A Multiwavelength Investigation of Blazar-type Active Galactic Nuclei

A THESIS
SUBMITTED IN PARTIAL FULFILMENT
OF THE REQUIREMENTS FOR THE DEGREE OF
MASTER OF SCIENCE IN PHYSICS
AT THE
UNIVERSITY OF CANTERBURY

by

Fane Bastin

2013

Abstract

A multiwavelength investigation is conducted for nineteen blazar-type active galactic nuclei. Studies of variability timescales and flux duty cycles are performed at x- and γ-rays for each source, with the relationship between flux and spectral index also being probed at γ wavelengths. The correlation between these two energy ranges is also investigated, by utilising the Discrete Correlation Function with both one and ten day binning. The sources were chosen for their availability over a range of different x- and γ-ray data sources: observations utilised include 0.2 - 150 keV x-ray data from the Swift mission and 200 MeV - 300 GeV γ-ray data from the Fermi mission.

Daily-binned Fermi data is used to calculate the smallest rise and decay e-folding times in γ for each source. The results range from 0.4 to 21 days, corresponding to limits on the size of the γ emission region ranging from $R\delta^{-1} = 4.39 \times 10^{12}$ to $R\delta^{-1} = 5.14 \times 10^{14}$ m.

Flux duty cycles for fourteen sources are created from Fermi data, with six displaying structure at high fluxes that indicate flaring states have occured. Five of these six sources also display clear flares in their light curves, confirming these results.

The relationship between the flux and the spectral index Γ shows eight of nineteen sources exhibit harder-when-brighter behaviour. Four of these eight have been previously confirmed to display such behaviour.

Results from the Discrete Correlation Function show a correlation at a time lag of ~ 600 days for H 1426+428, of uncertain origin. Gaussian functions are fitted to possible near-zero peaks in 3C 66A, 3C 454.3 and Mrk 421, which could be indicative of a synchrotron self-Compton component to the emission of these objects.

Contents

List of Figures

List of Tables

Chapter 1

Introduction

1.1 Active Galactic Nuclei

Every galaxy contains a black hole at its centre. While the centres of some galaxies are quiet and non-violent, such as our own Milky Way galaxy with its black hole Sagittarius A*, the centres of others have been observed to be emitting electromagnetic radiation very energetically. These systems are referred to as active galactic nuclei, or AGN. Observations of AGN have revealed emissions over an extremely wide range of wavelengths, from radio through to VHE γ-ray.

1.1.1 Current Model

The currently accepted model for AGN was first proposed by Urry and Padovani [32], and is shown in Figure 1.1. At the heart of the AGN, there is a supermassive black hole (SMBH), with a mass between approximately 10^6 and 10^{10} $M_\odot$ [33]. Some nearby matter under the influence of the SMBH falls to a low orbit, forming a disc of matter known as the accretion disc within around 1 pc of the black hole. The accretion disc has a width in the plane of motion, and so matter in the disc has different orbital speeds depending on the distance from the SMBH. Friction therefore causes matter in the disc to become heated, and so the accretion disc emits blackbody radiation which manifests itself in the form of various wavelengths, typically from infra-red through to x-rays. As the rate of accretion of matter into the disc changes, so the x-ray output of the disc changes. This relationship is thought to be strongly linked to the total activity of an AGN. Further out from the

SMBH, but not on the same plane as the accretion disc, there are regions of relativistic particles with various velocities. These particles reprocess the radiation emitted by the accretion disc into other wavelengths. The region closest to the SMBH (within 0.1 pc), which necessarily contains particles with higher velocities than those further out, has its emission lines significantly widened by Doppler effects and is thus known as the broad line region (BLR). Similarly, the region further out (within 1 kpc) is known as the narrow line region (NLR). On the same plane as the accretion disc, at a distance of around 1 pc from the SMBH, is a torus-shaped region of dust. This dusty torus blocks emissions from the accretion disc, BLR and NLR, meaning that AGN viewed from an angle close to the plane of the torus will appear to have reduced flux. The torus also reprocesses absorbed photons into infra-red energies, adding to the total observed spectrum of AGN. The final, and perhaps most enigmatic components of the AGN model are the relativistic jets. The jets are elongated regions, sitting approximately along the axis of rotation of the accretion disc, in which charged particles, accelerated to relativistic speeds, emit γ radiation [10]. With accelerated charged particles involved, the most natural explanation of the jets' structure and behaviour involves some sort of magnetic effect; it has not been determined exactly how such a field precisely acts or comes to exist, however. The jets are thought to be linked to the accretion disc, although the exact mechanism for this effect is also currently unknown. Models for the emission exist, however, that each posit something about the inner workings of the jet.

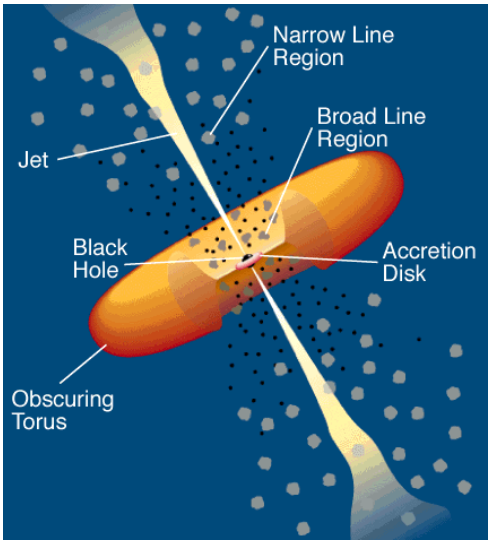

Figure 1.1 *The Urry and Padovani model for AGN. Shown are the supermassive black hole, accretion disc, dust torus, jet, BLR and NLR. (Image: C.M. Urry and P. Padovani)*

1.1.2 Classification

The model described above indicates a consistent structure in all AGN. Observations of AGN, however, show differences in the relative fluxes corresponding to certain components. Classes of AGN have been developed to categorise these differences. The differing observations can be explained by the model when one considers the angle of the AGN relative to the viewer: the angles and relative positions of the various components will affect the observed radiation, meaning that the emissions of AGN are not the same over all angles. For example, an AGN viewed from an angle near the plane of the accretion disc, as described above, will display reduced flux from central components due to the dusty torus blocking radiation. Conversely, an AGN viewed from an angle close to the axis of the jet will receive a much larger share of the emissions from the jet; a marked increase in γ-ray flux. This is precisely what is thought to mark blazar-type AGN apart from others. In addition to the viewing angle, however, the accretion rate can also strongly affect the observed characteristics. Blazars have been noted as being among the brightest of AGN types, as well as displaying the most variability. Within the blazar class, AGN can be further divided into flat spectrum radio quasars (FSRQs) and BL Lac objects. The distinguishing difference between these two classes is the width of emission lines, with FSRQs exhibiting broad lines where BL Lac objects do not. Observationally, FSRQs are frequently brighter than BL Lac objects at certain wavelengths.

1.1.3 Spectra

As previously mentioned, AGN emit over a very wide portion of the electromagnetic spectrum. The overall spectrum of an AGN (known as the spectral energy distribution or SED) can be described by a 'double-hump' structure, with each 'hump' corresponding to a specific set of physical phenomena (which will be described later in Sections 1.1.4 and 1.1.5). The lower energy hump generally spans from optical/UV energies ($\sim$ 1 eV) through to x-rays ($\sim$ 1 keV), with a peak at around 100 eV. The higher energy hump can span from soft x-rays ($\sim$ 100 eV) all the way to TeV γ-rays.
The range of the LAT detector (which will be described later in Section 1.5), 30 MeV - 300 Gev, falls on the high-energy side of the peak of this hump in most cases. In this subset, the spectrum is often well described by a power law of the form

$$\frac{dN}{dE} = N_0 \left(\frac{E}{E_0} \right)^{\Gamma} \tag{1.1}$$

where N_0 is a prefactor, E_0 is a defined energy scale and Γ is known as the photon index or spectral index. For those AGN with spectra that this equation describes well, the photon index is useful as an indicator of the state of the spectrum at a given time. For spectra where the flux is decreasing with higher energies, the photon index is negative, and for Fermi data usually has a value around -2. A spectrum with increased flux at higher energies, i.e. a more positive photon index, is referred to as being 'harder'; similarly, a 'softer' spectrum is one with a more negative photon index.

1.1.4 Synchrotron Self-Compton Emission Model

The synchrotron self-Compton (SSC) model proposes a single region of relativistic electrons, which by a combination of processes are responsible for the γ-ray emission of AGN. The region first produces x-rays via synchrotron processes, and then upscatters them via inverse-Compton (IC) scattering to much higher energies. In this way, the single region is responsible for the entire double-hump structure of the SED, mentioned previously in Section 1.1.3. As a result, a change in the output of the seed photon region will result in a corresponding change in the IC emission, meaning that quasi-simultaneous variation should be seen between the two photon populations. By observing the output of an AGN at a point on the low-energy as well as the high-energy hump in the SED, the applicability of the SSC model can therefore be tested. If the model holds, a correlation between the two observations should be found. Due to the energy ranges of the peaks in the SED, observations in soft x-rays as well as γ-rays should thus be sufficient to show a correlation. Since the positions of the seed photon region and the γ emission are constant, one would expect to see a constant characteristic time lag in the correlation. In addition to this fact, the emission regions of AGN are thought to be moving at relavtivistic speeds, and so a doppler correction needs to be applied to correctly model this effect.

1.1.5 External Compton Emission Model

The external Compton (EC) model differs from the SSC model in several respects. In this model, a population of relativistic electrons still exists, and still upscatters photons via the IC process, but this region is no longer the primary source of seed photons. A number of external sources also provide seed photons to the IC emission, for example radiation from the accretion disc or dusty torus, or reprocessed radiation from the broad- and narrow-line regions. The correlation characteristic to the SSC model is thus greatly

complicated, since no single source is likely responsible for the majority of seed photons, and the region of particles posited in the SSC model may not even be present. If there remains an SSC component to a given source's emission, a correlation between soft x-rays and γ-rays still exists, although correlations between other wavelengths such as infra-red and γ-rays likely also exist in this model, and provide significant numbers of seed photons. The characteristic time lag of the correlation depends on the source of the seed photons, and so different characteristic time lags arise corresponding to each source.

1.2 Variability

In contrast to non-active galaxies which have a constant luminosity, AGN emission is frequently observed to be variable. This variability can be used to quantify some of the physical differences between AGN, as well as to place limits on the size of emission regions via causality.

When analysing the variability of an object, it is useful to have a numeric indicator of the variability itself. The logical way to analyse the variability of time-dependent values is to fit some function between the values, taking into account both the differences in the observed variable and the time elapsed between the data. While a simple answer would be to fit a line between data, and take the gradient, this does not take into account that any changes in the emission of AGN are unlikely to be linear in nature. To this end, it is better to model an exponential increase or decrease to the variability, as exponents take into account the state of a system having an effect on its variability. One commonly used indicator of AGN variability is therefore the characteristic e-folding timescale (e-folding time), defined by

$$F(t) = F(t_0)e^{(t-t_0)/\tau} \tag{1.2}$$

where $F(t)$ is the final value of the variable, $F(t_0)$ is the initial value and τ is the e-folding time. The e-folding time τ can be found between any two data points, although in practice it is most useful to find it for the smallest time period possible, i.e. between adjacent data points. Using the smallest change in time means that the shortest timescales may be found, which can be used to place limits on the time needed for emission regions to change. This in turn means that, via causality, a limit on the size of the emitting region can be found. In order to accurately do this, however, the redshift of the source must be taken into account and the calculated e-folding time adjusted accordingly. The

redshift-corrected e-folding times are given by

$$\tau_{actual} = \frac{\tau_{apparent}}{1+z} \tag{1.3}$$

where z is the redshift.
When calculating limits on the size of an emission region, the movement of the region must be taken into account in the form of the Doppler factor, δ, such as in Brown [11]. The inequality representing the limit on the size of the region is then

$$R \leq c\tau\delta \tag{1.4}$$

where R is the size of the emission region and δ is the Doppler factor.
Another common indicator of variability is the doubling timescale which, rather than an increase or decrease by a factor of e, corresponds to an increase or decrease by a factor of two. Conversion between the two is a simple matter of changing from base e to base 2.

1.3 Thesis Aims

As it currently stands, AGN are somewhat of an enigma, with energetic large-scale processes occurring and no single comprehensive model existing. In particular, the exact mechanism which gives rise to the relativistic jets of AGN remains a compelling area of study. The best way of providing insight into these areas is to constrain known values. In this thesis, studies of a number of BL Lac and FSRQ objects are presented. The objective is to obtain information regarding these objects which can be used to probe the mechanism responsible for the relativistic jets of AGN.
Nineteen blazars were chosen, as will be discussed in Section 1.4, based on the availability of x- and γ-ray data from a number of different detectors.
Firstly, the variability of the chosen objects was characterised. The motivation for this is similar to in-depth studies of AGN variability, such as the analysis of 3C 454.3 and PKS 1510-089 in Tavecchio et al. (2010) [31]. In this paper, the smallest variability timescales for the two sources were found, allowing constraints to be placed on the size of the γ-ray emission region. Foschini et al. (2011) [19] also investigate the smallest variability timescales, this time for the FSRQs 3C 454.3, 3C 273 and PKS 1222+216 (4C 21.35). A different approach to the variability is also utilised in this thesis, creating for the e-folding

timescale a histogram which shows the distribution of variability timescales for a source. Next, histograms of the flux, known as duty cycles, were produced for each object. These are similar to those presented in Tavecchio et al. (2010), showing the relative proportions of different levels of flux. This approach allows the difference between typical and atypical fluxes to be observed, such as identifying when a source has been in a flaring state. Creating duty cycles for x- as well as γ-ray wavelengths could provide insight into the similarities and differences of AGN behaviour at those wavelengths.
Another area in which it is useful to ascertain information is the interaction of the two peaks in the SED, with the behaviour of these two regions allowing an investigation into the source of the γ-ray emission as described in Sections 1.1.4 and 1.1.5. Certain correlations between the two energy ranges can show the existence of various models for AGN emission. To this end, correlation between x- and γ-ray emission is studied in this thesis. Finally, flux versus. spectral index plots were created for each object, looking for harder-when-brighter (HWB) behaviour. Such behaviour is a common feature of AGN, with the γ-ray spectrum of an object emitting more photons at higher energies during periods of high flux. As described later in Section 2.5, HWB behaviour indicates an acceleration and cooling scenario. Identifying HWB behaviour in an object would indicate that such a scenario was indeed taking place.

1.4 Source Selection

In order to investigate the γ- and x-ray properties of sources, it was necessary to obtain data in both energy ranges for a number of AGN. Data from the Fermi Gamma-ray Space Telescope and the Swift mission, described in Sections 1.5 and 1.6 respectively, were utilised for this purpose. The Fermi 2-year AGN catalogue [6] contains all AGN detected by the satellite for the first two years of its operation. The Swift website contains sensitive lightcurve data for a large number of AGN in its 9 month AGN catalogue and 22-month source catalogue, but these do not contain data recent enough to be simultaneous with the Fermi data. The Swift transient monitor, however, does contain simultaneous data, although at a cost in sensitivity. The Rossi X-ray Timing Explorer (RXTE) mission, another space-based x-ray telescope, also has a catalogue of AGN [27]. By cross referencing the Fermi and RXTE catalogues, a list of 21 AGN with data from both sources was compiled, representing the entirety of sources with data available from both catalogues. This list was again cross-referenced, to the Swift transient monitor, which contained data from 19 of the 21 sources. These sources are shown in Table 1.1, along with their

classifications and redshifts.

Fermi data were downloaded for each of the sources for the time interval from 54682 to 55902 MJD, approximately 40 months. Swift BAT data were downloaded for the entire interval of time then available, between 53414 and 56224 MJD, approximately 90 months. A simultaneous time period equal to the entire Fermi observations was thus achieved. In addition to the BAT data, Swift XRT data corresponding to times simultaneous with Fermi were downloaded for 16 sources from the Swift Monitoring Program at Penn State University [29]. The sources for which these data were available are noted in the final column of Table 1.1. RXTE data were not utilised due to the inconsistent observations and lengths of observation, being more suited to short timescale analyses.

Source	**Type**	**Redshift**[6][1]	**XRT Data**
1ES 1959+650	BL Lac	0.048	yes
1H 0414+009	BL Lac	0.287	yes
3C 66A	BL Lac	0.444	yes
3C 273	FSRQ	0.158	yes
3C 279	FSRQ	0.536	yes
3C 454.3	FSRQ	0.859	yes
4C 21.35	FSRQ	0.434	yes
4C 71.07	FSRQ	2.172	-
AO 0235+16	BL Lac	0.940	yes
H 1426+428	BL Lac	0.129	yes
I Zw 187	BL Lac	0.055	yes
Mrk 180	BL Lac	0.046	-
Mrk 421	BL Lac	0.031	yes
Mrk 501	BL Lac	0.034	yes
PKS 0528+134	FSRQ	2.070	yes
PKS 2005-489	BL Lac	0.071	-
PKS 1502+106	FSRQ	1.839	yes
PKS 1510-089	FSRQ	0.360	yes
PKS 2155-304	BL Lac	0.116	yes

Table 1.1 *Complete list of sources obtained by cross-referencing Fermi, Swift and RXTE catalogues. Classification, right ascension, declination and redshift of each source is shown. The availability of Swift Monitoring Program data is denoted in the final column.*

1.5 Fermi Gamma-ray Space Telescope

The Fermi Gamma-ray Space Telescope (Fermi) [8] is a mission launched in June 2008 to investigate the γ-ray sky. The two main instruments aboard Fermi are the Gamma-ray Burst Monitor, used to detect and investigate γ-ray bursts, and the Large Area Telescope (LAT), which is used to periodically map the entire γ-ray sky and for a small number of pointed observations. By rocking on its axis, Fermi enables the LAT to map the entire sky in its orbit, with this being achieved every two orbits; approximately every 3 hours. This allows sources across the entire γ-ray sky to be monitored with 3-hour resolution over almost the entire mission time of the telescope. All data collected since operation began in August 2008 are available to the public for use, as well as the software designed to process these data.

1.5.1 Large Area Telescope

The LAT instrument itself consists of a few major components, as shown in Figure 1.2. From the point of view of a photon entering the detector, the first is an "anticoincidence" layer. γ-rays do not interact with the layer, and so pass through unhindered, while particles such as cosmic rays collide with the material of the layer and are detected before entering the instrument. Next come the layers of conversion material and particle tracking layers. A γ photon hits a layer of conversion material, and decays into an electron and a positron, which are tracked by the particle tracking layers. Finally, the electron and positron enter a calorimeter which measures their energy. The result is a measurement of a confirmed γ photon, with its angle relative to the detector reconstructed from the paths of the two charged particles it decays into, its energy measured by the calorimeter. For each event, these parameters are recorded. An event's status as being or not being a γ-ray is recorded as the "event class" in the final raw data files.

An important consideration when dealing with LAT data is the point spread function (PSF) of the detector. The PSF varies with energy, with higher energy photons having a smaller PSF and therefore a more accurate angle recorded. Near the lower energy limit of the detector, at 100 MeV, each photon's angle is accurate to around 8° (with 95% confidence). At 200 MeV, this figure reduces to around 5°. As a result, the necessary radius of interest (ROI) used when processing data is primarily determined by the lower energy limit desired for the analysis.

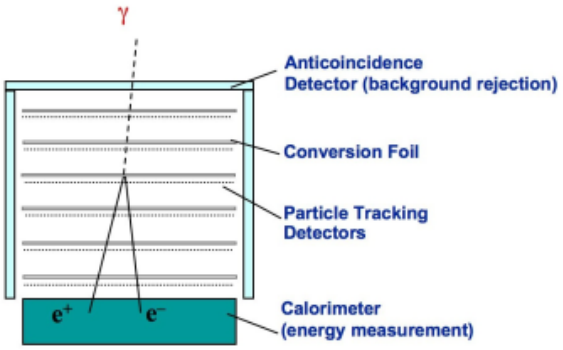

Figure 1.2 *The layout of the LAT detector, showing anticoincidence, conversion and tracking layers. (Image: www-glast.stanford.edu)*

The viewing angle relative to the Earth also has an effect on LAT data. The Earth's atmosphere can provide a γ-ray signal which interferes with the signal from the desired source, as well as directly causing a reduction in the signal from the source. To this end, the Fermi satellite records a parameter known as the "zenith angle", which denotes the angle of the satellite's zenith relative to that of the earth. In order to remove the effect of the Earth's atmosphere, data with an unsatisfactory zenith angle ($> 100°$ recommended) are usually discarded.

A flux of photons with a particular spatial density will result in different numbers of observed events as the angle relative to the detector changes. A source emitting photons such that they arrive normal to the detector will result in more recorded events than a similar source at an angle to the normal, due to the effective area of the detector changing. This is another effect that must be compensated for when processing Fermi data. To achieve this, an exposure must be calculated, and the exposure cancelled out in the final fluxes.

1.6 Swift Mission

The Swift Gamma-Ray Burst Mission was launched to investigate γ-ray bursts and hard x-ray emission [9]. The Swift satellite carries three main instruments: the X-Ray Telescope (XRT), the Ultraviolet/Optical Telescope (UVOT), and the Burst Alert Telescope (BAT). The UVOT, as the name implies, can detect optical and UV wavelengths between 170 and 650 nm.

The BAT is capable of detecting x-rays from 15 to 150 keV, with the latter end of the

range being considered 'hard' x-rays. The BAT consists of two main components: a coded aperture and a solid-state detector. The coded aperture consists of an x-ray opaque material with holes of known arrangement, and the detector counts photons. The coded aperture causes multiple images to be observed on the detector; with the pattern of the mask known, a computer algorithm can be applied to the result to separate the images, and thus ascertain certain properties of the incoming photons. The sensitivity of the instrument depends on the amount of coding the incoming signal is subjected to, and as the angle of the incoming photons affects the position of the coded 'shadow' on the detector, the sensitivity is thus dependent on the angle. The BAT covers a solid angle of around 1 steradian with full coding, and a total of around 3 steradians with partial coding.

The XRT has an energy range of 0.2 - 10 keV, and is used for pointed observations at objects. The telescope itself uses grazing-incidence mirrors to focus x-rays onto a CCD, and has a 110 cm^2 effective area with a 23.6×23.6 arcminute field of view. The resolution of the telescope is around 18 arcseconds.

Data available on the Swift website include transient monitor data as well as more focussed observations. The transient data are collected in a manner similar to that of Fermi's all-sky survey, with slew observations being used to construct the available light curves. The more focussed observations are currently available in the form of an AGN catalogue comprising the first 9 months of the mission, a source catalogue comprising the first 22 months of the mission, and hard x-ray surveys comprising up to the first 70 months of the mission. These observations are based on pointed observations as well as slew data, and typically contain more sensitive data due to a more focussed field of view. Additionally, a data source is available that aims to supplement Fermi observations with observations from the XRT onboard Swift [29].

Chapter 2

γ-ray Analysis

2.1 Fermi Science Tools

The Fermi Science Tools are a collection of programs and files designed to enable the analysis of Fermi data. Various programs allow things such as: the selection and exclusion of data, the creation of necessary files such as exposure maps, and the production of light curves and sky maps. The programs are designed to work with the format of Fermi data, and allow the various considerations discussed in Section 1.5.1 to be dealt with.

γ-ray data files, in the form of Fermi observations, consist of two parts. The first is a series of "photon files" for each source, which contain all the raw information as detected by the LAT. This includes the energy, angle of entry into the detector, and event class for each photon received. The second is a "spacecraft file" which contains information pertaining to the state of the detector over the course of the observation. This includes such things as the angle of the detector relative to the Earth and the source, which are needed later. Additionally, models of the galactic and extragalactic γ-ray background are available which are updated by the Fermi collaboration. The collaboration periodically updates its software and the aforementioned background models, ensuring that the most up-to-date data are being used to process Fermi observations. Each time this is performed is called a 'pass'; the current software is based on Pass 7 data.

In order to extract useful data from the raw data that are supplied, a series of tools from the provided software must be utilised. First, the data must undergo selections in time and angle, to isolate the region which is to be analysed (`gtselect`), and provide checks which ensure the validity and usefulness of the data (`gtmktime`). A 'live-time cube' must then be computed (`gtltcube`) which examines the time spent looking at each

area of the sky, taking into account viewing angles, and creates a file necessary for the next step. An exposure map must then be calculated, which will be used to compensate for the difference in received flux as described in Section 1.5.1 (`gtexpmap`). Next, it is necessary to provide spatial and spectral models for each source present in the field of view, including spatial and spectral models and models of the galactic and extragalactic γ-ray background. These must be specified in an XML file, which is used in the next step. With the models provided, a likelihood fitting algorithm (`gtlike`) is applied to fit the models to the data. The result of one such sequence is an output detailing the state of the modelled AGN over the period of the observations, including the average flux and average parameters relating to the spectral models used.

Included in the output from the likelihood fitting is the test statistic (TS), which is approximately equal to the square of the σ value. The TS value, for a given fit, is a measure of the probability that the data match the model used to describe them. It is defined as $2[logL - logL_0]$; that is, twice the difference between the log-likelihood of two models, L and L_0. These models represent the source being included or not, respectively. A low TS value indicates that the model is a poor representation of the data, and that the values of the parameters used by the model to describe the data may therefore not be sufficiently accurate. It is therefore necessary to specify a lower TS limit, below which the model's parameter values cannot be considered admissible. Due to the way the likelihood fitting works, a higher TS value more often occurs with a strong signal, i.e. more recorded photons. For the same limits on time, a brighter source will therefore usually have a higher TS value than a dimmer one.

The information supplied by such an output is useful, but it is much more useful to have a series of bins, each of which is analysed in this manner. To this end, a Perl script `like_lc.pl` [15] is available which allows the user to input a model file for a given source, specify a binning interval and minimum TS value, and run the above sequence for each bin in the data provided. This script as provided, however, is not sufficient for current Fermi analysis. Similarly, a Python script is available which generates a model file for a given source, using a Fermi γ-ray source catalogue to model all nearby sources.

2.1.1 Modelling and Likelihood Fitting

The `like_lc.pl` script described in Section 2.1 is useful, but lacks certain features in its default form. The script was modified to use the latest Pass 7 Fermi data and the associated new catalogues, and further modified to allow parameters relating to the model fit to be more strictly controlled. Using the modified `like_lc.pl` and the Python model-

file script from Section 2.1, each source was processed using daily bins. The program `like_lc.pl` is quite processor intensive, with the likelihood fitting sometimes taking on the order of weeks to process all the bins for a source. Sources 3C 66A, 3C 273, 3C 279, 3C 454.3, 4C 21.35, AO 0235+16, Mrk 421, PKS 1502+106 and PKS 1510 had previously been processed with an 8° ROI, and so these data were used. The remaining sources were processed using a 5° ROI, which meant fewer dynamically modelled background sources, and thus less time taken. Each source was modelled using the power law spectral model detailed in Eq. 1.1. The energy range from 200 MeV to 300 GeV was used for all sources, and since a point source has an approximately 5° PSF at 200 MeV in the LAT detector, the 5° size of the ROI that was utilised was sufficient. A minimum TS of 10 was used for the `like_lc.pl` program, meaning that any bins which fell below approximately $\sigma = 3$ were excluded from the final results. The data in these bins were the output of fitted models which, by the choice of a minimum TS value, were deemed to not sufficiently represent the physical data they modelled. The data in the excluded bins were therefore not accurate enough to include in any results.

2.2 *e*-folding Timescales

A program was written to calculate the e-folding time between adjacent bins of a specified data file. This program is shown in its entirety in Appendix A. The errors on the e-folding time value were calculated by using an equation of the form $\Delta z = z\sqrt{\left(\frac{\Delta u}{u}\right)^2 + \left(\frac{\Delta v}{v}\right)^2}$ and substituting flux and time values for u and v. As the structure of the input file varied depending on the source of the data, the input variables had to be reorganised depending on the file. A separate program was thus made for every different file structure, enabling e-folding times to be rapidly calculated for every file.

e-folding times for the processed daily-binned Fermi LAT data as well as the downloaded Swift BAT data were found between all bins using the above method.

The e-folding times, thus recorded, were able to be plotted as histograms to show the frequency of different timescales. This was done for all sources.

The characteristic e-folding timescale, as defined in Equation 1.2, is a function of differences in time and differences in flux. The smallest e-folding time for a given object is often one of the most useful pieces of information, but the form of the data being used can greatly limit the resulting timescale. Consider two points which are being used to fit an e-folding value: one point is higher than the other, and there is a constant time between the two points. A line connected between those points will have a specific gradient, and

as long as the ratio of the difference in height to the difference is time is unchanged, so the gradient of the line is unchanged. Consider now that the two points are bins in a light curve, the averaged result of values which fell into each bin. If the binning time in this example were to be reduced, say to half the previous time, there would now be more bins in the same space of time. There is a negligible chance that the points corresponding to these new bins would fall exactly on the line between the original two points. Connecting lines between these new points, then, we would see shorter lines which had gradients both smaller and larger than the initial line; that is to say, the shorter binning has allowed a line with a steeper gradient than the initial line to be found. An e-folding timescale depends on the same inputs as a line between points, and, similar to the line, the timescale depends on the ratio between magnitude and time. It follows, then, that the binning time used affects the smallest e-folding time that can be found in a given set of data. When comparing the smallest e-folding times of different sources, this effect must be taken into account. The same binning must be used for the smallest e-folding times to have any relevant comparison, and the smallest possible binning must be used if the absolute smallest e-folding timescale is sought. This effect is apparent in, e.g., Brown & Adams (2011) [13] and Saito et al. [26].

2.3 Light Curves and Variability

The light curves from the `like_lc.pl` output for Fermi LAT observations are shown in Figures 2.1, 2.2 and 2.3, showing only those bins with a TS value greater than 10. The relative dearth or abundance of surviving bins is clearly visible in the number of plotted points for each source. Sources 3C 273, 3C 279, 3C 454.3, 4C 21.35, AO 0235+16, PKS 1502+106 and PKS 1510-089 can be seen to show periods during which the activity is higher than the surrounding regions of time; states of flaring activity.

The smallest e-folding rise timescales, calculated with daily-binned Fermi LAT data, are shown for each source in Table 2.1. Approximate MJD values, corresponding to the end of the bin used to calculate τ, are also shown, as are the size limits on the γ-ray emission region for each source. The size limits were calculated using redshift-corrected smallest e-folding times, as given by Equation 1.3, multiplied by the speed of light in a vacuum. These values are not corrected for the unknown Doppler shift of each region, and are thus given in terms of $R\delta^{-1}$ as a simple rearrangement of Eq. 1.4.

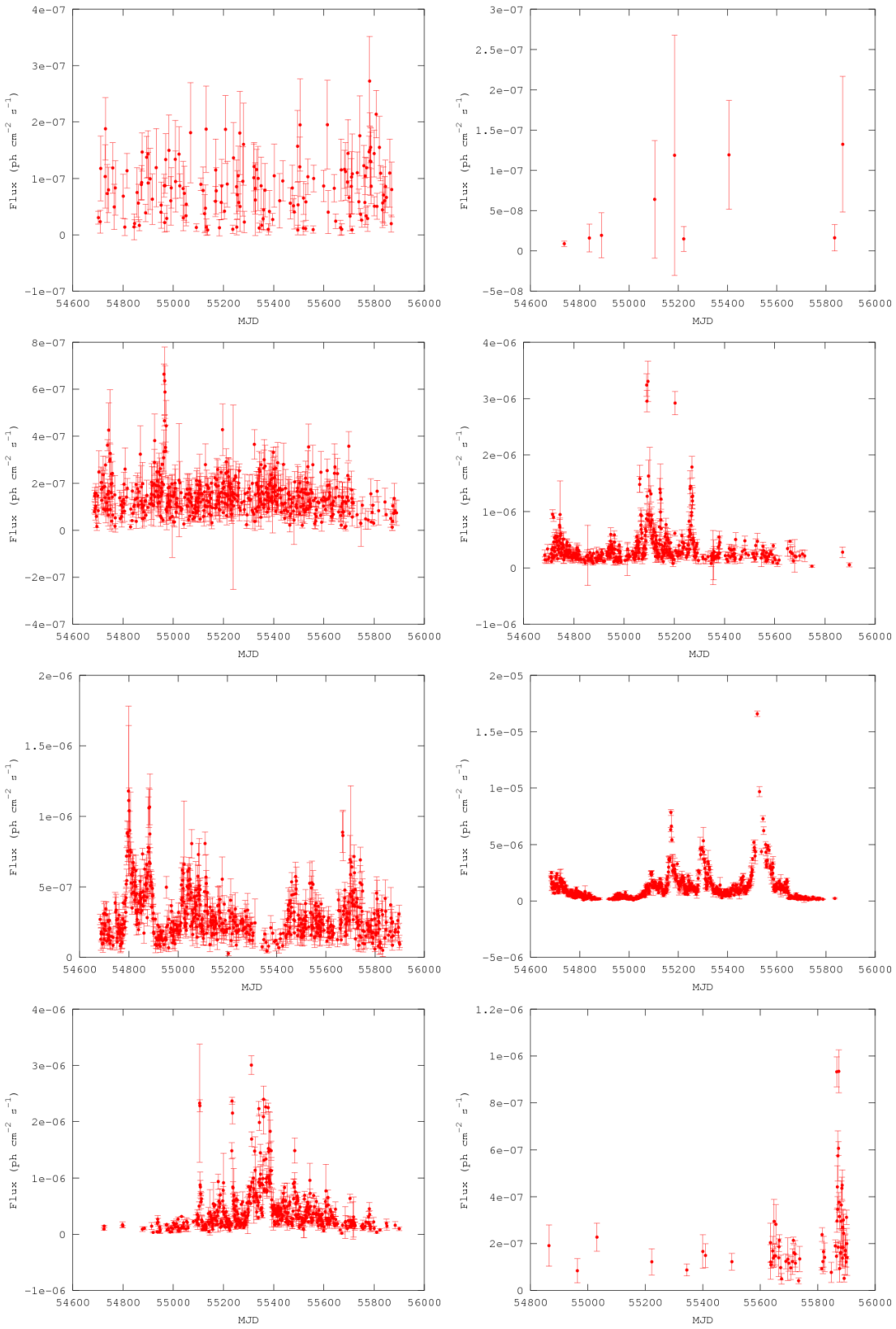

Figure 2.1 *Light curves for Fermi data, with daily bins. Left to right from top: 1ES 1959+650, 1H 0414+009, 3C 66A, 3C 273, 3C 279, 3C 454.3, 4C 21.35, 4C 71.07.*

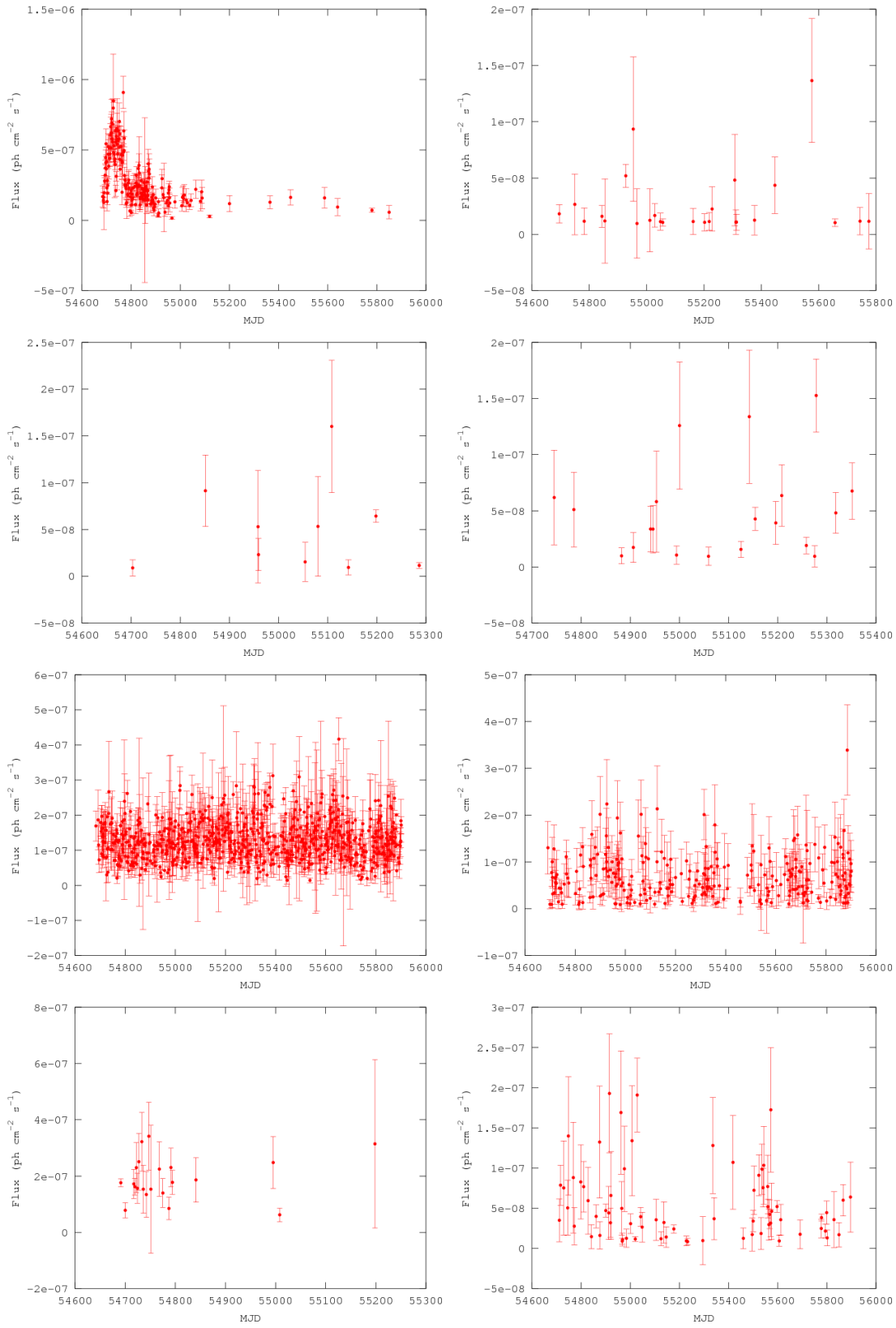

Figure 2.2 *Light curves for Fermi data, with daily bins. Left to right from top: AO 0235+16, H 1426+428, I Zw 187, Mrk 180, Mrk 421, Mrk 501, PKS 0528+134, PKS 2005-489.*

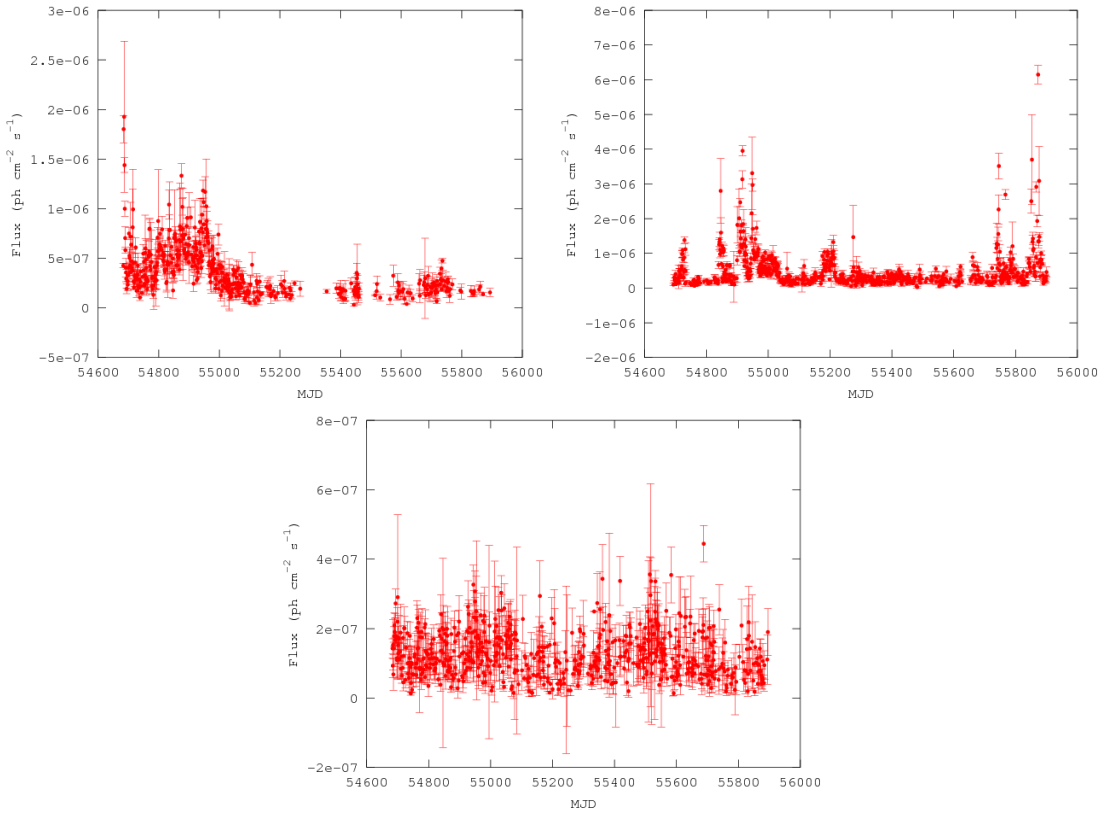

Figure 2.3 *Light curves for Fermi data, with daily bins. Left to right from top: PKS 1502+106, PKS 1510-089, PKS 2155-304.*

Histograms of the e-folding rise times for each source are shown in Figures 2.4 and 2.5, and histograms of the e-folding decay times are shown in Figures 2.6 and 2.7. Sources MRK 180, I Zw 187, 1H 0414+009, PKS 0528+134 and H 1426+428 are excluded due to the low number of bins remaining after the TS threshold was applied. Sources 1ES 1959+650, 4C 71.07, AO 0235+16 and PKS 2005-489 have their rise and decay e-folding histograms plotted in 1 day bins, due to the relatively small number of entries for these sources, while the remaining sources have their histograms plotted with 0.5 day bins to better display the distribution.

Source	τ_{rise} **(days)**	**MJD**	τ_{decay} **(days)**	**MJD**	$R\delta^{-1}$ ($\times 10^{13}$ **m**)
1ES 1959+650	0.4 ± 0.3	55713	0.3 ± 0.3	55496	0.982 ± 0.741
1H 0414+009	15 ± 10	55868	17 ± 18	55222	31.7 ± 20.1
3C 66A	0.52 ± 0.14	55688	0.5 ± 0.3	54768	0.928 ± 0.251
3C 273	0.61 ± 0.05	54719	0.7 ± 0.4	55072	1.37 ± 0.11
3C 279	0.71 ± 0.11	54952	0.6 ± 0.5	55831	1.21 ± 0.19
3C 454.3	0.9 ± 0.2	55729	0.6 ± 0.4	54815	1.22 ± 0.33
4C 21.35	0.49 ± 0.05	55233	0.6 ± 0.3	55188	0.881 ± 0.090
4C 71.07	0.54 ± 0.04	55866	0.8 ± 0.5	55876	0.439 ± 0.032
AO 0235+16	11 ± 3	55858	0.7 ± 0.2	54801	14.6 ± 4.0
H 1426+428	15 ± 13	55228	3 ± 3	55311	33.5 ± 29.7
I Zw 187	21 ± 20	55080	1.2 ± 0.9	54949	51.4 ± 49.1
Mrk 180	1.1 ± 0.2	55278	11 ± 3	55154	2.67 ± 0.50
Mrk 421	0.44 ± 0.05	55327	0.5 ± 0.5	55441	1.10 ± 0.13
Mrk 501	0.34 ± 0.14	55980	0.4 ± 0.5	54830	0.861 ± 0.351
PKS 0528+134	4.0 ± 1.2	54791	4 ± 2	54736	3.38 ± 1.01
PKS 2005-489	0.6 ± 0.3	55572	0.5 ± 0.5	54876	1.42 ± 0.73
PKS 1502+106	0.6 ± 0.2	55102	0.6 ± 0.3	55444	0.572 ± 0.182
PKS 1510-089	0.43 ± 0.02	55767	0.6 ± 0.4	55268	0.824 ± 0.038
PKS 2155-304	0.44 ± 0.10	55191	0.5 ± 0.4	55689	1.01 ± 0.23

Table 2.1 *The smallest e-folding rise and decay times in Fermi data for each source, with errors and associated MJD, calculated using Eq. 1.2 on daily bins. All values are given in days. Upper size limits on the emitting region for γ-rays are given in units of 10^{13} m, calculated using redshift-corrected e-folding rise times.*

The light curves in Figures 2.1 through 2.3 show the activity of each source in γ-rays over the period of the Fermi observations. Some sources, namely 3C 273, 3C 279, 3C 454.3, 4C 21.35, AO 0235+16, PKS 1502+106 and PKS 1510-089 have clearly visible flaring activity

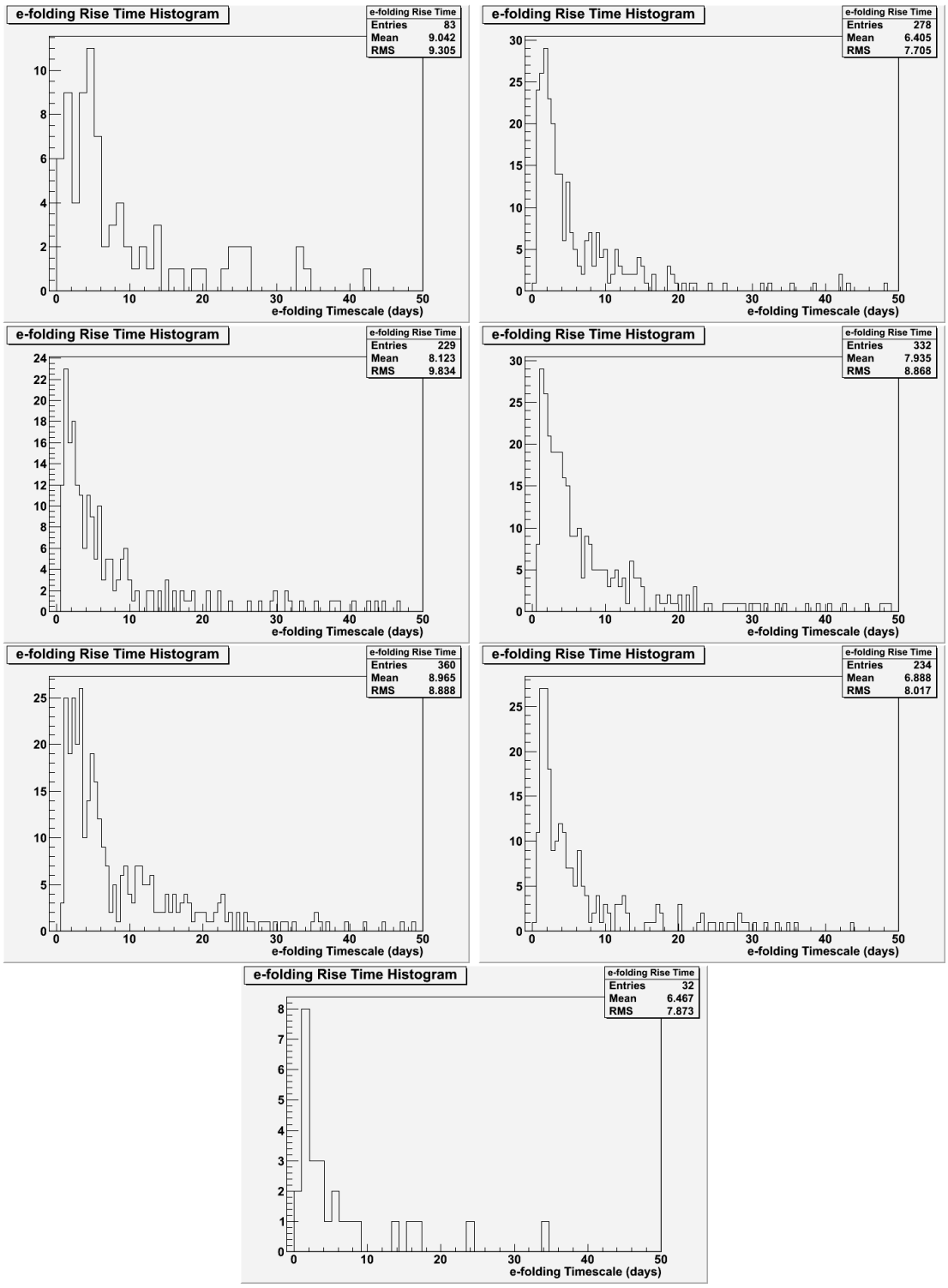

Figure 2.4 *Histograms of the γ-ray e-folding rise times for seven sources, plotted using daily-binned Fermi data. Sources 1ES 1959+650 and 4C 71.07 show 1 day bins for e-folding times, while the remaining sources show 0.5 day bins. Left to right from top: 1ES 1959+650, 3C 66A, 3C 273, 3C 279, 3C 454.3, 4C 21.35, 4C 71.07.*

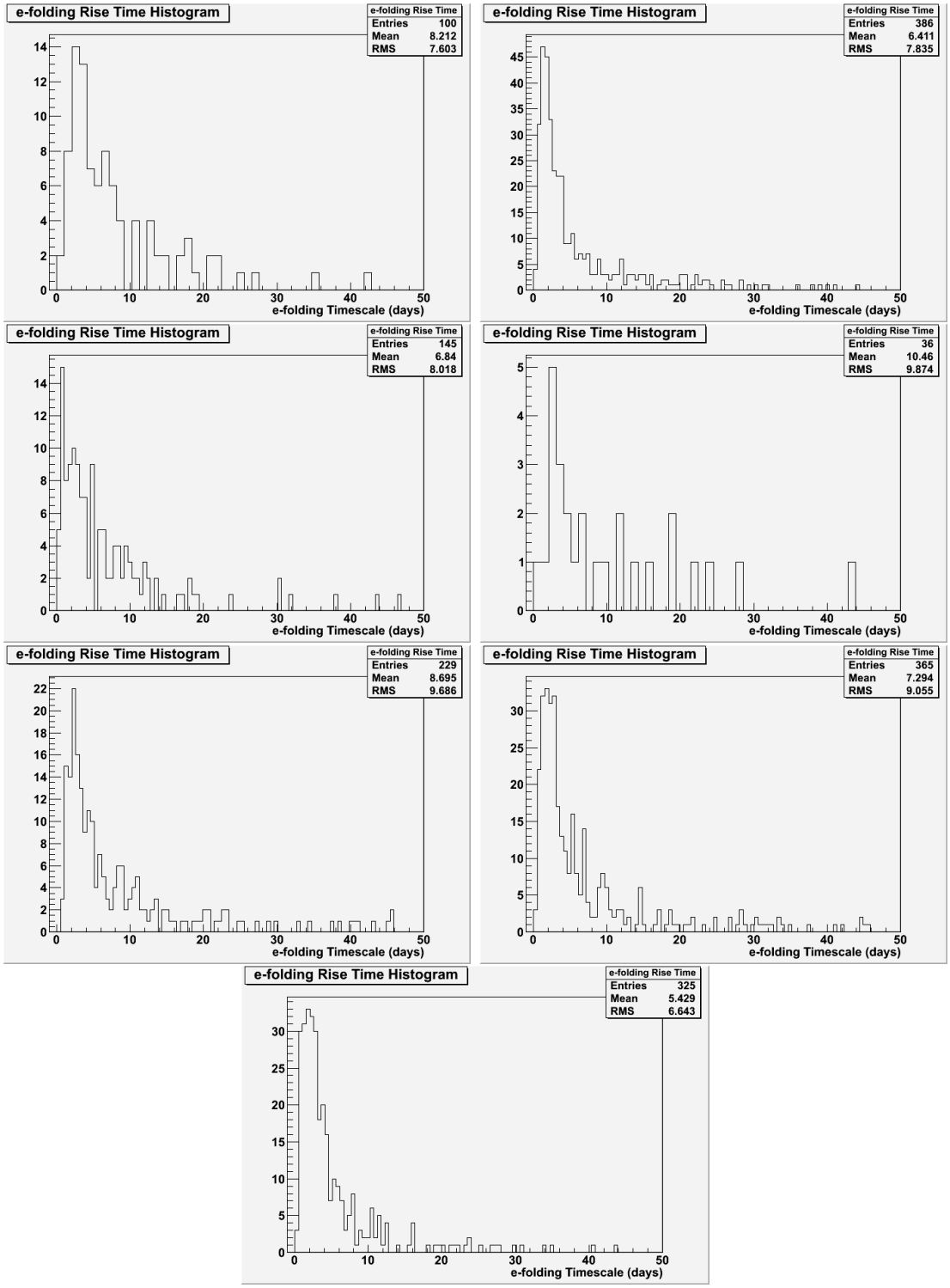

Figure 2.5 *Histograms of the γ-ray e-folding rise times for seven sources, plotted using daily-binned Fermi data. Sources AO 0235+16 and PKS 2005-489 show 1 day bins for e-folding times, while the remaining sources show 0.5 day bins. Left to right from top: AO 0235+16, Mrk 421, Mrk 501, PKS 0528+134, PKS 2005-489, PKS 1502+106, PKS 1510-089, PKS 2155-304.*

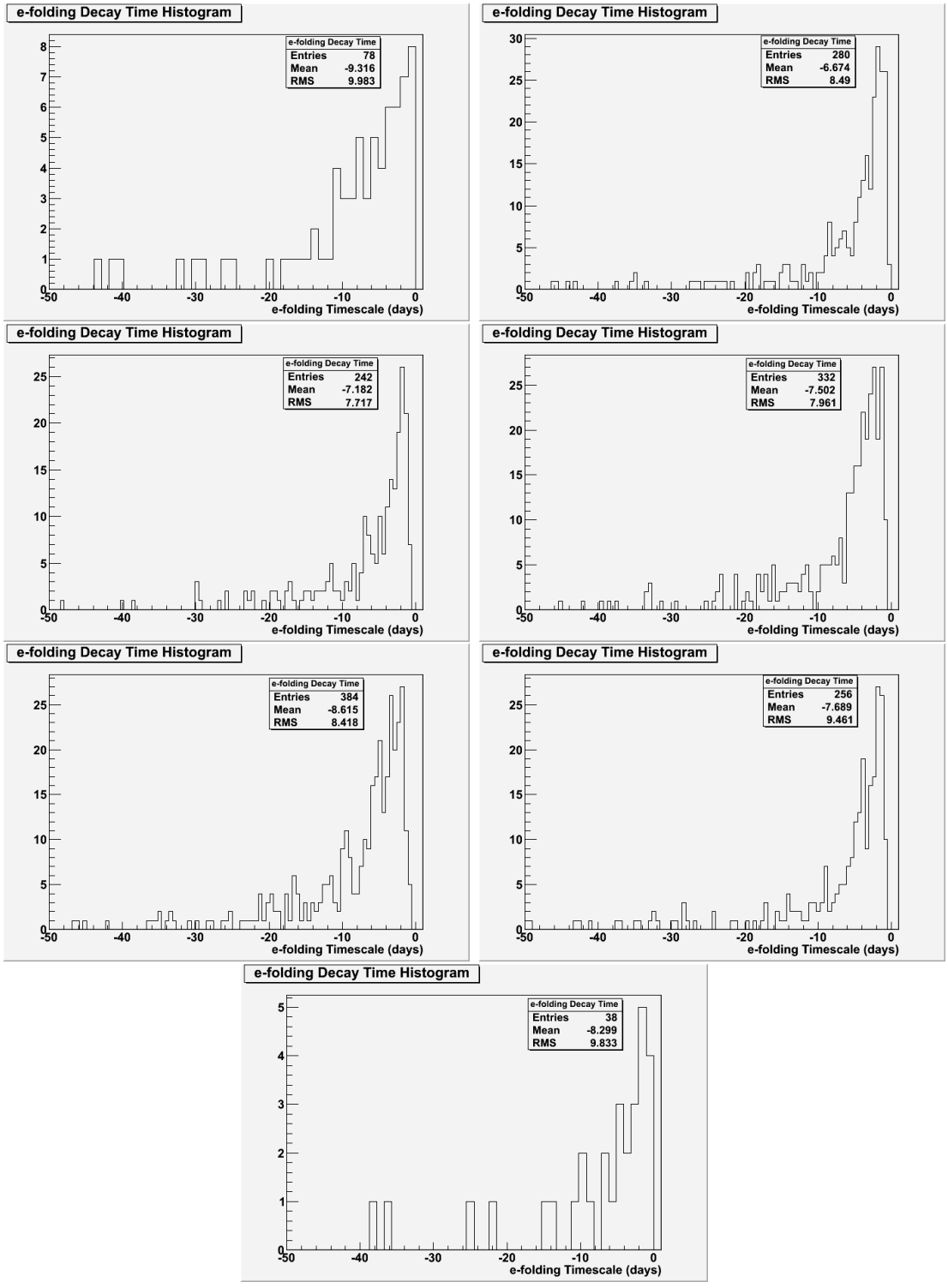

Figure 2.6 *Histograms of the γ-ray e-folding decay times for seven sources, plotted using daily-binned Fermi data. Sources 1ES 1959+650 and 4C 71.07 show 1 day bins for e-folding times, while the remaining sources show 0.5 day bins. Left to right from top: 1ES 1959+650, 3C 66A, 3C 273, 3C 279, 3C 454.3, 4C 21.35, 4C 71.07.*

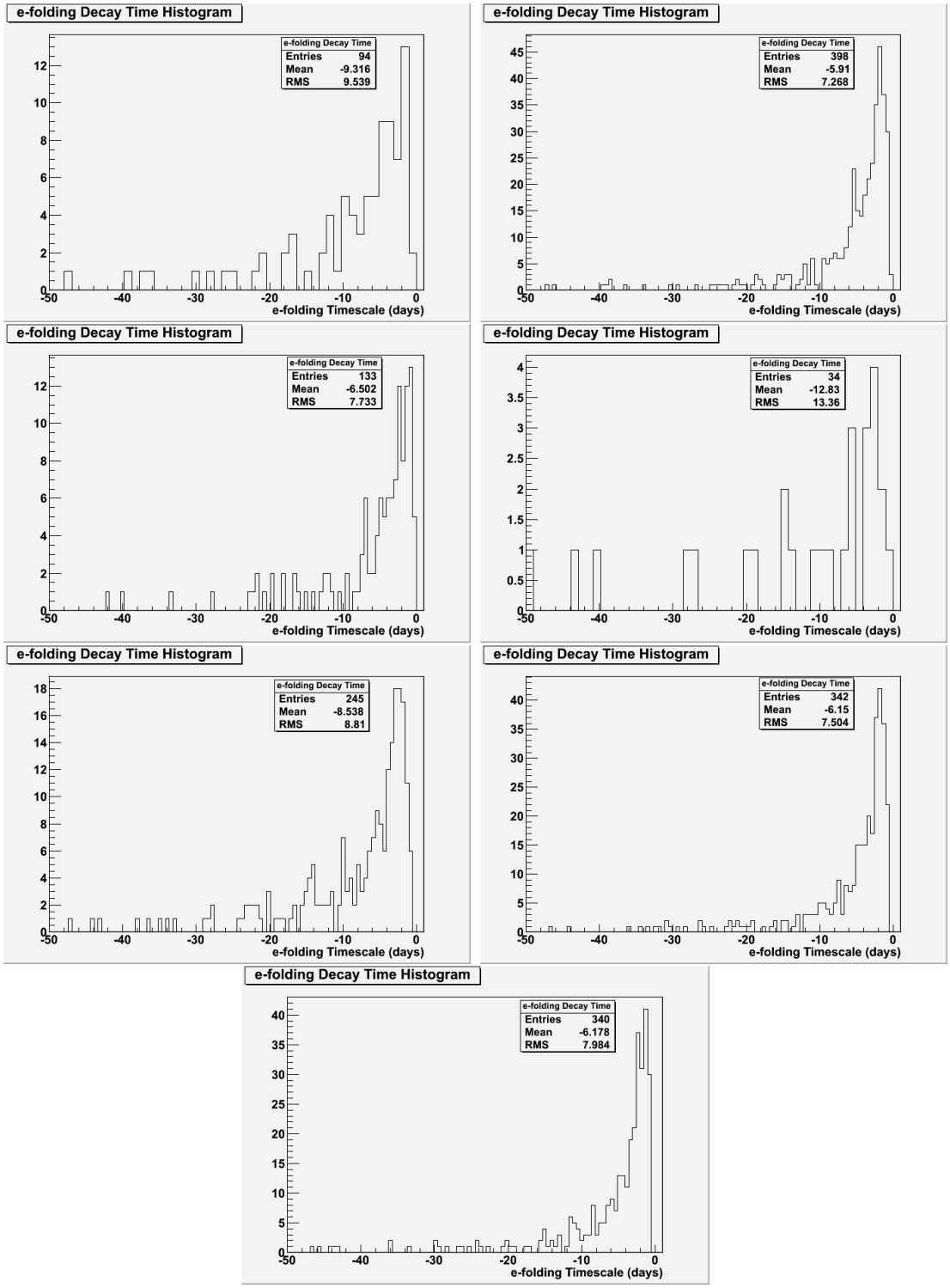

Figure 2.7 *Histograms of the γ-ray e-folding decay times for seven sources, plotted using daily-binned Fermi data. Sources AO 0235+16 and PKS 2005-489 show 1 day bins for e-folding times, while the remaining sources show 0.5 day bins. Left to right from top: AO 0235+16, Mrk 421, Mrk 501, PKS 0528+134, PKS 2005-489, PKS 1502+106, PKS 1510-089, PKS 2155-304.*

in their plots. Of these sources, all but AO 0235+16 are FSRQs. The range of energies visible to the LAT detector fall on the high-energy side of the inverse-Compton peak of the SED for FSRQs, including the high-energy tail of these objects. This means that any variation in the tail of FSRQs is apparent in Fermi data, with large-scale variation being commonplace. In contrast, the range of energies available to the LAT falls approximately at the peak of the Compton hump for BL Lac objects, meaning that there exists less apparent large-scale variation in the plotted light curves. With this knowledge, it is often possible to identify which sources are BL Lac objects and which are FSRQs simply by looking at their light curves, as in several cases here.

Due to the daily binning on the Fermi data, the e-folding times shown in Table 2.1 are very likely not the smallest timescales that any of the sources actually exhibit. In order to find the actual smallest times, data would have to be used with the smallest binning possible, such as in Foschini et al. [19] where changes on the order of a few hours were analysed and timescales of a similar length were found. The e-folding times found here can place very strict upper limits on the smallest time, however, since any data which did not meet the stringent requirements described in Section 2.1.1 were discarded. As the binning of Fermi data becomes smaller, so the uncertainties become bigger simply due to the statistical nature of the data. Although the limits on the size of the emission region for each source are not small, they are accurate. These size limits range from 4.39×10^{12} m for 4C 71.07 to 5.14×10^{14} m for I Zw 187, although the actual limits depend on the Doppler factors of each source. In extreme cases, such as for PKS 1510-089 in Kadota et al. [23], δ has reached values as high as 47. This means that the actual limit on the size of the emission region would become 47 times the quoted value for PKS 1510-089, reaching $R = 3.87 \times 10^{14}$. Four of the five smallest size limits are from FSRQs, out of a total of eight FSRQs overall, and four of the five largest limits belong to BL Lac objects, although there are not enough objects in the sample to determine whether FSRQs have smaller emission region limits overall than BL Lac objects. Since the size limits are proportional to the redshift-corrected e-folding times, the same is approximately true of the redshift-corrected smallest e-folding times as well.

The e-folding rise and decay time histograms for Fermi data are shown in Figures 2.4 through 2.7. The rise time histograms all show a very similar structure, sharply rising to a peak below 5 days and then falling off. This shows that between the majority of bins, for each of these sources, a variability timescale of between 1 and 10 days occurs. The decay time histograms appear to exhibit a structure symmetrical to that of the rise time histograms, which does not allow us to directly infer any of the differences between the mechanisms for increasing and decrasing flux in AGN. It may be that any differences

in the mechanism are simply masked by the statistical distribution of e-folding times, however. For those sources which did not have enough surviving bins to plot an e-folding histogram of any apparent value, such as I Zw 187 and H 1426+428, it can be noted that the observed smallest e-folding times are much higher than for those sources that have many surviving bins. The implication of this is that it is the lack of data, and not a significant physical difference, which leads to the differences in the observed e-folding times. The explanation for this is likely that the average distance in time between data points is larger when there are fewer data points, and as discussed previously the temporal resolution limits the smallness of the e-folding times.

2.4 Duty Cycles

Flux duty cycles for Fermi LAT data are shown in Figures 2.8 and 2.9. Sources MRK 180, I Zw 187, 1H 0414+009, PKS 0528+134 and H 1426+428 are excluded due to the low number of bins remaining after the TS threshold was applied. The number of bins used in the histogram in each case varied depending on the range of the flux values, as well as the number of entries. The result is that the graphs have been manually normalised to a certain degree, with the peak bins in each case containing on the order of 10 entries.

The duty cycles for daily-binned Fermi LAT data are shown in Figures 2.8 and 2.9. Only 14 of the 19 sources are shown, with 4C 71.07, H 1426+428, Mrk 180, PKS 0528+134 and PKS 2005-489 being excluded. These sources had fewer than 100 remaining bins after the TS threshold was imposed, and so their duty cycles contained very little useful information. The majority of the remaining sources display a clear structure in the distribution of fluxes, with the integrity of the visible structure being seemingly related to the total number of entries in each duty cycle. In those cases where the structure deviates from the simple case, there are two common differences: first, the structure at or below the peak is most visibly affected in most cases; and second, there are often non-zero bins at fluxes above the edge of the visible structure. The first observation is likely attributable to the fact that the errors are larger in proportion to the flux at very low values, meaning that the bin in the histogram that a given data point is assigned to is more variable at lower fluxes. A lower flux is also more likely to be accompanied by a lower TS value, meaning that a number of low-flux points will be removed in all cases and therefore that the statistical distribution may not hold as strongly. The second previously mentioned observation is likely explained by those periods in time over which sources experience increased flux:

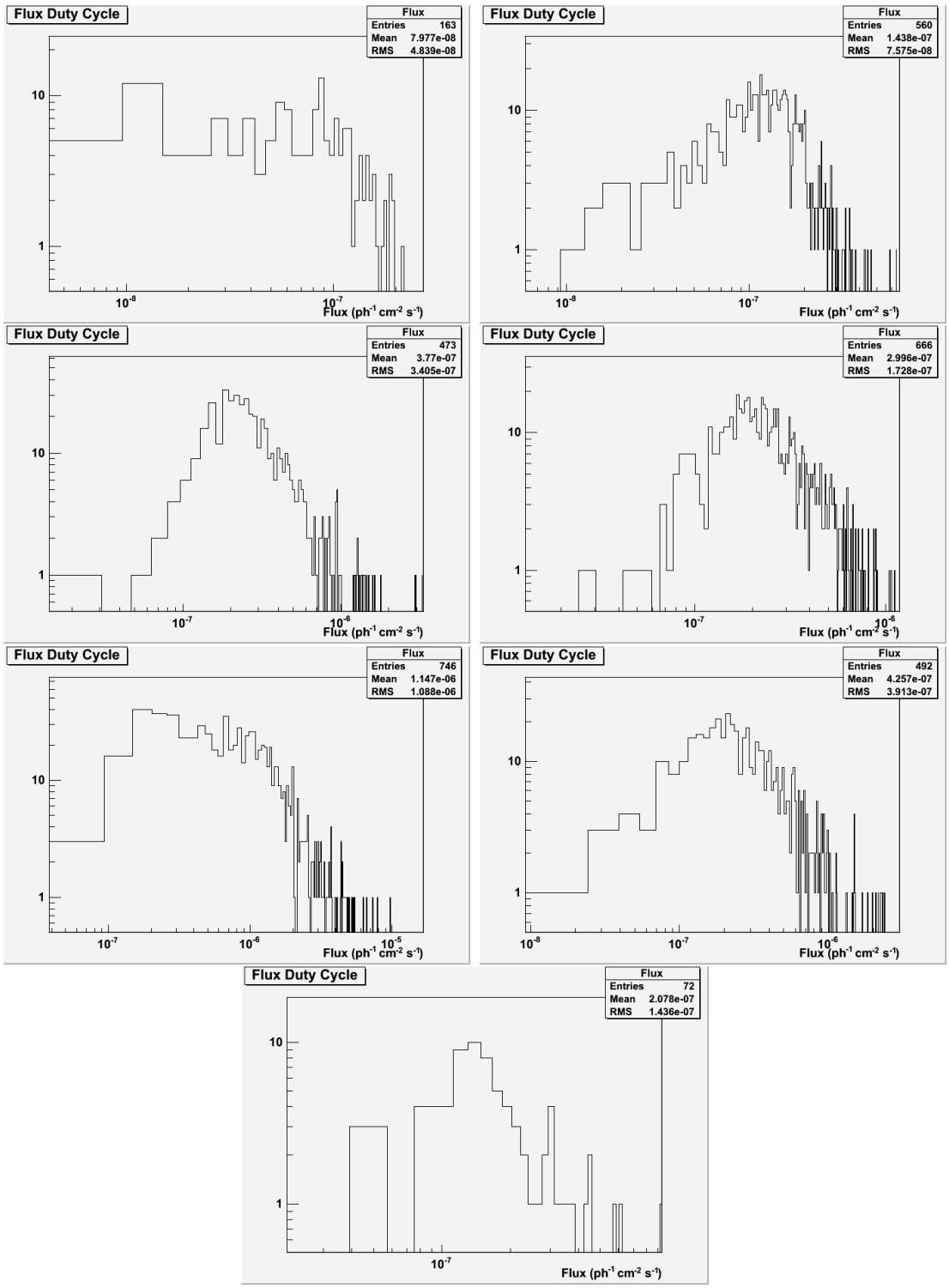

Figure 2.8 *γ-ray Flux duty cycles for seven sources, plotted using daily-binned Fermi data. Left to right from top: 1ES 1959+650, 3C 66A, 3C 273, 3C 279, 3C 454.3, 4C 21.35, 4C 71.07.*

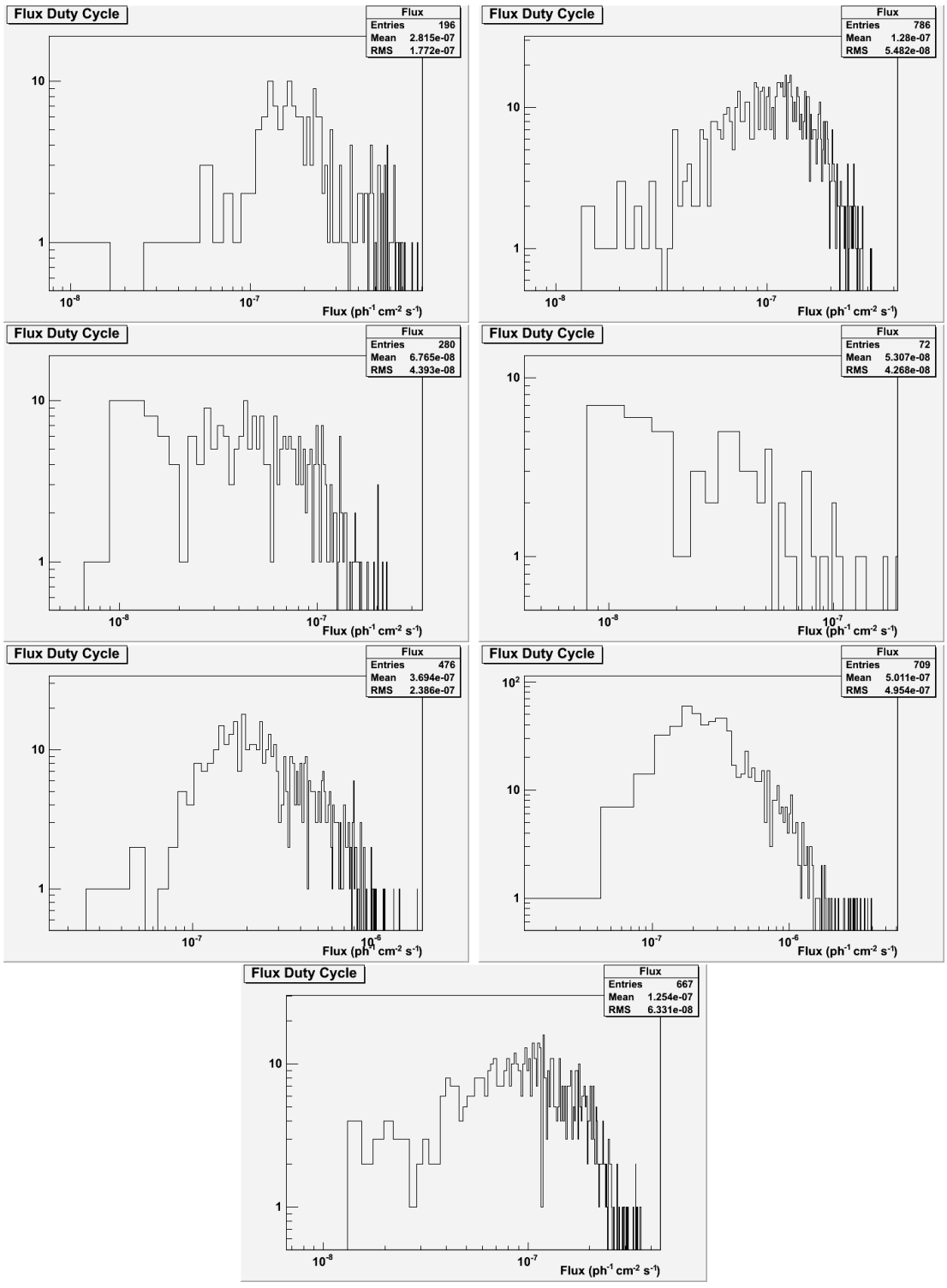

Figure 2.9 *γ-ray Flux duty cycles for seven sources, plotted using daily-binned Fermi data. Left to right from top: AO 0235+16, Mrk 421, Mrk 501, PKS 2005-489, PKS 1502+106, PKS 1510-089, PKS 2155-304.*

periods of flaring activity. The fact that these bins in the duty cycle fall at higher fluxes than the visible statistical distribution implies that they are extraordinary occurrences, and most likely caused by different physical phenomena (or by different intensities of the same phenomena) than the majority of the rest of the points. An example of such a change would be the onset of an acceleration/cooling scenario as described in Section 2.5. The sources which best display these higher flux irregularities are 3C 66A, 3C 273, 3C 454.3, 4C 21.35, PKS 1502+106 and PKS 1510-089. Of these sources, all except 3C 66A have clearly identifiable flaring regions in their light curves, as shown in Figures 2.1, 2.2 and 2.3. This provides further evidence that the higher flux irregularities in the duty cycles correspond to flaring activity.

2.5 Flux vs. Γ

Graphs showing the flux plotted against the photon index for each source, using LAT data, are shown in Figures 2.10, 2.11 and 2.12. PKS 0528+134 is excluded due to having been modelled with a log-parabola model rather than a power-law model, and thus having no Γ values to report. Graphs show the flux of each daily bin for a given source plotted against the photon index Γ for that bin. The value of Γ for each bin comes from Eq. 1.1 fitted over the averaged state of the spectrum for that bin. The plots for sources 1ES 1959+650, 1H 0414+009, H 1426+428, I Zw 187, Mrk 180, Mrk 501, PKS 0528+134 and PKS 2005-489 do not display sufficient structure to warrant a specialised fit, and so a linear fit has been applied to the entirety of the data. The remaining sources display structure at higher fluxes, and so only fluxes above a minimum cut-off flux (shown on these graphs) have been used to fit the line in these cases. The equation for the linear fit is shown on all graphs.

The plots of flux versus the spectral index Γ for the γ-ray energies of an AGN can provide useful information regarding the way it acquires and reacts to energy. In a situation where the spectrum becomes harder as flux increases, known as a harder-when-brighter (HWB) trend, the system can be considered as being analogous to a black body emitter. A black body at with any heat energy emits photons, with the exact nature of the emissions depending on the temperature of the body. The emissions increase in intensity as the temperature increases, as one would expect; the average energy of the emitted photons also increases, however, such as a heated metal object transitioning from red- to white-hot. Since a harder spectrum denotes more photons being emitted at higher energies, this

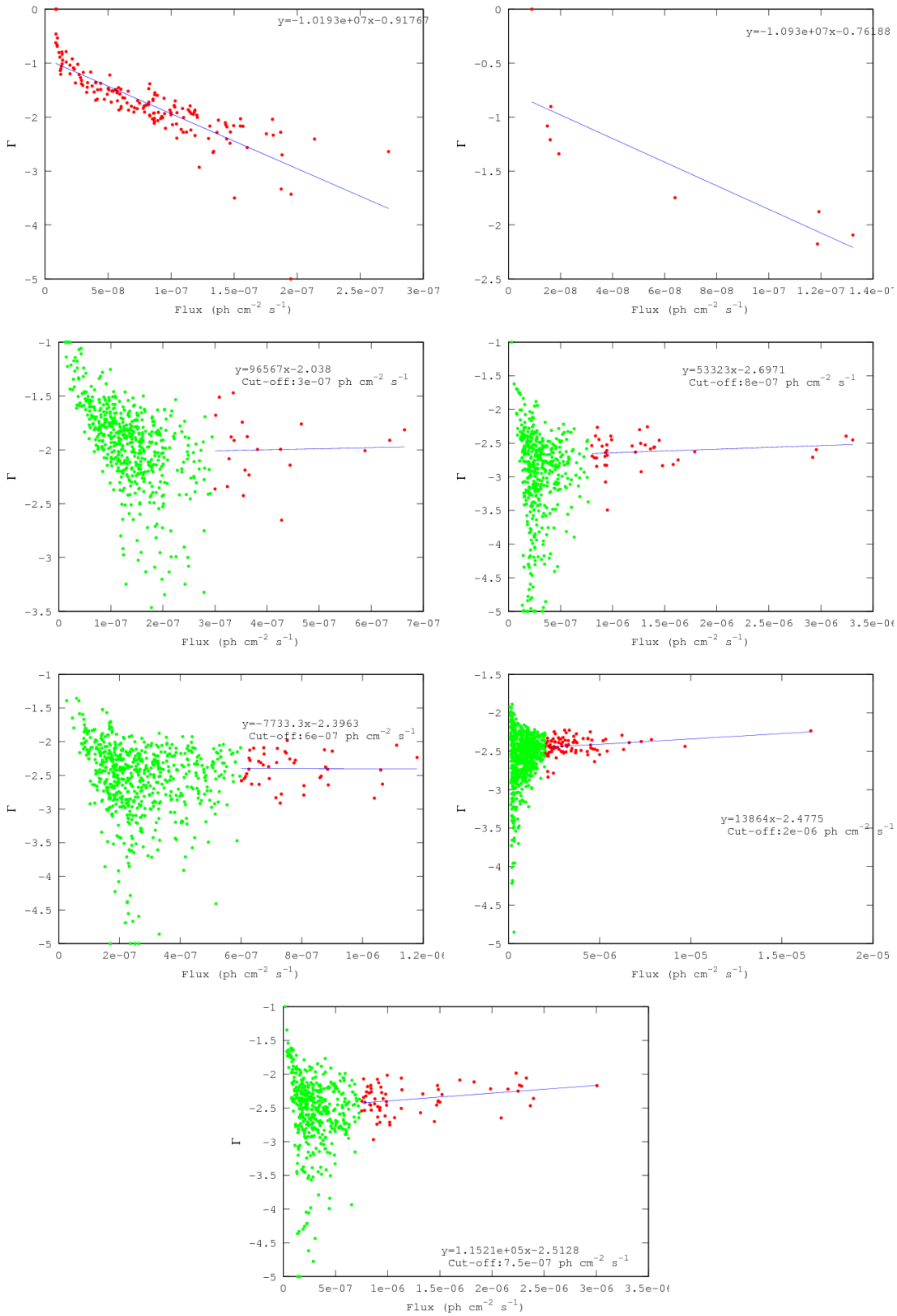

Figure 2.10 *The flux plotted against the photon index* Γ *of each bin, for daily binned Fermi data from seven sources. Linear fits are shown, with noted equations. Lower limits on the flux are shown if utilised. Red points indicate those data used to fit the line. Left to right from top: 1ES 1959+650, 1H 0414+009, 3C 66A, 3C 273, 3C 279, 3C 454.3, 4C 21.35.*

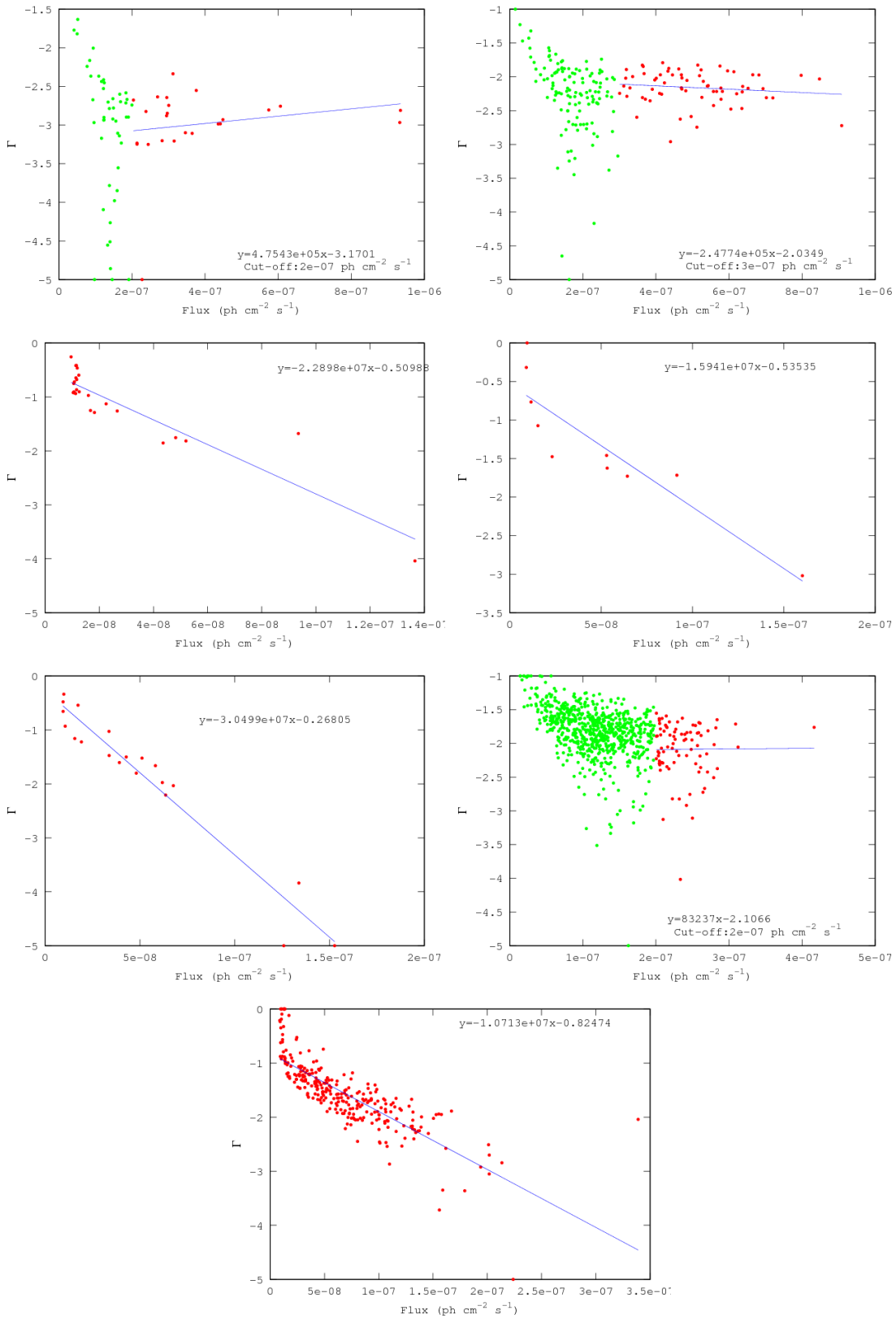

Figure 2.11 *The flux plotted against the photon index Γ of each bin, for daily binned Fermi data from seven sources. Linear fits are shown, with noted equations. Lower limits on the flux are shown if utilised. Red points indicate those data used to fit the line. Left to right from top: 4C 71.07, AO 0235+16, H 1426+428, I Zw 187, Mrk 180, Mrk 421, Mrk 501.*

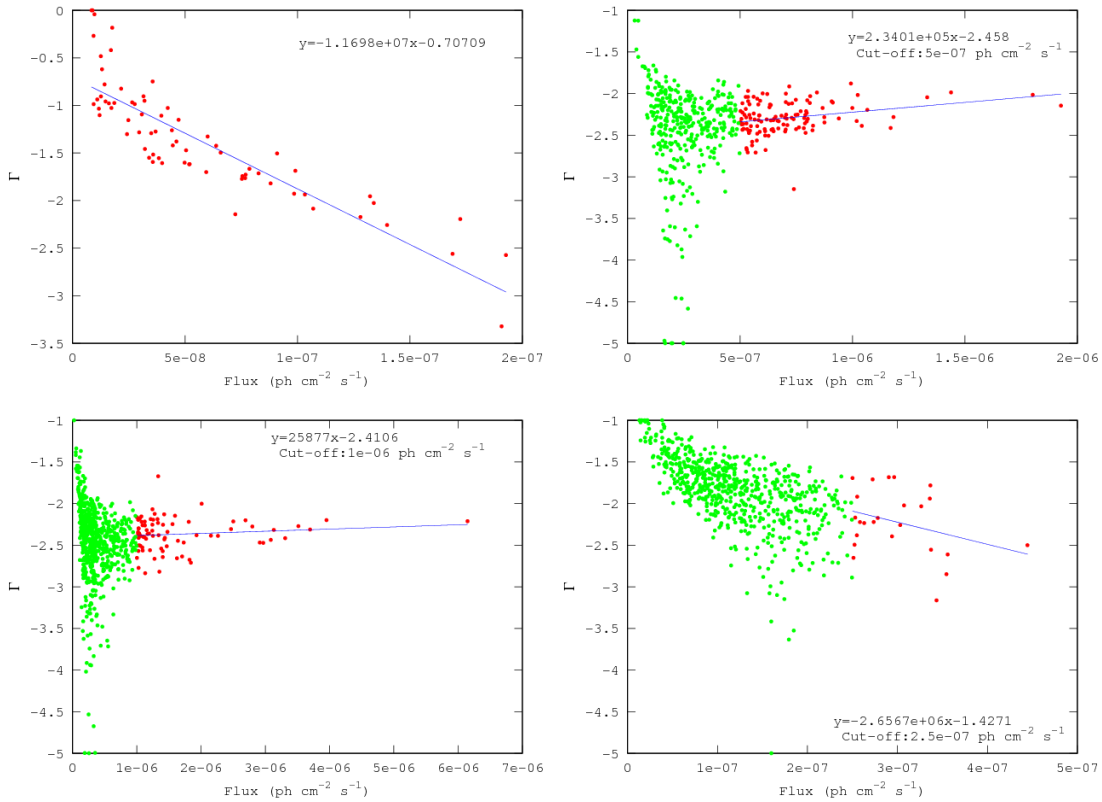

Figure 2.12 *The flux plotted against the photon index* Γ *of each bin, for daily binned Fermi data from four sources. Linear fits are shown, with noted equations. Lower limits on the flux are shown if utilised. Red points indicate those data used to fit the line. Left to right from top: PKS 2005-489, PKS 1502+106, PKS 1510-089, PKS 2155-304.*

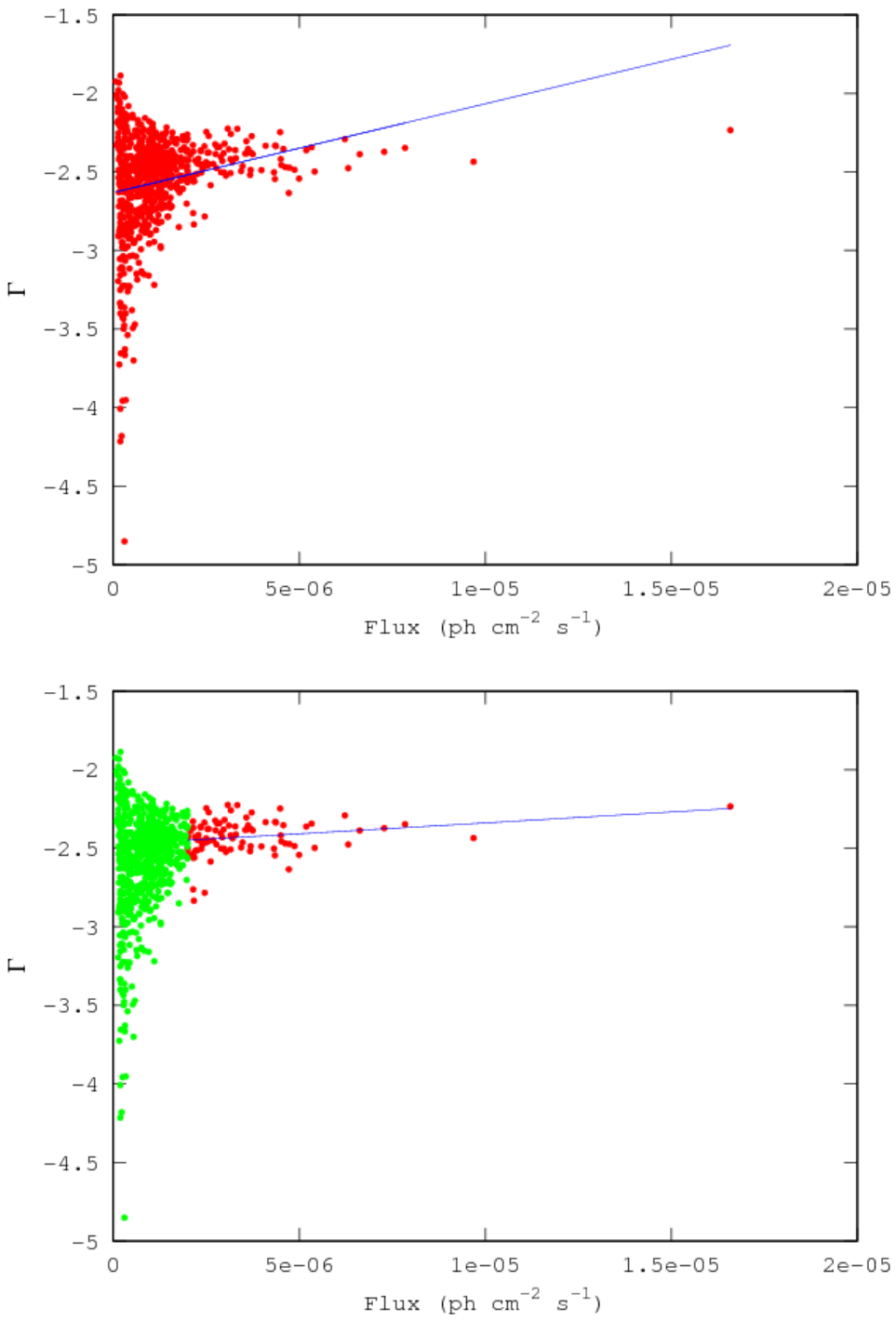

Figure 2.13 *Flux vs. spectral index plots illustrating the difference in fit of non-truncated vs. truncated data. The top image shows data from 3C 454.3 with all data used to fit, while the bottom shows the fit using only those data corresponding to fluxes above* 2×10^{-6} *ph* cm^{-2} s^{-1} *(red points) and the unused green points.*

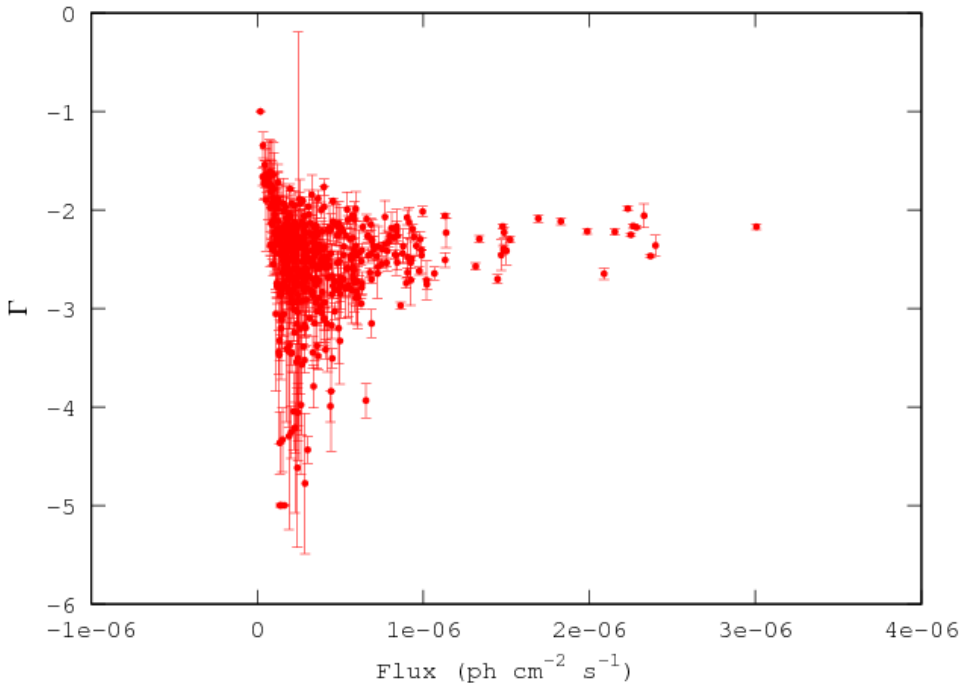

Figure 2.14 *Flux vs. spectral index plot of 4C 21.35 illustrating the common 'triangular' structure of the plot, also showing the errors of* Γ *at different regions.*

is analogous to the increase in average energy experienced by the emitting black body. A HWB trend therefore signifies an acceleration and cooling scenario occurring in the AGN [24], particularly in the jets since this is the primary source of γ emissions.

A HWB trend, if one exists, can be shown to exist by analysing the flux versus photon index plots. If such a trend exists, one would expect to see higher (less negative) values for Γ at higher values of flux, particularly at the highest fluxes which would most likely correspond to flaring states. To this end, a simple line may be fitted to the data, with the gradient of the line providing a numerical basis for determining whether a HWB trend exists. This line may be fitted to the entirety of the data, but in practice there is often a large spread of Γ values at lower fluxes. Given that a HWB trend would exist in most cases primarily in the region of the higher flux, it is often better to remove the data below a certain flux from the fitting, allowing the higher flux to dominate. This ensures that the fit is calibrated to those regions, and does in fact correspond to the HWB trend if it exists. The value of the cut-off flux has an effect on the final fit, with lower values tending to align the fit to the spread of Γ values at low fluxes, as shown for 3C 454.3 in Figure 2.13. The top image shows a linear fit using the entirety of the data set, while the bottom shows a fit using those data with fluxes above 2×10^{-6} ph cm^{-2} s^{-1}. A cut-off flux must therefore be chosen which maximises the number of flaring-type data points included and

minimises the number of data points from a more quiescent state. Since the objective in this instance is primarily to identify (not quantify, per se) a HWB trend, the sign of the gradient of the linear fit is the main point of interest. Therefore, it is not required to have a rigid algorithm for the choice of cut-off flux, as would be necessary to numerically compare the trends of different sources.

The flux versus Γ plots are shown in Figures 2.10, 2.11 and 2.12, with linear fits applied to certain regions of data. In some cases, particularly the dimmer sources, the fits do not necessarily correspond to the actual trend of the data. Where a clear trend was available, the visible trend was isolated for the linear fitting by applying a cut-off flux; in some of these cases, however, the fit still does not appear to be a good indicator of any possible trend. Examples of this are the plots for Mkn 421 and PKS 2155-304. The sources 1ES 1959+650, 1H 0414+009, H 1426+428, I Zw 187, Mrk 180, Mrk 501, PKS 0528+134 and PKS 2005-489 do not display sufficient structure to warrant applying a cut-off flux, and so the linear fit was applied to the entirety of the available data in these cases. None of these sources show any increase in hardness with increased flux, rather appearing to become softer. This apparent result could possibly be a selection effect based on the TS threshold, however, with points that would have increased the visible structure removed from the final results due to this criterion. The bright sources all display a 'triangular' distribution such as is visible in Figure 2.14. The errors on the lower 'limb' in this plot show the relative magnitude as compared to errors in other parts of the structure, with the larger errors likely corresponding to bins with lower TS values. The dimmest sources do not display this limb, or indeed the limb extending to regions of higher flux, in most cases. This implies that, for the dimmest sources, the apparent softer-when-brighter trend is simply equivalent to the upper limb of the triangular structure seen in the brighter sources. Additionally, regions of singular or a few points such as the highest flux point on the plot of Mrk 501 (in Figure 2.11) suggest that the higher flux limb may simply be unrepresented in these cases, supporting this hypothesis.

The brighter sources shown in Figures 2.10, 2.11 and 2.12 invariably display the limb extending to higher fluxes. This limb does not contain the points at which the spectrum was hardest for any source, but it does represent the behaviour of each source at the highest levels of activity. All sources with applied cut-off fluxes, except AO 0235+16, 3C 279 and PKS 2155-304 display a linear fit to the high-flux limb with a positive gradient, denoting HWB behaviour in these regions. The exemplar of this is 3C 454.3, with a single point at markedly higher flux falling very close to the fitted line. For the sources 3C 66A, 3C 273, 3C 454.3, 4C 21.35, 4C 71.07, Mrk 421, PKS 1502+106 and PKS 1510-089 we can therefore say that HWB behaviour was observed, and posit an acceleration/cooling

scenario occurring at regions of higher flux. This effect is most likely caused by a change in the energy input to the system, such as a change in the accretion rate [14]. HWB behaviour has been previously observed at high γ-ray fluxes in 3C 454.3 [4, 5], 3C 273 [28], 4C 21.35 [30] and PKS 1510-089 [2], agreeing with the results in this case. AO 0235+16 has also been observed to exhibit HWB behaviour [4], as has PKS 2155-304 [7, 12] conflicting with the observed result in these cases.

The fact that HWB trends have been previously observed for AO 0235+16 and PKS 2155-304, while not being found to display them here, has some interesting physical interpretations. Firstly, it must be noted that Aharonian et al. and Brown (2006) both used a different energy range to that implemented here, utilising VHE (> 100 GeV) γ emission detected by the HESS telescope [22]. Both AO 0235+16 and PKS 2155-304 are BL Lac objects, which means that the energy range of the LAT likely falls on or very near the inverse-Compton peak. For HESS, however, the observations would fall well into the high-energy tail of these sources, and so any variability would be accentuated as discussed in Section 2.3. This could explain why HWB behaviour was observed primarily for FSRQs in this study. A second explanation for the discrepancy between observed HWB trends in these cases is that the time periods for these observations are different. Aharonian et al. and Brown (2006) worked with data from before 2006, while the Fermi observations utilised here begin in late 2008. This could imply that the dominant mechanism for γ emission from these two sources has changed over this period, an indicator that the inner workings of AGN may vary with time.

Chapter 3

X-ray Analysis

3.1 Methods

For Swift BAT and XRT data, the e-folding timescales were calculated for each bin in a manner similar to that of Section 2.2. The smallest e-folding times for these data sources were thus found.

Flux duty cycles were plotted for Swift BAT data, as with the Fermi data. In the Fermi analysis in Chapter 2, data points were only included if the model used to fit them had at least a 3σ probability over the lack of a model. This ensured that each point was a good representation of the data used to create it. In contrast to the Fermi analysis, where the data were processed specifically for this study, the BAT and XRT data were obtained in a pre-processed format. There was therefore no control over the modelling, data selection or quality checks for these data, and so the points and their errors were the only indication of the quality of data. There may therefore be modelled points in these datasets which do not accurately represent the data, or data may have been included that have introduced systematic errors or observational biases. Ideally, raw data would have been obtained and processed for this thesis like the Fermi data were.

3.2 Light Curves and Variability

The light curves from Swift XRT data for each source are shown in Figures 3.1 and 3.2. The smallest e-folding rise timescales found for each source using daily-binned BAT data are shown in Table 3.1 with their associated errors. Approximate MJD values, corre-

sponding to the end bin of the increase, are also shown.

Histograms of the Swift XRT e-folding rise times are shown in Figures 3.3 and 3.4. The corresponding decay times are shown in Figures 3.5 and 3.6. The smallest e-folding rise and decay timescales found for each source using XRT data are shown in Table 3.2 with their associated errors. The closest MJD values to each timescale are also shown.

Source	τ_{rise} **(days)**	**MJD**	τ_{decay} **(days)**	**MJD**
1ES 1959+650	0.13 ± 0.11	54315	0.14 ± 0.2	54995
1H 0414+009	0.15 ± 0.14	54685	0.1 ± 0.4	55507
3C 66A	0.1 ± 0.2	54816	0.2 ± 0.3	55993
3C 273	0.15 ± 0.18	55823	0.22 ± 0.11	55925
3C 279	0.18 ± 0.12	55037	0.19 ± 0.13	53604
3C 454.3	0.09 ± 0.06	54309	0.1 ± 0.3	54308
4C 21.35	0.1 ± 2.0	55263	0.1 ± 0.3	55262
4C 71.07	0.14 ± 0.08	56170	0.13 ± 0.14	53646
AO 0235+16	0.16 ± 0.06	53912	0.1 ± 0.4	56132
H 1426+428	0.16 ± 0.15	53517	0.17 ± 0.17	56008
I Zw 187	0.1 ± 0.4	56023	0.2 ± 0.5	55783
Mrk 180	0.13 ± 0.08	55510	0.13 ± 0.19	55509
Mrk 421	0.09 ± 0.05	53427	0.09 ± 0.07	53426
Mrk 501	0.15 ± 0.08	55792	0.2 ± 7.0	54791
PKS 0528+134	0.2 ± 0.3	55821	0.2 ± 0.3	55781
PKS 2005-489	0.13 ± 0.07	55137	0.13 ± 0.15	55134
PKS 1502+106	0.2 ± 0.3	56014	0.2 ± 0.3	53737
PKS 1510-089	0.1 ± 0.3	55060	0.12 ± 0.19	55059
PKS 2155-304	0.14 ± 0.19	54815	0.2 ± 0.3	56026

Table 3.1 *The smallest e-folding times for Swift BAT data for each source, with errors, calculated using Eq. 1.2 on daily bins. All values are given in days.*

Table 3.2 shows the smallest rise and decay e-folding times for Swift XRT data. The smallest variability timescales previously observed are of the order of 2000 s [18], but the smallest e-folding times calculated here range from the order of a few seconds to a few hundreds of seconds. Due to the lack of information about the manner in which these data were created, for example any modelling of raw data, the possibility that these data are inappropriate for calculating e-folding times must be considered. When looking at the light curves for XRT data in Figures 3.1 and 3.2, it is apparent that there are large proportions of flux change over very small periods of time, a fact which would indeed

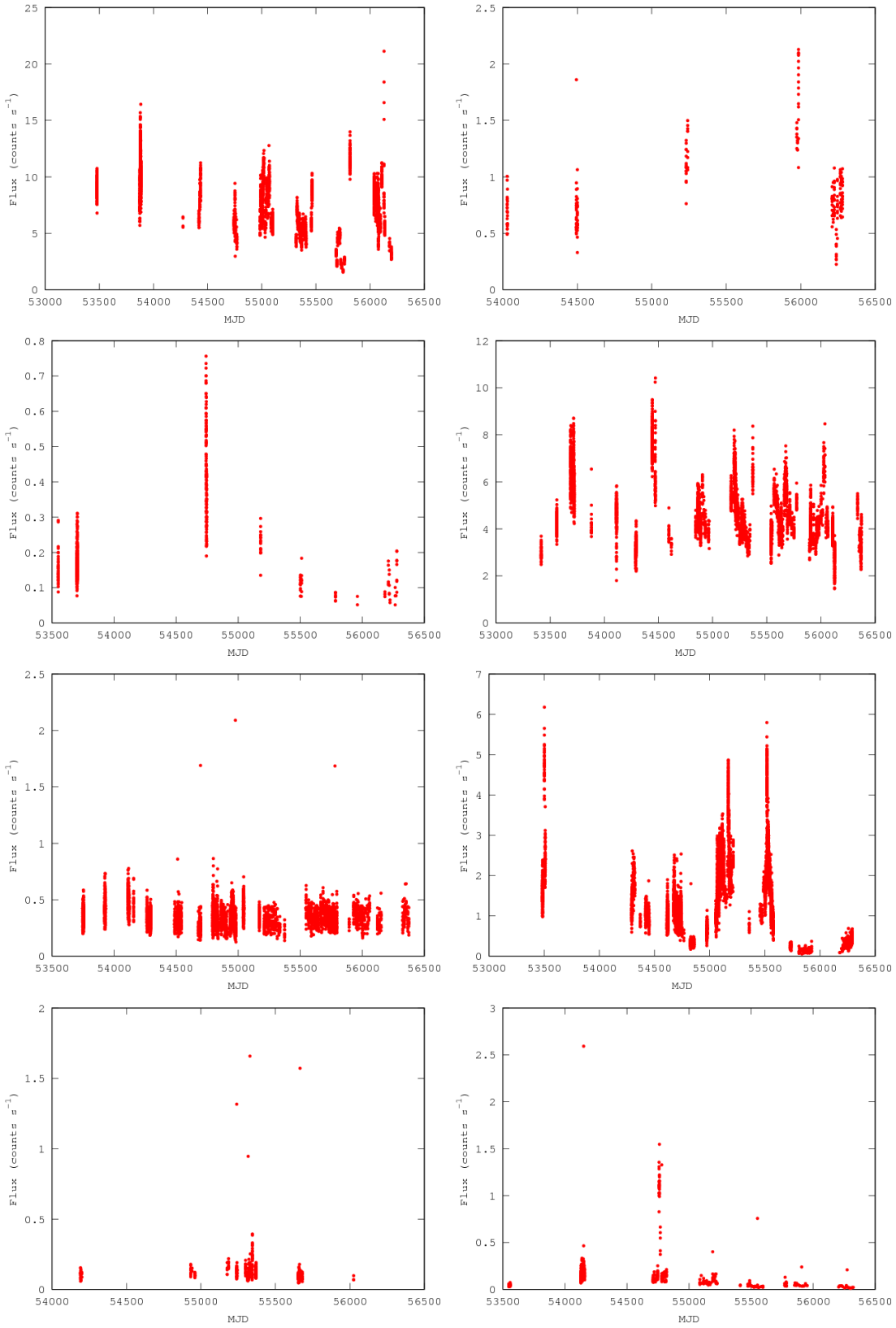

Figure 3.1 *Light curves for eight sources using Swift XRT data. Left to right from top: 1ES 1959+650, 1H 0414+009, 3C 66A, 3C 273, 3C 279, 3C 454.3, 4C 21.35, AO 0235+16.*

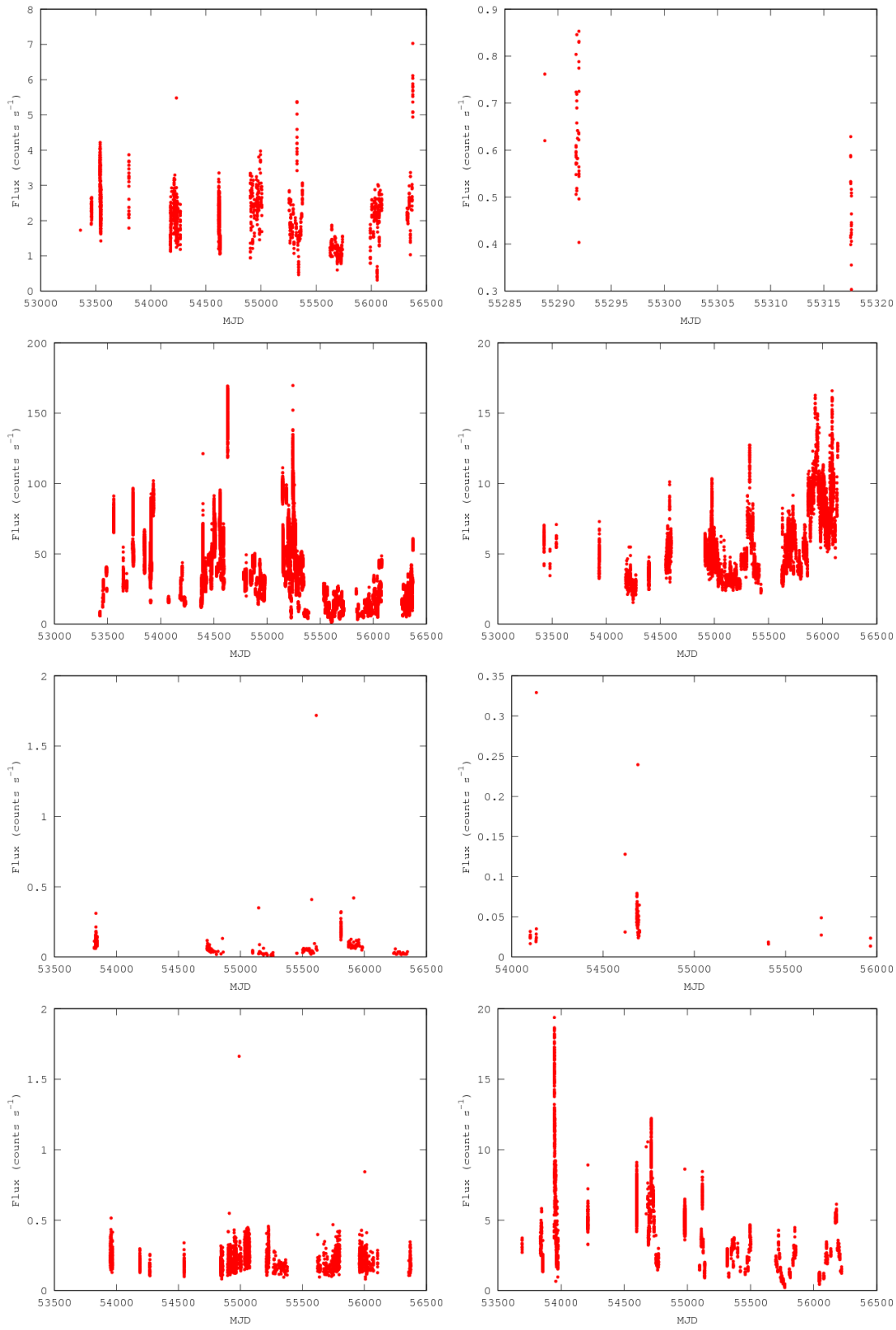

Figure 3.2 *Light curves for eight sources using Swift XRT data. Left to right from top: H 1426+428, I Zw 187, Mrk 180, Mrk 421, Mrk 501, PKS 0528+134, PKS 1502+106, PKS 1510-089, PKS 2155-304.*

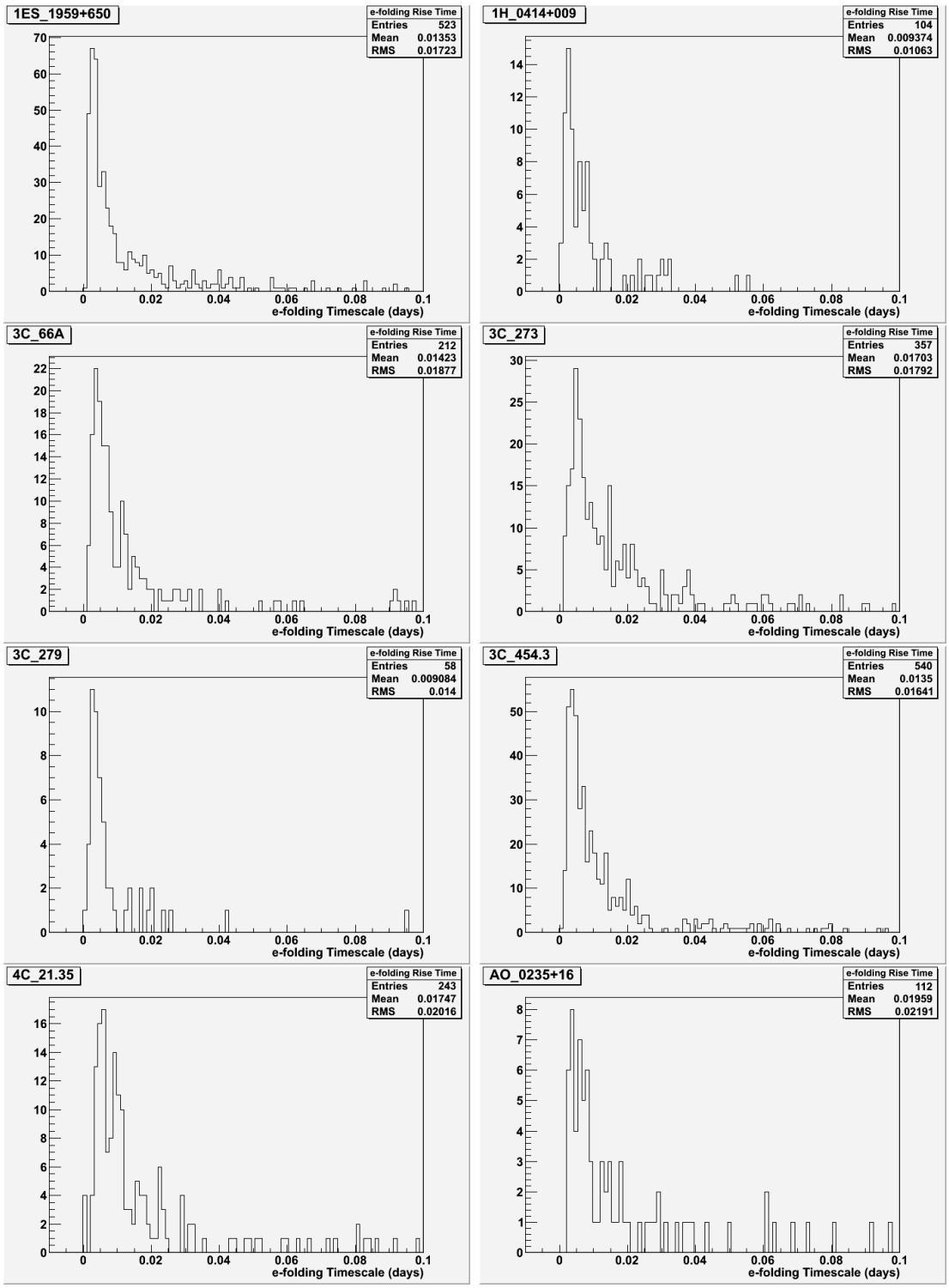

Figure 3.3 *Histograms of the x-ray e-folding rise times for eight sources, calculated using Swift XRT data. Left to right from top: 1ES 1959+650, 1H 0414+009, 3C 66A, 3C 273, 3C 279, 3C 454.3, 4C 21.35, AO 0235+16.*

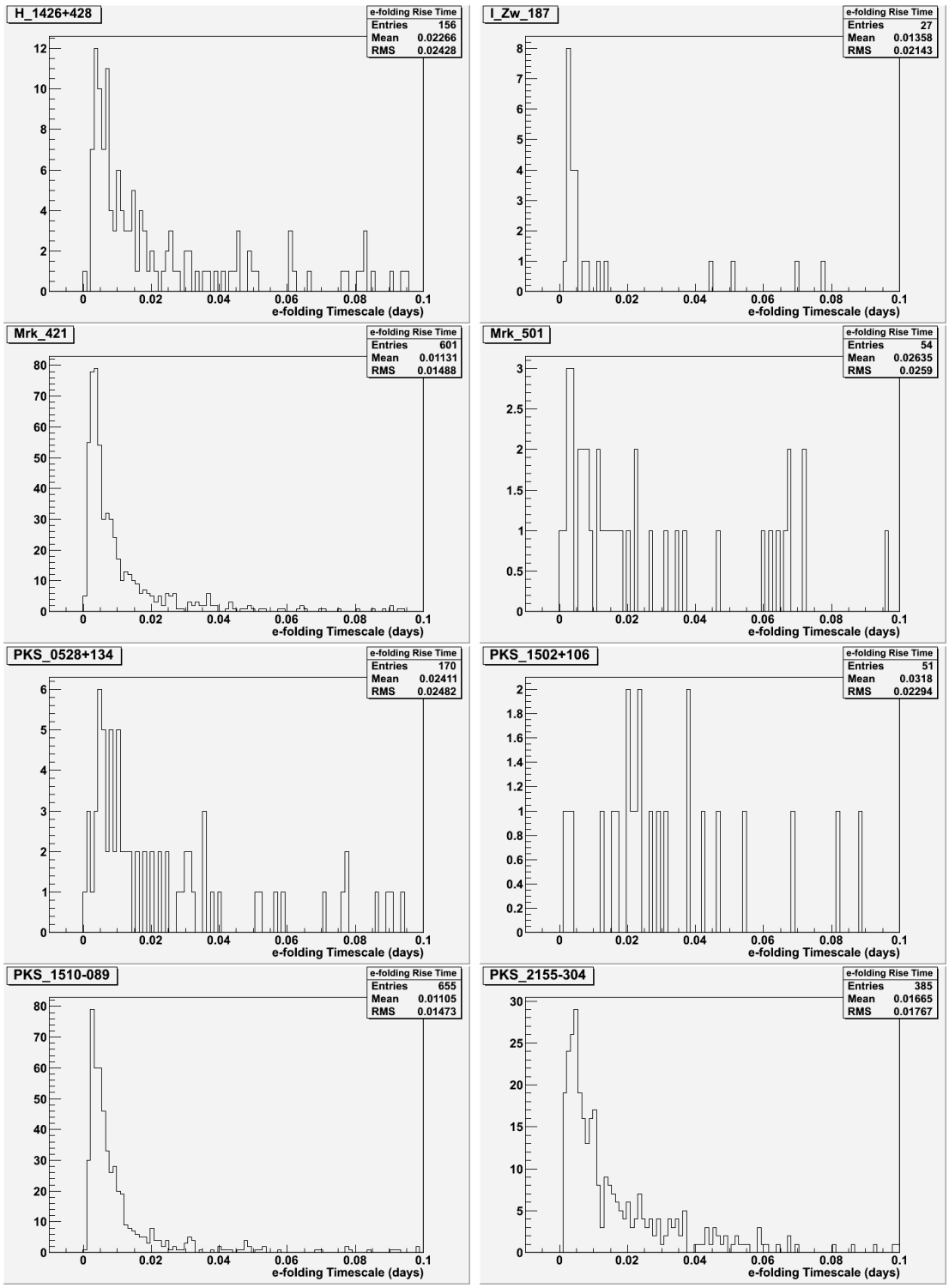

Figure 3.4 *Histograms of the x-ray e-folding rise times for eight sources, calculated using Swift XRT data. Left to right from top: H 1426+428, I Zw 187, Mrk 180, Mrk 421, Mrk 501, PKS 0528+134, PKS 1502+106, PKS 1510-089, PKS 2155-304.*

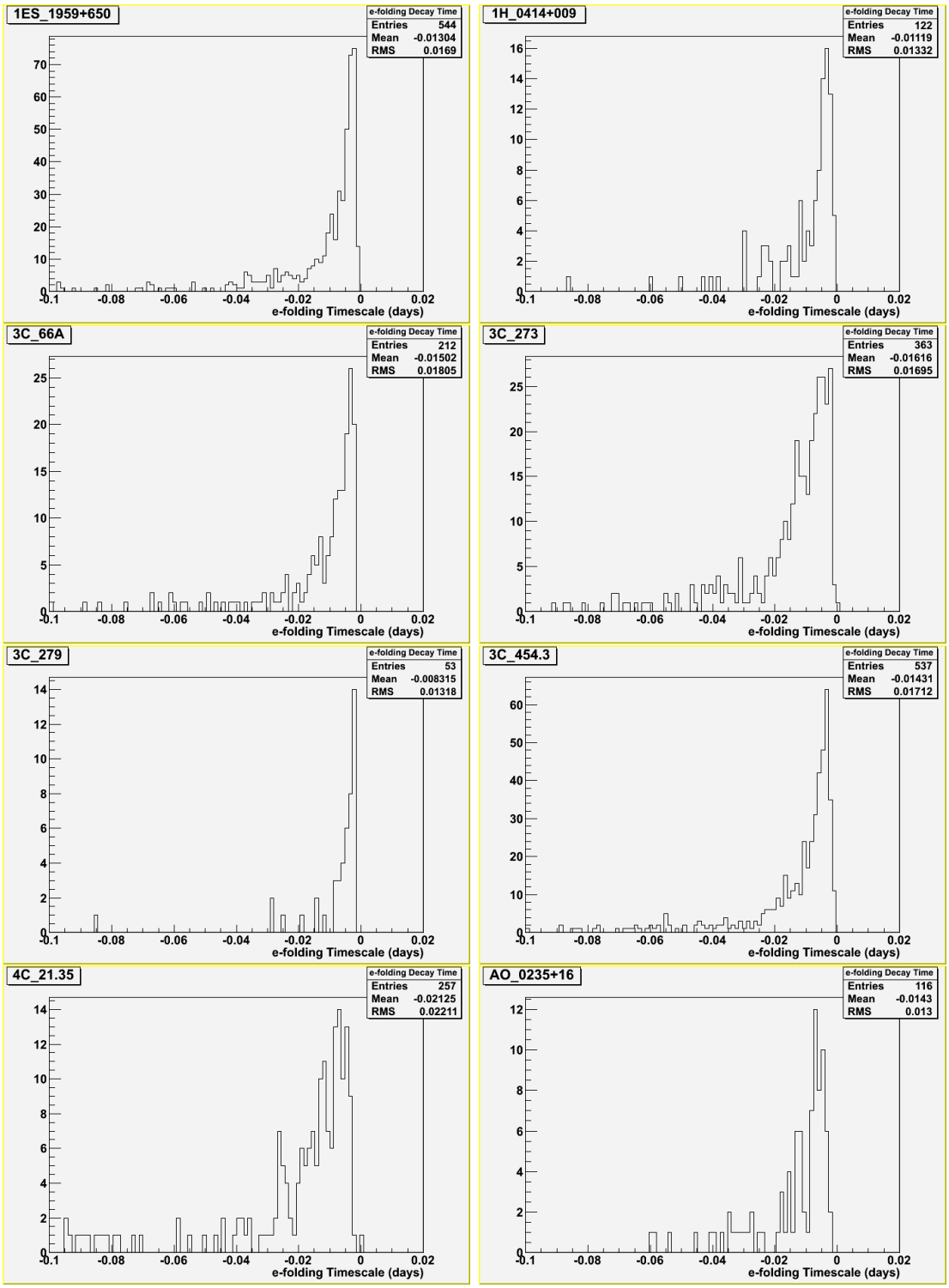

Figure 3.5 *Histograms of the x-ray e-folding decay times for eight sources, calculated using Swift XRT data. Left to right from top: 1ES 1959+650, 1H 0414+009, 3C 66A, 3C 273, 3C 279, 3C 454.3, 4C 21.35, AO 0235+16.*

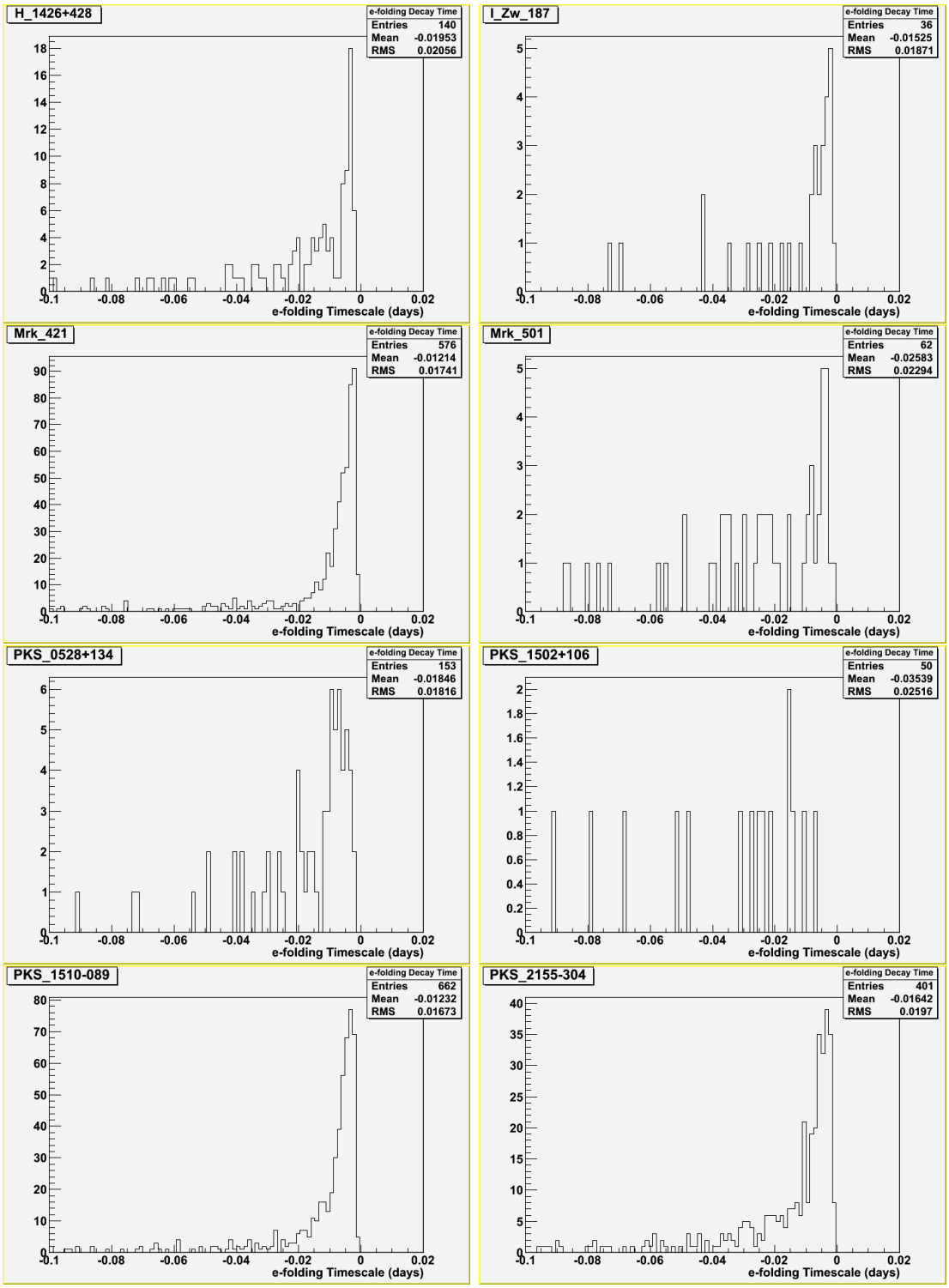

Figure 3.6 *Histograms of the x-ray e-folding decay times for eight sources, calculated using Swift XRT data. Left to right from top: H 1426+428, I Zw 187, Mrk 180, Mrk 421, Mrk 501, PKS 0528+134, PKS 1502+106, PKS 1510-089, PKS 2155-304.*

Source	τ_{rise} (sec)	MJD	τ_{decay} (sec)	MJD
1ES 1959+650	71 ± 5	56078.4	30.7 ± 1.8	55010
1H 0414+009	13.8 ± 1.8	54029	55 ± 8	54029
3C 66A	120 ± 30	54744.4	130 ± 30	54745.3
3C 273	86 ± 6	54443.1	29 ± 2	53689.1
3C 279	4.4 ± 0.8	53926.5	3.1 ± 0.3	53925.5
3C 454.3	25 ± 14	54830.2	56 ± 8	54679
4C 21.35	39 ± 23	55329.1	12 ± 3	54191.5
AO 0235+16	22 ± 8	54150.8	130 ± 30	54150.9
H1426+428	31 ± 4	53546.4	52 ± 6	54232.2
I Zw 187	150 ± 20	55291.8	130 ± 30	55292
Mrk 421	65 ± 5	56312.6	52 ± 2	54398.4
Mrk 501	62 ± 4	55966.6	41 ± 6	54224.4
PKS 0528+134	60 ± 30	55612	210 ± 50	53835.1
PKS 1502-106	200 ± 500	54134.7	630 ± 130	55695.9
PKS 1510-089	26 ± 15	54989.7	51 ± 14	55746.8
PKS 2155-304	76 ± 11	56045.8	51 ± 7	53855.7

Table 3.2 *The smallest e-folding rise and decay times for Swift XRT data for each source, with errors, calculated using Eq. 1.2. All τ values are given in seconds.*

translate into very small e-folding times. This provides evidence for the assumption that the calculated e-folding times are correctly calculated from the data, but that the data may not be sufficient in accurately representing the activity of each source. This possibility is currently under further investigation, due to the large discrepancy between these and the previously reported results. The calculated e-folding times from the XRT data have been included for completeness.

In the unlikely case that the e-folding times calculated here are in reality indicative of a much smaller variability timescale, one possible explanation is based on the erratic nature of the binning of the XRT data. With no standard time interval, and taking into account the nature of the XRT observations that comprise the XRT data, the time interval between any two data points in the XRT data sets can be very small, on the order of seconds. In order for a variability timescale to apply to an entire emission region, the entire region would have to vary its flux over a given amount of time; but, given the ~ 2000 s results for variability timescales, the observed timescales here are too small for that to be occurring. Instead, it is possible that the flux variability observed between any two close data points is a result of localised changes in the emission region, and not

a change over the entire region. With this in mind, it may be that the e-folding times in Table 3.2 correspond to some sub-regions of the main emission region. This idea appears to be similar to that discussed in Papadakis and Lawrence (1993) [25]. This effect could possibly be combatted by averaging the XRT results more, for example by sorting them into bins of a standardised size, specifically as large as or larger than the ~ 2000 s previously mentioned. The averaged values in each bin would then better represent the emission region as a whole. The calculated sizes of emission regions are not shown in Table 3.2, but they range from 8.58×10^8 m to 4.26×10^{10} m.

The rise and decay e-folding time histograms for XRT data are shown in Figures 3.3 through 3.6. The histograms for I Zw 187, Mrk 501, PKS 0528+134 and PKS 1502+106 contain very few entries, and as such they convey only limited information. The rest of the histograms, however, each display a clear structure in the distribution of values. Similar to the Fermi histograms discussed previously, the histograms all display a similar structure, this time having the bulk of the entries falling between 0 and 0.02 days with a peak at 0.005 days. Again, like the Fermi histograms, the distributions of the decay timescales appear to be symmetrical to those of the rise timescales.

The smallest e-folding timescales from Swift BAT data are shown in Table 3.1. The smallest e-folding times all fall within a range of about 0.1 - 0.2, appearing very consistent over all sources. By contrast, the Fermi and XRT e-folding times show marked variation between sources. One explanation for this difference could be that the BAT data are noisy or error-dominated, which is a conclusion backed up by discussion on other facets of the used BAT data. On a close inspection of the values in Table 3.1, it can be seen that for the sources 3C 454.3, 4C 21.35, Mrk 180, Mrk 421, Mrk 501 and PKS 1510-089 the smallest rise time in fact occurs in the bin directly after the smallest decay time. This indicates that for these sources, the smallest variability timescales were centred around a single point, with this point being significantly lower than the two adjacent points. For daily-binned data, such as the Fermi data in this case, we would not expect any significant and unwarranted drops in flux, since the bins are averaged over a period of time. Indeed, for the Fermi data there are no instances of a single bin causing both the smallest rise and decay time. The fact that such a thing has occurred in the BAT e-folding times could be yet another indicator of the noisiness of the BAT data. Consequently, the BAT e-folding times are of limited usefulness, and size limits were not derived from these values.

3.3 Duty Cycles

The flux duty cycles plotted using Swift BAT data are shown in Figures 3.7, 3.8 and 3.9.

The duty cycles for daily-binned Swift BAT data are shown in Figures 3.7, 3.8 and 3.9. Of these duty cycles, all except 3C 273 display a very similar structure. This common structure consists of a 'plateau' of low flux points, with an ill-defined peak, a sharp decrease in the number of points with high fluxes, and a scattering of points at fluxes above the main structure. The plateau and ill-defined peak indicate that the duty cycle is in fact dominated by points of low flux, which seems to be in keeping with the prevalence of noise in the BAT monitoring data. In Section 2.4, the presence of points above the main structure in the duty cycles was linked to flaring activity in several sources. In this case, however, the BAT data display no clear instances of flaring behaviour, and yet the high-flux points exist for every duty cycle. This implies that these points are a result of the variation in the BAT data due to the lack of sensitivity, not an indicator of any physical behaviour. The only exception to the above structure is 3C 273, shown in Figure 3.7. This source displays a clear increase in the number of points up to a certain peak, with the high flux structure then being similar to that previously described. This indicates that 3C 273 may be the only source bright enough in the 10 - 150 keV energy range to overcome the inherent fluctuations in the BAT monitoring data. For this source, then, we can determine a mode flux of around 3×10^{-3} counts s^{-1}, but comparisons with other sources would be needed to determine more.

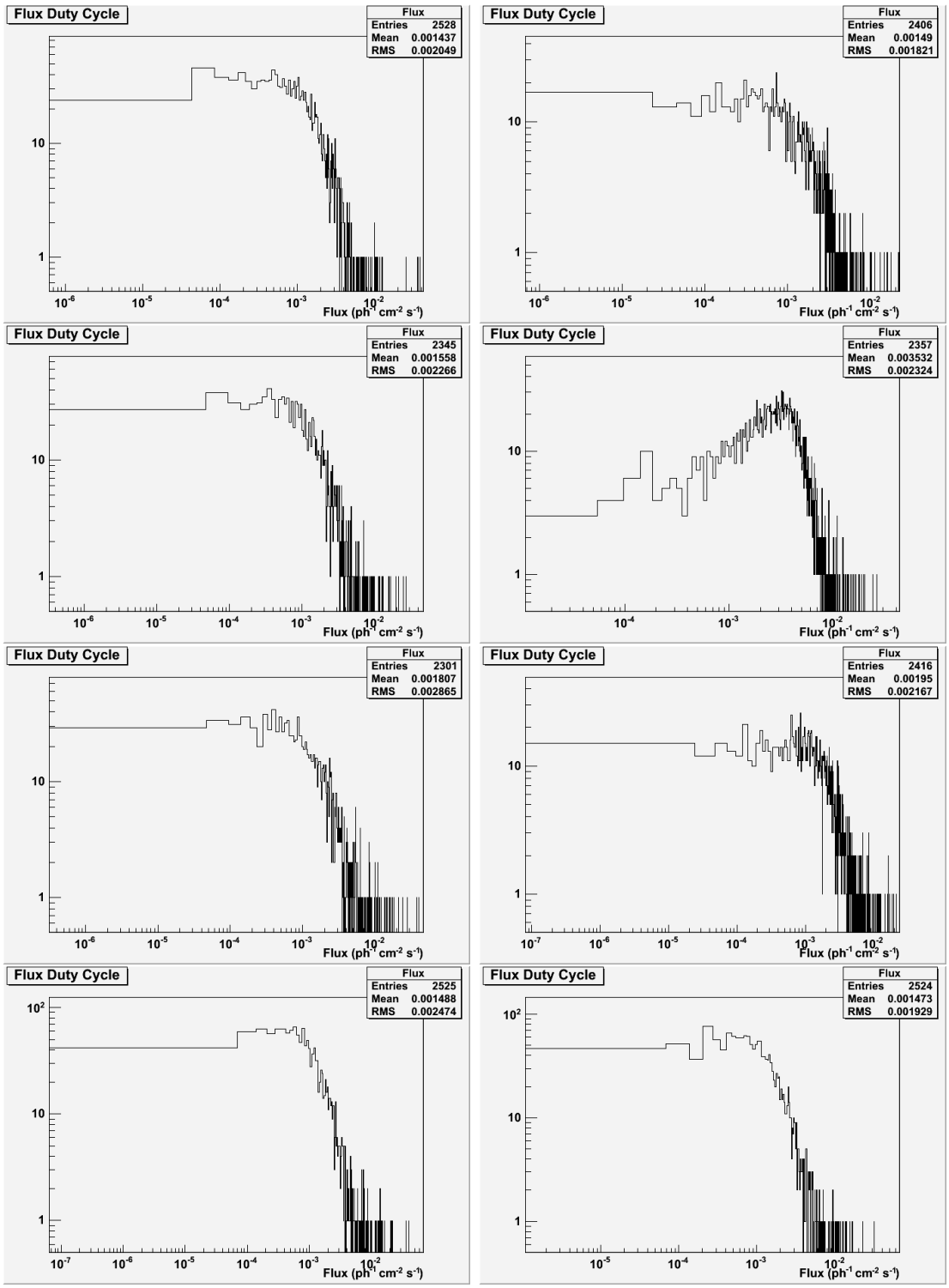

Figure 3.7 *Flux duty cycles for eight sources, plotted using daily-binned Swift BAT data. Left to right from top: 1ES 1959+650, 1H 0414+009, 3C 66A, 3C 273, 3C 279, 3C 454.3, 4C 21.35, 4C 71.07.*

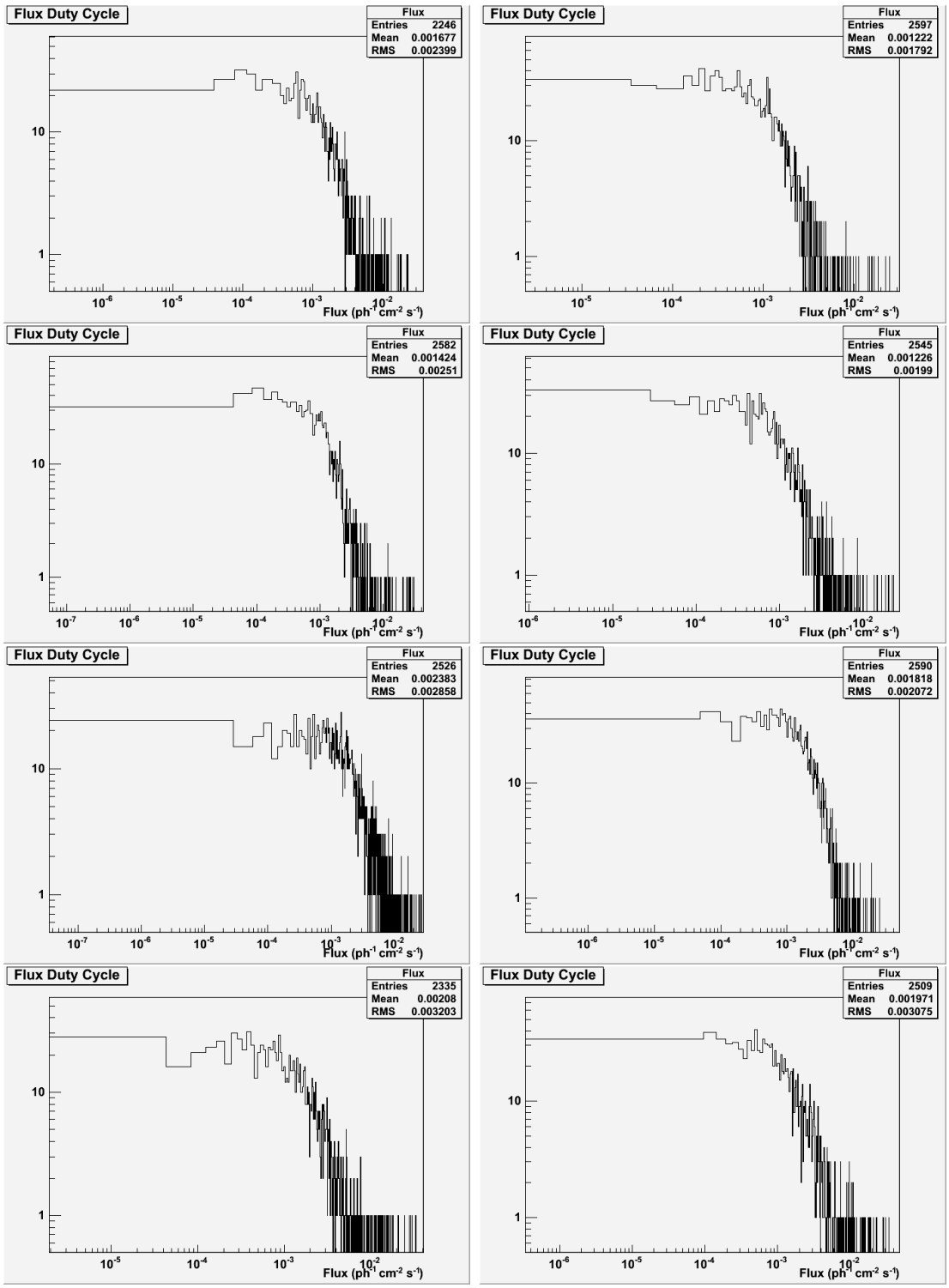

Figure 3.8 *Flux duty cycles for eight sources, plotted using daily-binned Swift BAT data. Left to right from top: AO 0235+16, H 1426+428, I Zw 187, Mrk 180, Mrk 421, Mrk 501, PKS 0528+134, PKS 2005-489.*

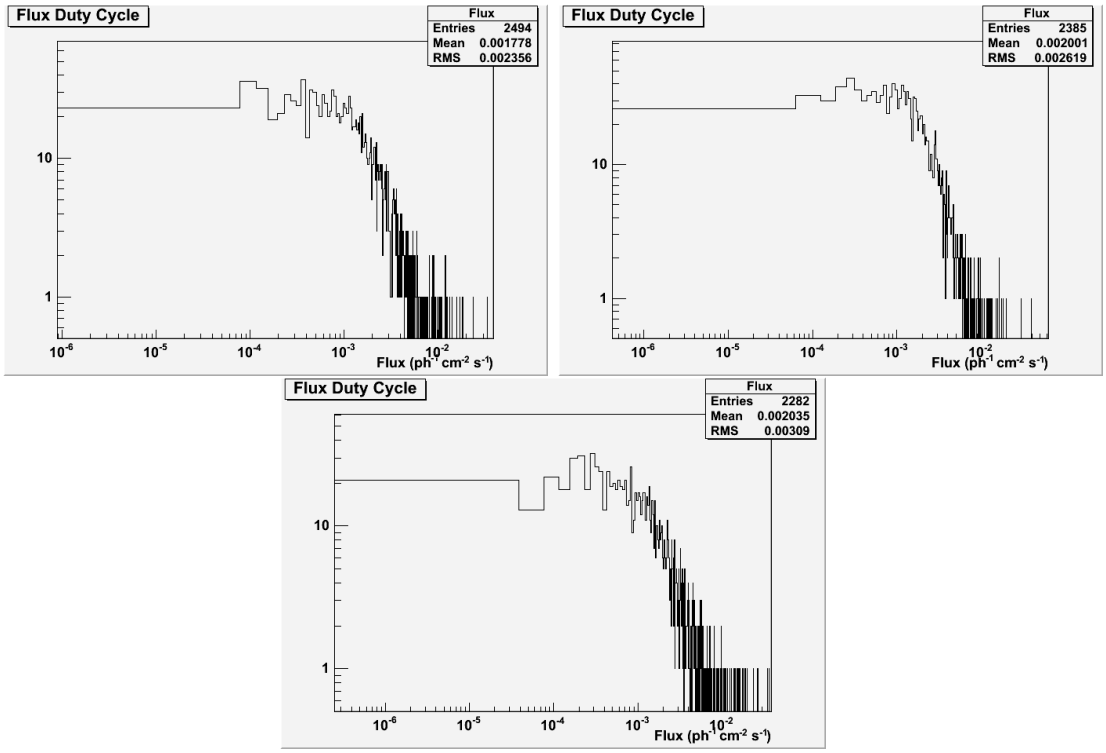

Figure 3.9 *Flux duty cycles for three sources, plotted using daily-binned Swift BAT data. Left to right from top: PKS 1502+106, PKS 1510-089, PKS 2155-304.*

Chapter 4

Multiwavelength Analysis

4.1 Discrete Correlation Function

4.1.1 Definition

It is often very helpful or necessary in physics and astronomy to have a measure of the correlation of two signals. When two signals have exactly simultaneous data points, each pair can be directly compared and a correlation (or lack thereof) easily discovered. In practice, however, it is very rare to find data sources where the two signals are so organised. This means that it is often necessary to compare one signal to a point interpolated between points of the other signal. This is undesirable, primarily because the interpolated data do not correspond to any measured data directly, and also because the values of the interpolated data depend on the function used to interpolate. It is therefore useful to find a function capable of determining correlations between signals that do not necessarily have simultaneous data points, or even the same distance between data points.
To this end, Edelson and Krolik [16] developed the discrete correlation function (DCF). The DCF is defined for a pair of points as

$$\mathrm{UDCF}_{ij} = \frac{(a_i - \bar{a})(b_j - \bar{b})}{\sqrt{(\sigma_a^2 - e_a^2)(\sigma_b^2 - e_b^2)}} \tag{4.1}$$

where $UDCF_{ij}$ is the individual (unbinned) DCF value, a_i and b_j are the two data sets, and the $\sigma_{a,b}$ and $e_{a,b}$ are the standard deviations and measurement errors associated with the data sets. The $e_{a,b}$ are included to deal with noisy data, and can be omitted if this

is not the case, making the denominator of Eq. 4.1 simply $\sigma_a \sigma_b$. The UDCF values are calculated between every possible pair of data between the two data sets, meaning that the number of UDCF values calculated between a set of j data points and a set of k data points will be equal to $j \times k$. A value relating to correlation is thus established between values with every possible difference in time. The difference in time of two points, Δt_{ij}, is then used to create the binned DCF (the final product); in practice the difference in time may be limited within reasonable bounds. For the purposes of this investigation, the DCF equations were applied such that a positive value of Δt_{ij} corresponds to the γ-ray flux lagging behind the x-ray flux. After a binning time is chosen, the UDCF values are sorted into the bins based on the particular Δt_{ij} of each, and each bin is divided by the number of UDCF values in it (M). Then we have

$$\mathrm{DCF}(\tau) = \frac{1}{M} \mathrm{UDCF}_{ij} \tag{4.2}$$

where τ is the time binning factor.
A DCF value is thus defined for all bins which have UDCF values assigned to them, and the error of the DCF can be given by

$$\Delta\mathrm{DCF}(\tau)^2 = \sum_{i=1}^{M} \left(\mathrm{UDCF}_i - \mathrm{DCF}(\tau)\right)^2 . \tag{4.3}$$

We thus have a set of values which show the strength of correlation as a function of the difference in time between values. In a system where one observable quantity affects another observable quantity with a 'lag' in time, this property of the DCF becomes very useful. In this case, the DCF would show a correlation to exist at the characteristic time lag between the two quantities, a fact which would both prove that such a correlation existed and allow the lag to be measured. The dominant emission models for AGN, as described in Sections 1.1.4 and 1.1.5, posit that a region or regions of seed photons are responsible for the γ-ray emission via inverse-Compton upscattering. When the seed photons and the γ emission from an AGN are both observable, we would therefore expect to see a change in the seed photon population causing a change in the γ-ray photon population. Distance between the emission regions responsible for each would result in a lag between the cause and effect via causality. We would thus expect a DCF applied to light curves at the relevant wavelengths to show a correlation in the changes of the two photon populations, and to demonstrate the characteristic lag of those changes.

4.1.2 Implementation

Before any DCF results could be calculated, it was necessary to create a system capable of applying Equations 4.1 and 4.2 to two given sets of data. This system took the form of two programs; one to calculate the UDCF values, and one to bin the UDCF values into the DCF with a chosen binning. These two programs were written in the C++ programming language, and utilise features of the ROOT C++ Interpreter. They are shown in full in Appendix B.

The two programs were applied to Fermi LAT and Swift BAT data, creating results for the DCF between these two data sources. Additionally, the two programs were run using Fermi LAT and the Swift Monitoring Program data for each of the 16 relevant sources.

Modifications were made to the UDCF program in an attempt to improve the output. First, a conditional statement was applied to the UDCF calculation loop that prevented data with fluxes below zero or with errors greater than 100% from being included in the UDCF calculations. This was a simple method of attempting to remove some of the noise in the Swift BAT transient monitor data. Second, the definition of simultaneous data (that to be included in the UDCF calculations) was extended. In addition to those sections of data that were completely simultaneous between the two data sets, data within a given 'buffer' period from the completely simultaneous region was included. This meant, in practice, that whenever one data set extended past the other in time, the extra data were included up to a pre-defined limit set by the user. Given that the limits on Δt_{ij} were chosen as $\pm$1000 days, this was effectively the best choice for the length of the buffer zone, and this choice was indeed used. The effects of these modifications are discussed in Section 4.2.2.

4.2 Results

The DCF results utilising Fermi LAT and Swift XRT data are shown with 10 day binning in Figures 4.1 and 4.2. These plots show Δt_{ij} values from -1000 to 1000 days. The same data sources, but with 1 day binning and for Δt_{ij} values from -20 to 20 days, are shown in Figures 4.3 and 4.4. All of these DCF results utilise the extra constraints and additions described in Section 4.1.2.

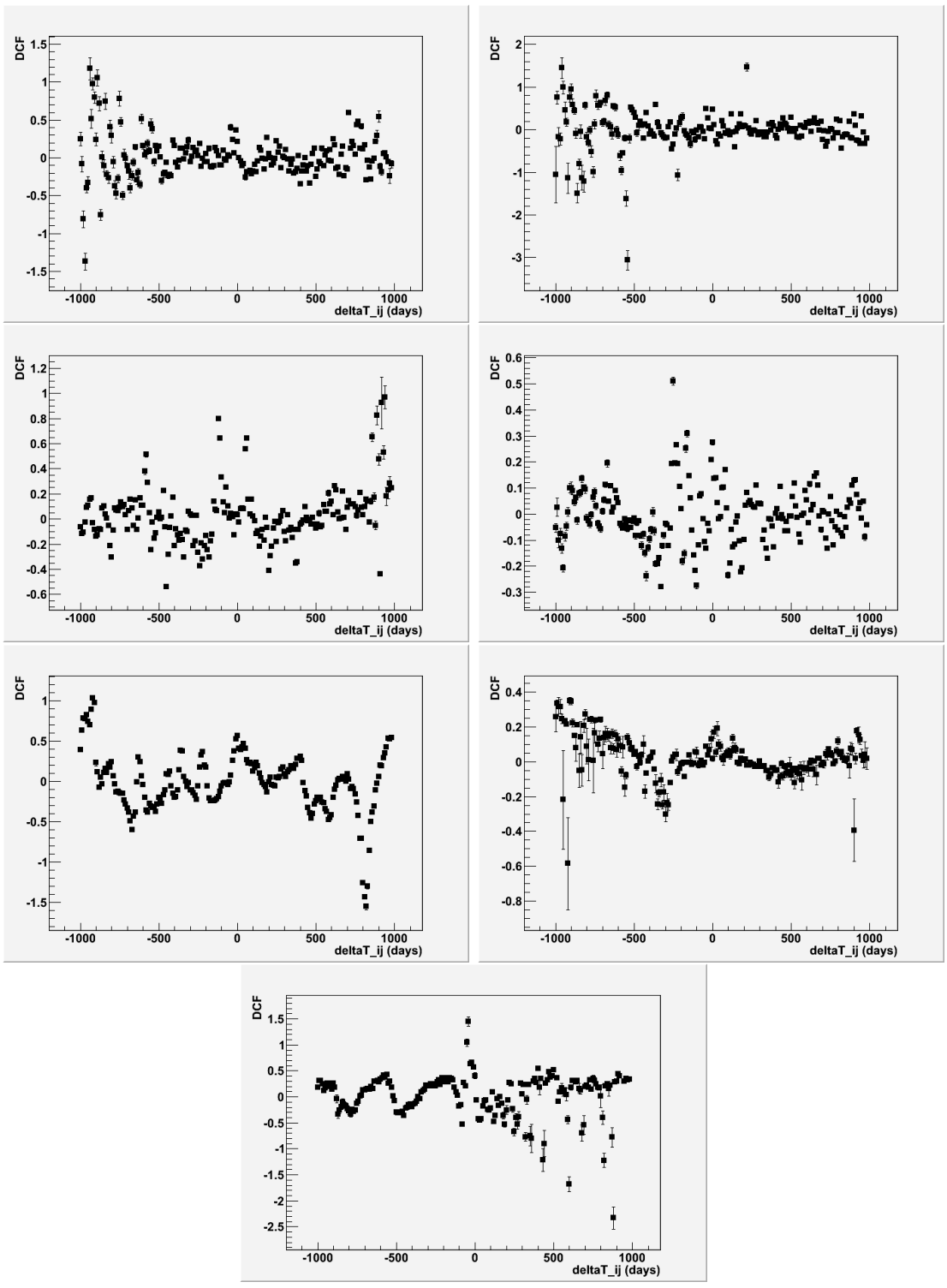

Figure 4.1 *DCF results from Fermi LAT/Swift XRT data, with 10 day binning. Δt_{ij} from -1000 to +1000 days shown, with a positive value denoting x-ray leading γ-ray. Left to right from top: 1ES 1959+650, 3C 66A, 3C 273, 3C 279, 3C 454.3, 4C 21.35, AO 0235+16.*

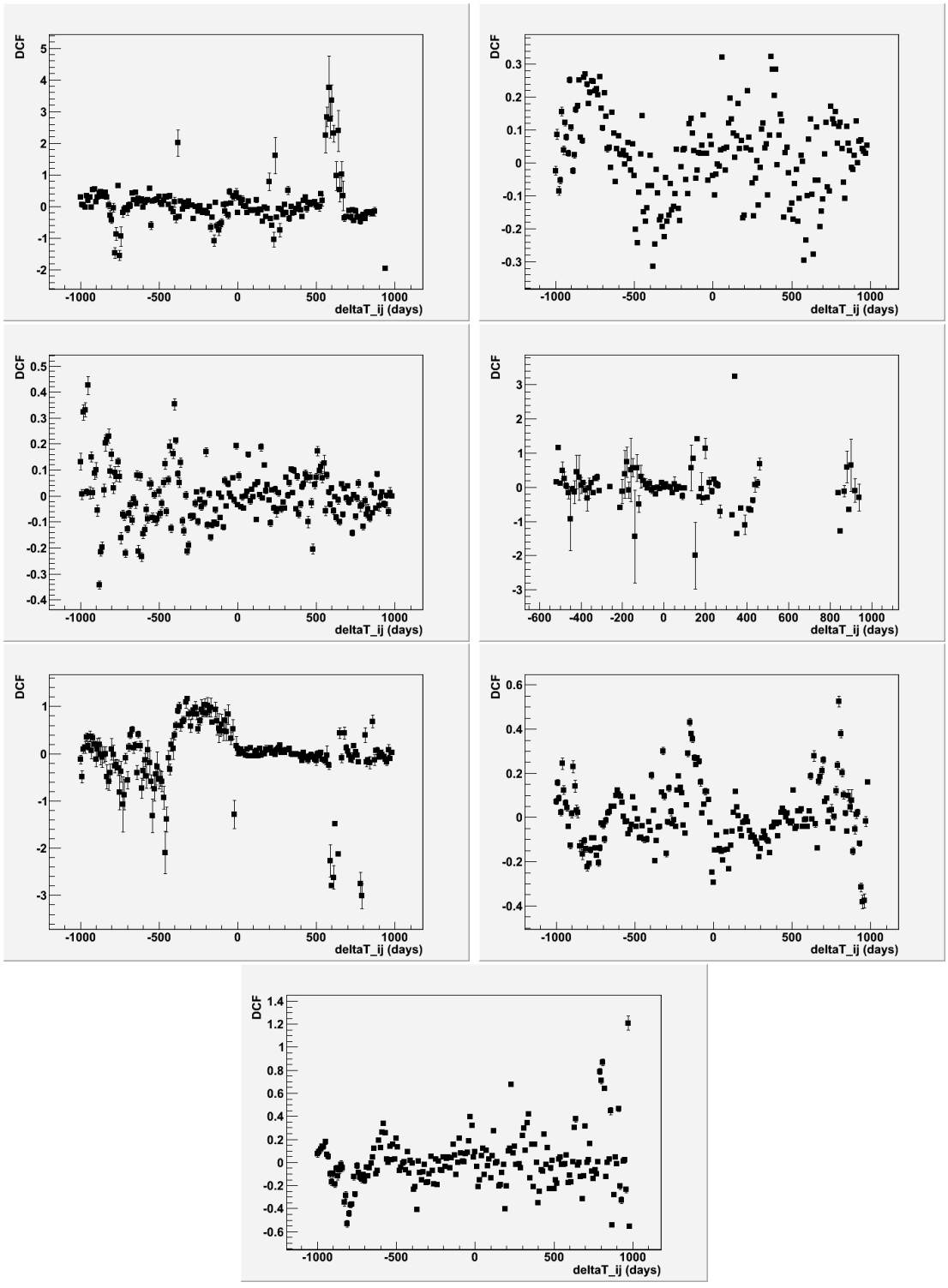

Figure 4.2 *DCF results from Fermi LAT/Swift XRT data, with 10 day binning.* Δt_{ij} *from -1000 to +1000 days shown, with a positive value denoting x-ray leading* γ*-ray. Left to right from top: H 1426+428, Mrk 421, Mrk 501, PKS 0528+134, PKS 1502+106, PKS 1510-089, PKS 2155-304.*

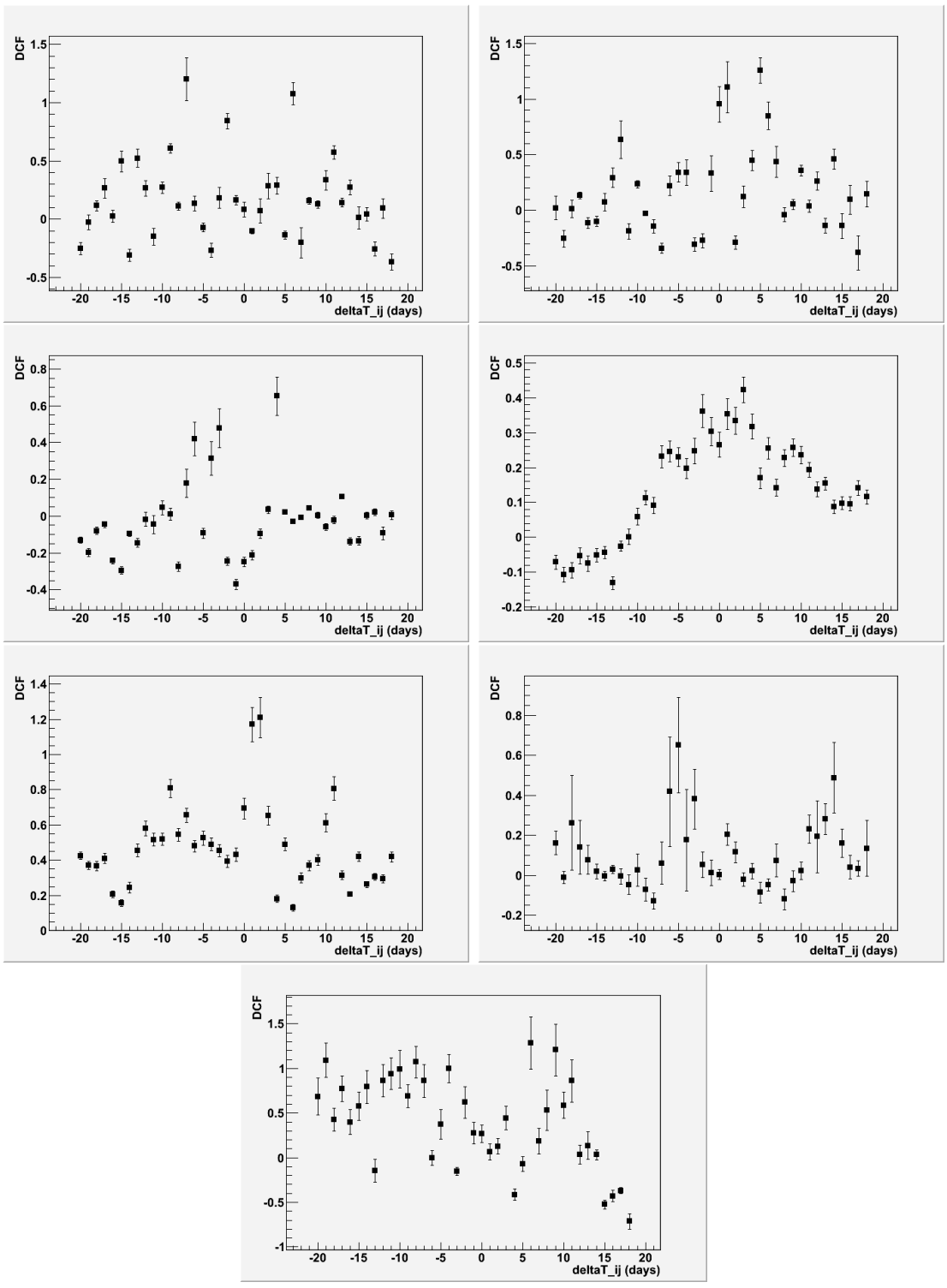

Figure 4.3 *DCF results from Fermi LAT/Swift XRT data, with 1 day binning. Δt_{ij} from -20 to +20 days shown, with a positive value denoting x-ray leading γ-ray. Left to right from top: 1ES 1959+650, 3C 66A, 3C 273, 3C 279, 3C 454.3, 4C 21.35, AO 0235+16.*

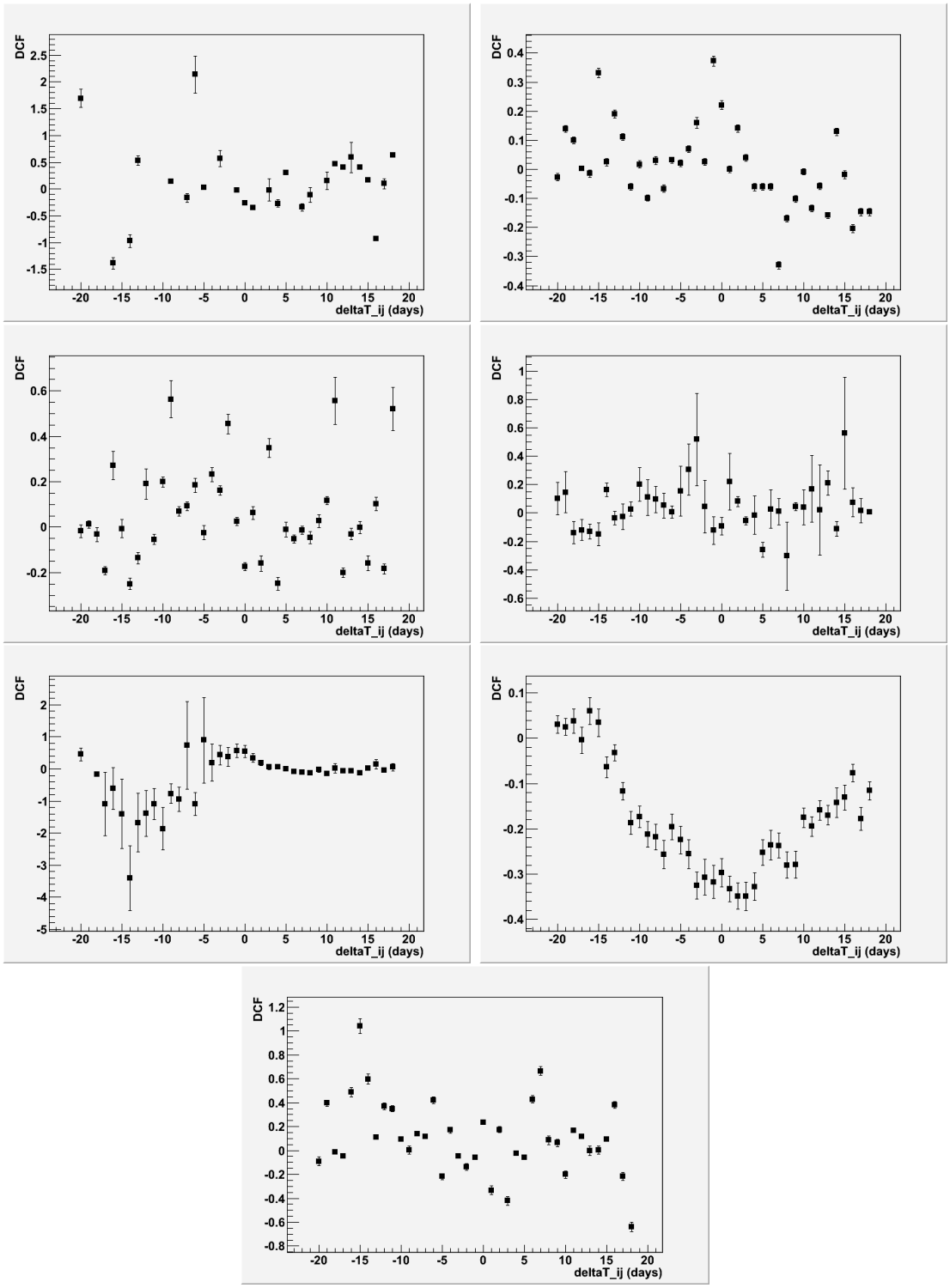

Figure 4.4 *DCF results from Fermi LAT/Swift XRT data, with 1 day binning.* Δt_{ij} *from -20 to +20 days shown, with a positive value denoting x-ray leading* γ*-ray. Left to right from top: H 1426+428, Mrk 421, Mrk 501, PKS 0528+134, PKS 1502+106, PKS 1510-089, PKS 2155-304.*

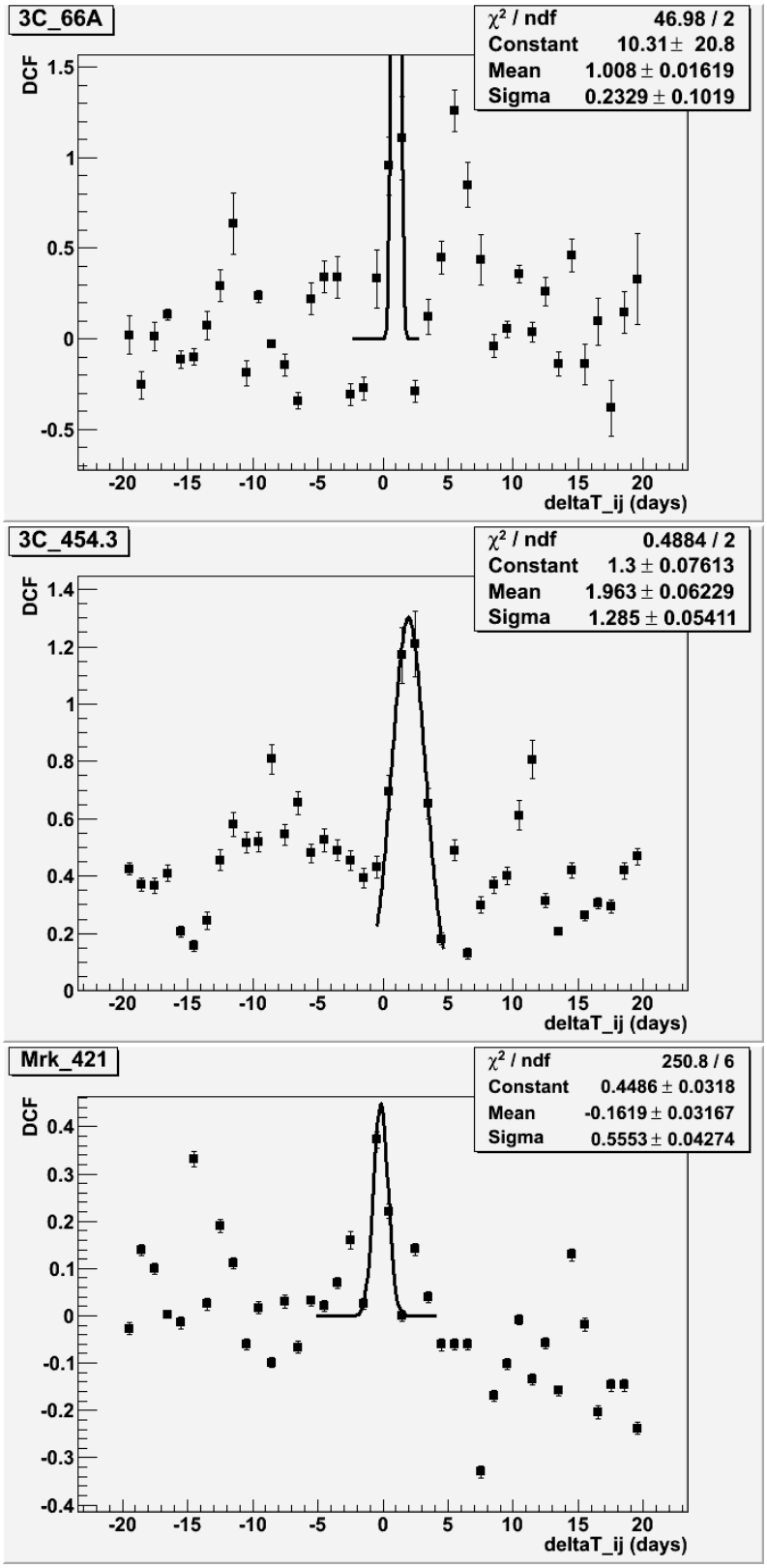

Figure 4.5 DCF results from Fermi LAT/Swift XRT data, with 1 day binning. Gaussian functions have been fitted to observed spikes in correlation around $\Delta t_{ij} = 0$ days for each source. A positive value for Δt_{ij} denotes x-ray leading γ-ray. Left to right from top: 3C 66A, 3C 454.3, Mrk 421.

4.2.1 Interpretation

The output of the binned DCF function is a plot of Δt_{ij} versus a measure of correlation. The result of this juxtaposition is the ability to see at which time scales a correlation exists, and at which direction. Individual bins, however, may be dominated by statistical coincidences, and as such a single high point on the DCF plot cannot be considered strong evidence of a correlation by itself. In addition, physical phenomena are subject to statistical variations themselves, providing further reason for a single bin to not be taken as an indication of correlation. Instead, the shape or trend of the data should be investigated, and any significant features noted. In the case of a physical phenomenon, we would expect a single point of correlation to be acted on by statistical fluctuations, and as a result to conform to a statistical distribution. The simplest such distribution is a Gaussian function, which has a peak at a certain value and spreads to both sides in a known ratio. A clear feature with a Gaussian shape arising from the trend in the data, with values in the trend being clearly higher or lower than the inherent variations in the rest of the values, is therefore an indicator of a correlation being shown in a DCF plot at the centre of the Gaussian shape. Due to the manner in which the equations defining the DCF were applied, in all cases here a positive Δt_{ij} value corresponds to x-ray flux leading γ-ray flux.

The DCFs created using Fermi and BAT data display very low correlations and much noise overall. The absence of any significantly high correlation means that even if a clear peak were identified, a meaningful conclusion could not be drawn from this fact. In practice, no clear peaks can be identified in these plots, and so the point is irrelevant.

The Fermi/XRT DCFS display much higher correlations overall than the Fermi/BAT DCFs, and as such are much more likely to contain useful information. The 10 day binned DCFs in Figures 4.1 and 4.2 show a Δt_{ij} range of -1000 to 1000 days, allowing any correlations with large time lags to be identified. A clear peak in the DCF of H 1426+428 in Figure 4.2 reaching up to a value of around 4 can be identified, while no such correlations can be readily identified in any other sources. In radio astronomy, a common phenomenon causes different wavelengths with a common cause to have a characteristic lag between them, with certain regions of matter not allowing certain wavelengths to escape. A brief postulation suggests that a similar process may be occuring here, with the γ emission being trapped behind some region which causes a delay. Alternatively, it is possible that some region of matter is reflecting the γ emission, causing a signal with a characteristic delay. If this were the case, however, it is likely that a second correlated signal would be observed: the signal causing the reflection. No evidence for a second

signal exists in this case, and so this hypothesis seems unlikely.

The 1 day binned Fermi/XRT DCFs in Figures 4.3 and 4.4 allow a higher-resolution look at the region around $\Delta t_{ij} = 0$, with the purpose of identifying quasi-simultaneous variation between x- and γ-rays. Possible peaks can be identified in the plots for 3C 66A, 3C 454.3 and Mrk 421, with the other sources not displaying any discernible features. Gaussian functions were fitted to these peaks, with the results being shown in Figure 4.5.

The fit for 3C 66A does not appear to be very good, with only two of the data points falling significantly close to the fitted function. Extending the number of points with which to fit served only to raise the quoted χ^2 value, while not appearing to significantly alter the form of the fitted function. The included plot has $\chi^2 \approx 48$. The common form of the function with the lowest χ^2 value is shown. The location of the centre of the fit indicates that there may be correlation in this source with a time lag of approximately one day, with the x-ray emission leading the γ emission.

The fit for 3C 454.3 is perhaps the most visually convincing of the three fits, and accordingly it has by far the best goodness-of-fit value (with $\chi^2 \approx 0.5$), although it only encompasses very few points overall. The fit can be seen to pass very close to six points, indicating that this form of function may describe the observed shape of the peak well. The fit describes a time lag of nearly two days, with the x-ray emission leading the γ emission.

The fit for Mrk 421 is less visually convincing than that of 3C 454.3, and it has a worse goodness-of-fit value with $\chi^2 \approx 250$. The fitted function indicates a time lag of -0.16 days, with the γ emission therefore leading the x-ray emission by this amount. The very high χ^2 value indicates that this fit may not adequately describe the data, and so the accuracy of the time lag value must be called into question. The point of highest correlation is much lower for this source than the others, possibly indicating that this peak is not an actual feature of the data but a coincidence. In Giebels et al. [21], a correlation between keV x-rays and VHE γ-rays was observed for Mrk 421. In Brown (2006) [12] and Aharonian et al. [7] a similar correlation was observed for PKS 2155-304, although this was not confirmed in this case.

4.2.2 Improvement of Data

While the number of UDCF values alone ensures a certain level of accuracy in the binned DCF outputs, there are steps which can further be taken to hone these outputs.

The Swift BAT transient monitoring observations, due to the large field of view being monitored, necessarily have less sensitivity than directed observations such as some of

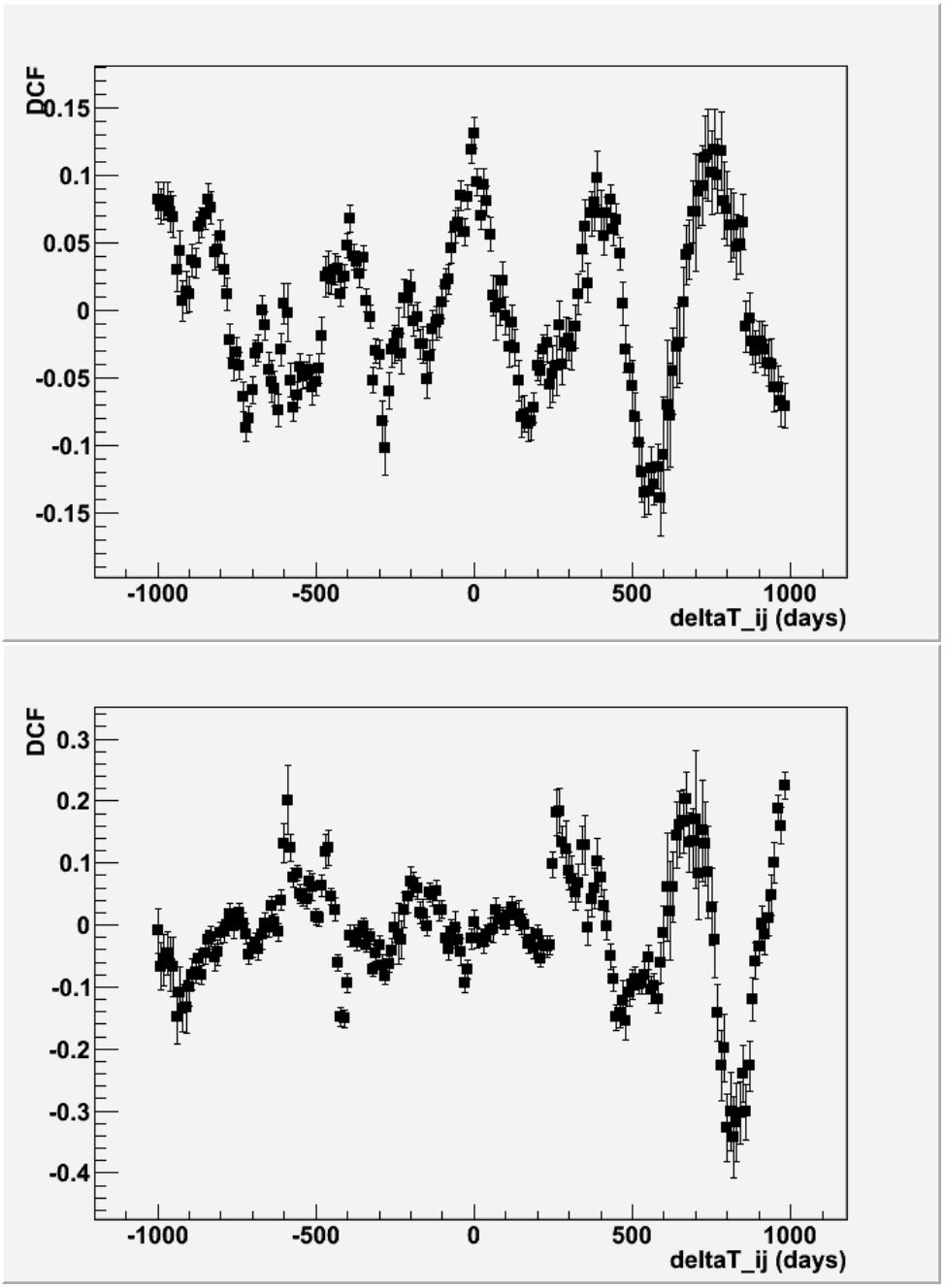

Figure 4.6 *DCF results for Fermi/BAT data from 3C 454.3 illustrating the effect of imposing restrictions on data exhibiting* $> 100\%$ *errors and negative fluxes. The top image shows the result before 'cleaning', while the bottom shows it afterwards. Note the change in scale.*

the other available BAT data. This lack of sensitivity manifests as large errors on some data, as well as some apparently negative fluxes. To increase the accuracy of the input to the DCF, certain criteria can be applied to the data that are allowed to be used, namely relating to those factors previously mentioned. A rational step is to remove those data that have greater than 100% error, since there is a chance that these values could in fact be zero, and since the error cannot be taken into account in the DCF equations in any way. Another rational step is to remove those data that are apparently below zero flux, since these points have no physical basis and do not therefore contribute any meaningful information to the DCF. As described in Section 4.1.2, these modifications were made to the DCF program. The modification appeared to primarily affect the visible lay of the data, changing the shape of certain parts of the 'trend' to become more pronounced. This effect is demonstrated in Figure 4.6.

A strength of the DCF is its flexibility in the definition of simultaneity, with data which are offset by a significant period of time still providing useful input to the process. It is therefore not necessary to use data sets which are entirely simultaneous, and to use data from one data set that may extend significantly further in time than the ends of the other data set. In initially creating the DCF program, the data sets used were truncated such that the data used in calculating the UDCF values had exactly the same time limits. Due to the flexibility of the DCF, however, this approach was ignoring usable data and reducing the total number of data used in calculating the UDCF values. A 'buffer zone' was therefore added to the coding, as described in Section 4.1.2, which allowed data outside the simultaneous range to be included. As the limits on the DCF bins were set to $\Delta t_{ij} = \pm 1000$ days, a 1000 day buffer zone was established. The results of this extra inclusion of data are shown in Figure 4.7. The most apparent result is the reduction in magnitude of those bins which fall significantly away from the trend, reducing the overall noise of the result. The magnitude of parts of the trend were also lowered, showing that the apparent 'trend' in these parts of the plot is likely an irrelevant fluctuation and not indicative of any real correlation.

After all the above improvements were made to the DCFs created from Fermi and BAT data, DCFs were created using the XRT data that still utilised these measures.

4.3 Emission Models

In Section 4.2.1, Gaussian fits to the sources 3C 66A, 3C 454.3 and Mrk 421 were discussed. These fits showed a numerical interpretation of the correlation between XRT and

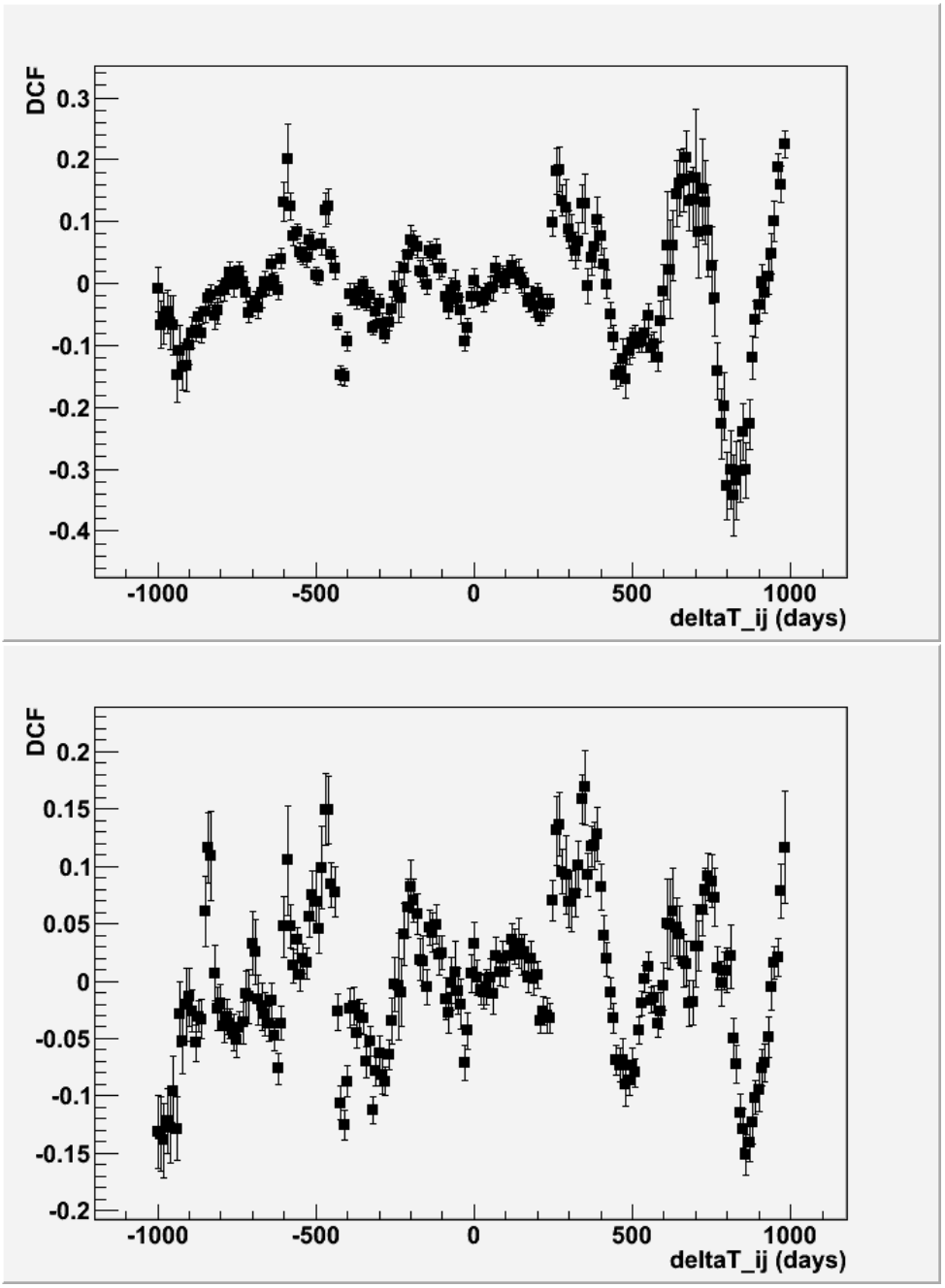

Figure 4.7 *DCF results for Fermi/BAT data from 3C 454.3 illustrating the effect of applying a 1000 day buffer to the included data. The top image shows the result before the buffer was applied, while the bottom shows it afterwards. Note that the vertical scales differ by a factor of two.*

Fermi data.

The fit for 3C 66A in Figure 4.5 showed a possible correlation with a time lag of approximately one day, which if indeed present would indicate that an SSC component plays a role in the γ-ray emission of this source. Abdo et al. (2011) found, through a multiwavelength campaign on 3C 66A, that the observed characteristics of the source could be described by either a pure SSC emission model or an SSC emission model with additional EC components [3].

A correlation seems to be strongly visually apparent for 3C 454.3, with a clear and well-fitted peak centred around a time lag of approximately two days. This implies that there is likely a strong SSC component to the sources emission. Finke and Dermer, however, found in their investigation that a simple SSC model does not describe the object's behaviour [17]. Instead, they posit that EC components must be present.

Mrk 421 has a possible peak present, with a fitted Gaussian being centred around a time lag of -0.16 days. If a correlation of an SSC type existed, we would expect a positive time lag, indicating that the γ emission followed the x-ray emission. Ghisellini, Maraschi and Dondi found that a simple SSC model best describes the emission from Mrk 421 [20], which suggests that the fit in this case is within the margin of error of the data.

While PKS 2155-304 did not display sufficient structure to identify a correlation between the two energy ranges, Aharonian et al. and Brown (2006) found a correlation in their studies (as mentioned in Section 4.2.1). Brown (2006) found that an SSC model described the emission of the object well. As the time ranges utilised in that study and this thesis differ by several years, it is possible that PKS 2155-304 has changed from an SSC mechanism to some other mechanism in that time. This supports the hypothesis in Section 2.5 that the inner workings of the jet may change with time.

Chapter 5

Conclusion

Daily-binned Fermi LAT data were used to calculate e-folding times for the 19 selected sources. The smallest e-folding timescales, both rise and decay, range from 0.4 - 21 days, with most sources having smallest e-folding times of between 0.4 and 0.6 days. These timescales, when corrected for the redshift of each source, gave rise to limits on the size of the γ-ray emission region ranging from $R\delta^{-1} = 4.39 \times 10^{12}$ to $R\delta^{-1} = 5.14 \times 10^{14}$ m. Due to the binning size used, these are not extreme limits, but they can be considered highly rigorous. The selection process applied to the outputs of the likelihood fitting for each source meant that the faintest sources had fewer surviving data, meaning that these results are more accurate for the brightest sources.

Flux duty cycles were plotted at γ wavelengths for 14 sources using Fermi data. Of these sources, 3C 66A, 3C 273, 3C 454.3, 4C 21.35, PKS 1502+106 and PKS 1510-089 display clear structure at fluxes above the statistical distribution, indicating flaring activity during the observational period. For all sources but 3C 66A, the Fermi light curves confirm that flaring activity was indeed present.

Plots of the flux against the spectral index Γ were also created using Fermi data, for all 19 sources. 11 of these 19 sources displayed structure at high fluxes, and had linear fits applied to this structure. Of those 11, 8 were found to exhibit harder-when-brighter behaviour: 3C 66A, 3C 273, 3C 454.3, 4C 21.35, 4C 71.07, Mrk 421, PKS 1502+106 and PKS 1510-089. The sources 3C 273, 3C 454.3, 4C 21.35 and PKS 1510-089 have been found to display harder-when-brighter behaviour in other investigations, confirming the results in those cases. Two sources which were not found to display harder-when-brighter behaviour, AO 0235+16 and PKS 2155-304, have been previously reported to display such behaviour, however. This HWB behaviour indicates an acceleration and cooling scenario occurring in these sources, most likely due to changes in the accretion rate of the system.

e-folding timescales were also calculated using Swift XRT data for those sources with available data, 16 of the 19 sources. Due to the small time between data points, however, these timescales conflict greatly with generally accepted limits (4 - 600 s as compared to $\sim$ 2000 s). A certain effect that applies only to very short-timescale data is considered to be responsible for this disagreement. As a result, size limits for the x-ray emission region were not calculated.

The Discrete Correlation Function was used to probe the correlation of x- and γ-ray fluxes, in this case Swift XRT and Fermi LAT data. DCFs with 10 day binning and a range of $\pm$1000 days were created to look for long-timescale correlation in each source. A clear peak of correlation was discovered in the DCF of H 1426+428, at a time lag of approximately 600 days, although it is currently unclear what physical processes (if any) are responsible for this apparent correlation. DCFs with 1 day binning and a range of $\pm$20 days were also created, to look for quasi-simultaneous correlation between x- and γ-rays. Sources 3C 66A, 3C 454.3 and Mrk 421 displayed possible peaks of correlation near zero time lag, and Gaussian functions were fitted to each. 3C 66A displayed a peak around a time lag of approximately one day, with x-rays leading γ, consistent with the effect of the SSC emission model. A previous multiwavelength investigation of this source has indicated that an SSC or SSC + EC model fit its emission, in agreement with the observations here. 3C 454.3 displayed a clear peak at a time lag of approximately two days, again with x-rays leading γ and thus consistent with the effect of the SSC model. Previous studies indicate, however, that a pure SSC model does not fit the source's emission as well as an SSC + EC model. Mrk 421 displayed a peak with an apparent time lag of -0.16 days, indicating a possibility that the γ flux leads the x-ray flux. More likely, however, is that the fit is either an artifact of the data or that the position of the centre of the peak is uncertain. A previous study indicates that a simple SSC model with no EC component best describes this source.

In addition to all the above results, a number of points remain open to further investigation. Unfortunately, time constraints meant that these points were not able to be explored before submission of this thesis. The XRT data warrant an in-depth study to determine the exact nature of these observations, and contact with the providers of these data may reveal currently unknown aspects of the format and origin of the provided files. The spike of correlation in H 1426+428 at $\Delta t_{ij} = 600$ days is a compelling result, with two postulated theories but not enough evidence to suggest that either of them fit the observation. Further investigation into this phenomenon is therefore required. The lack of a HWB trend in AO 0235+16 and PKS 2155-304, where such a trend has been previously reported, may suggest that the mechanism responsible for γ-ray emission in these sources

has changed with time. Similarly, the previously reported SSC emission in PKS 2155-304, where none was found here, may indicate a change in the mechanism. This clearly warrants further study, with the currently accepted position (that a single emission model should describe a source in any time range) being challenged.

Bibliography

[1] SIMBAD Astronomical Database, 2013. URL `http://simbad.u-strasbg.fr/simbad/`.

[2] Abdo, A.A. et al. Fermi large area telescope and multi-wavelength observations of the flaring activity of PKS 1510-089 between 2008 September and 2009 June. *Astrophys. J.*, 721:1425–1447, 2010.

[3] Abdo, A.A. et al. Multi-wavelength observations of the flaring gamma-ray blazar 3C 66A in 2008 October. *Astrophys. J.*, 726(1):43, 2011.

[4] Abdo, A.A. et al. Spectral properties of bright Fermi-detected blazars in the gamma-ray band. *Astrophys. J.*, 710:1271–1285, 2010.

[5] Ackermann, M. et al. Fermi Gamma-ray Space Telescope observations of gamma-ray outbursts from 3C 454.3 in 2009 December and 2010 April. *Astrophys. J.*, 721: 1383–1396, 2010.

[6] Ackermann, M. et al. The Second Catalog of Active Galactic Nuclei Detected by the Fermi Large Area Telescope. *Astrophys. J.*, 743(2), 2011.

[7] Aharonian, F. et al. Multi-wavelength observations of PKS 2155-304 with HESS. *Astron.and Astrophys.*, 442(3):895–907, 2005.

[8] Atwood, W.B. et al. The Large Area Telescope on the Fermi Gamma-ray Space Telescope mission. *Astrophys. J.*, 697(2):1071, 2009.

[9] Barthelmy, S.D. et al. The Burst Alert Telescope (BAT) on the SWIFT Midex Mission. *Space Science Reviews*, 120(3-4):143–164, 2005.

[10] Blandford, R.D. and Znajek, R.L. Electromagnetic extraction of energy from Kerr black holes. *MNRAS*, 179:433–456, 1977.

[11] Brown, A.M. Locating the gamma-ray emission region of the flat spectrum radio quasar PKS 1510-089. *arXiv preprint arXiv:1301.7677*, 2013.

[12] Brown, A.M. *Very High Energy Emission and Multi-wavelength Campaigns of the BL Lac Object PKS 2155-304*. PhD thesis, University of Durham, 2006.

[13] Brown, A.M. and Adams, J. High energy γ-ray properties of the FR I radio galaxy NGC 1275. *MNRAS*, 413(4):2785–2790, 2011.

[14] Brown, A.M. and Adams, J. Discovery of γ-ray emission from the broad-line radio galaxy Pictor A. *MNRAS*, 421(3):2303–2309, 2012.

[15] Corbet, R. like_lc.pl, 2012. URL `http://fermi.gsfc.nasa.gov/ssc/data/analysis/user/like_lc.pl`.

[16] Edelson, R.A. and Krolik, J.H. The Discrete Correlation Function: A new method for analyzing unevenly sampled variability data. *Astrophys. J.*, 333:646–659, 1988.

[17] Finke, J.D. and Dermer, C.D. On the Break in the Fermi-Large Area Telescope Spectrum of 3C 454.3. *Astrophys. J. Lett.*, 714(2):L303, 2010.

[18] Foschini, L et al. A short hard X-ray flare from the blazar NRAO 530 observed by INTEGRAL. *Astron. Astrophys.*, 450(1):77–81, 2006.

[19] Foschini, L. et al. Search for the shortest variability at gamma rays in flat-spectrum radio quasars. *Astron. Astrophys.*, 530(77), 2011.

[20] Ghisellini, G, Maraschi, L, and Dondi, L. Diagnostics of Inverse-Compton models for the gamma-ray emission of 3C 279 and MKN 421. *Astron. Astrophys. Supplement Series*, 120:503, 1996.

[21] Giebels, B., Dubus, G., and Kh'lifi, B. Unveiling the X-ray/TeV engine in Mkn 421. *Astron. Astrophys.*, 462(1):29–41, 2007.

[22] Hofmann, W. HESS - an Array of Imaging Atmospheric Cherenkov Telescopes for Stereoscopic Observations of Air Showers in the 100 GeV Energy Range. *Proc. of the Workshop "Towards a major atmospheric Cherenkov detector - V"*, page 405, 1997.

[23] Kadota, A. et al. An Intrinsic Short-Term Radio Variability Observed in PKS 1510-089. *Publications of the Astronomical Society of Japan*, 64:109, 2012.

[24] Kirk, J.G., Rieger, F.M., and Mastichiadis, A. Particle acceleration and synchrotron emission in blazar jets. *arXiv preprint astro-ph/9801265*, 1998.

[25] Papadakis, I. E. and Lawrence, A. Improved Methods for Power Spectrum Modelling of Red Noise. *MNRAS*, 261(3):612, 1993.

[26] Saito, S. et al. Very Rapid High-amplitude Gamma-Ray Variability in Luminous Blazar PKS 1510–089 Studied with Fermi-LAT. *Astrophys J. Lett.*, 766(1):L11, 2013.

[27] Sazonov, S. Yu. and Revnivtsev, M. G. Statistical properties of local active galactic nuclei inferred from the RXTE 3-20 keV all-sky survey. *Astron. Astrophys.*, 423: 469–480, 2004.

[28] Soldi, S., Beckmann, V., and Turler, M. The variability of the quasar 3C 273: a radio to gamma-ray view. *arXiv preprint*, arXiv:0912.2266, 2009.

[29] Stroh, M. and Falcone, A. Swift X-ray Telescope Monitoring of Fermi-LAT Gamma Ray Sources of Interest. *Astrophys. Journ. Suppl.*, submitted, 2013. URL `http://www.swift.psu.edu/monitoring/`.

[30] Tanaka, Y.T. et al. Fermi Large Area Telescope detection of bright γ-ray outbursts from the peculiar quasar 4C +21.35. *Astrophys. J.*, 733:19, 2011.

[31] Tavecchio, F. et al. Constraining the location of the emitting region in Fermi blazars through rapid gamma-ray variability. *MNRAS*, 405(94), 2010.

[32] Urry, C.M. and Padovani, P. Unified Schemes for Radio-Loud Active Galactic Nuclei. *PASP*, 107:803–845, 1995.

[33] Woo, Jong-Hak and Urry, C.M. Active galactic nucleus black hole masses and bolometric luminosities. *Astrophys. J.*, 579:530–544, 2002.

Appendices

Appendix A

e-folding Program

The following is the γ-ray version of the e-folding calculation program.

```
#include <iostream>
#include <fstream>
#include <math.h>
#include <stdlib.h>
using namespace std;

int main ()
{

//      User inputs
//-------------------------------------------------------------------
        const int arraySize = 2000;             //Size for data arrays
//-------------------------------------------------------------------

string inputfile, outputfile, dummy;
int nl, i;
double time[arraySize], flux[arraySize], delFlux[arraySize], delTime[arraySize], TS[arraySize], gamma[
    arraySize], delGamma[arraySize];
double tau[arraySize], delTau[arraySize], minRiseTau, delMinRiseTau, minFallTau, delMinFallTau;
int minRiseIndex, minFallIndex;

ifstream input;
ofstream results;

cout << endl << "Enter input filename: ";
cin >> inputfile;

input.open(inputfile.c_str(), ios::in);

if (! input.is_open())  //Checking file works.
        {
        cout << "Error while opening input file " << inputfile.c_str() << "." << endl;
        exit (EXIT_FAILURE);
        }

cout << "Enter output filename: ";
cin >> outputfile;

nl = 0;
i = 0;

minRiseTau = 100000;    //Setting large initial values for minimum e-folding times.
minFallTau = -100000;

while (!input.eof())    //Reading in data and getting number of lines.
        {
        input >> time[i] >> flux[i] >> delFlux[i] >> delTime[i] >> TS[i] >> gamma[i] >> delGamma[i];
```

```
        //cout << time[i] << " " << flux[i] << " " << delFlux[i] << " " << delTime[i] << endl;
        if (i >= 1)
                {
                tau[i] = (time[i] - time[i-1]) / (log(flux[i]/flux[i-1]));       //Tau and error.
                delTau[i] = tau[i] * sqrt( pow(delFlux[i]/flux[i],2) + pow(delTime[i]/time[i],2) );

                if(delTau[i] < 0)
                        {
                        delTau[i] = -delTau[i];
                        }
                if(tau[i] > 0 && tau[i] < minRiseTau)
                        {
                        minRiseTau = tau[i];
                        delMinRiseTau = delTau[i];
                        minRiseIndex = i;
                        }
                if(tau[i] < 0 && tau[i] > minFallTau)
                        {
                        minFallTau = tau[i];
                        delMinFallTau = delTau[i];
                        minFallIndex = i;
                        }
                //cout << tau[i] << " +/- " << delTau[i] << endl;
                }
        i++;
        getline (input,dummy);  //Next line.
        }

input.close();

nl = i - 1;

cout << "Minimum rise time: " << minRiseTau << " +/- " << delMinRiseTau << " at " << time[minRiseIndex]
     << endl;
cout << "Minimum decay time: " << minFallTau << " +/- " << delMinFallTau << " at " << time[minFallIndex
    ] << endl;

results.open(outputfile.c_str(), ios::out);      //Output results to specified file.
for (i=0; i < nl; i++)
        {
        results << time[i] << " " << flux[i] << " " << delFlux[i] << " " << delTime[i] << " " << TS[i]
            << " " << gamma[i] << " " << delGamma[i] << " " << tau[i] << " " << delTau[i] << endl;
        }
results.close();

ofstream log;
log.open("e-folding_results.txt", ios::out | ios::app); //Add to e-folding log file.
log << inputfile << " Rise: " << minRiseTau << " +/- " << delMinRiseTau << " at " << time[minRiseIndex]
     << " MJD, Fall: " << minFallTau << " +/- " << delMinFallTau << " at " << time[minFallIndex] << "
    MJD." << endl;
log.close();

return 0;
}
```

Appendix B

DCF Programs

UDCF Calculator (Fermi/XRT Version)

```
#include <iostream.h>
#include <fstream>
#include <math.h>

//Output codes: 0 = success, 1 = , 2 = file open failure, 3 = file format problem/empty file

int DCF_finder_XRT()
{
gROOT->Reset();

//      Important information:
//
    ------------------------------------------------------------------------------------------------------------

//      Throughout this file, Fermi data shall be known as "1" and XRT as "2".
//      Output codes: 0 = success, 1 = unused, 2 = file open failure, 3 = file format problem/empty
    file
//
    ------------------------------------------------------------------------------------------------------------


//      User-set inputs:
//------------------------------------------------------------------------------------------------------------
        //int binSize = 50;                                     //DCF bin size in days
        const int arraySize = 30000;                          //Size of arrays to use to store data
        double bufferSize = 1;                                //Maximum size of buffer time in data
//------------------------------------------------------------------------------------------------------------

cout << endl;
cout << "  ------------------------" << endl;
cout << "    Fane's UDCF Finder  " << endl;
cout << "  ------------------------" << endl << endl;

//---------------------------------
string fermifolder = "fermi/";
string XRTfolder = "";
string fermiapp = "_daily.txt";
string XRTapp = "lightcurve3.txt";
string outBefore = "UDCF_";
string outAfter = "_XRT_fine.dat";
//---------------------------------

string id;
string inputfile1_detect;
string inputfile2_detect;
string UDCF_output;
```

```
string fermi;
string xrt;

cout << "Source id: ";
cin >> id;

/*cout << "Fermi like_lc.pl file: ";
cin >> fermi;
cout << "XRT file: ";
cin >> xrt;
cout << "UDCF output file: ";
cin >> UDCF_output;
cout << endl;*/

/*inputfile1_detect.append(fermi);      //Adding filenames to folder strings to get proper filenames.
inputfile2_detect.append(xrt);*/

inputfile1_detect = fermifolder + id + fermiapp;
inputfile2_detect = XRTfolder + id + XRTapp;
UDCF_output = outBefore + id + outAfter;


//Fermi data arrays:
double time1[arraySize], flux1[arraySize], delflux1[arraySize], deltime1[arraySize], TS1[arraySize],
     spec1[arraySize], delspec1[arraySize];

//XRT data arrays:
double time2[arraySize], binHW2[arraySize], flux2[arraySize],  delflux2[arraySize], exp2[arraySize],
     mode2[arraySize];

string dummy;   //Dummy for getline().
int i, j, k, numlines1, numlines2;      //Integers to do with number of rows in each file, loop
     integers.

double MJDmin, MJDmax, MJD1min, MJD2min, MJD1max, MJD2max;      //Start and end times of simultaneous
     data.
int startIndex1, endIndex1, startIndex2, endIndex2, length1, length2;   //Indices of orginal data
     arrays corresponding to limits of simultaneous data.

double sum1, sum2, avg1, avg2, SDsum1, SDsum2, SD1, SD2;        //Variables for flux averages and
     standard deviations.

double maxDelT, minDelT;        //Largest and smallest UDCF values, for binning.
//float numNegBins, numPosBins;
//int binToUse;

//FILE *UDCFoutput;

//-----------------------
//  Fermi input section
//-----------------------

  //input section from Anthony
  cout << "Looking for file " << inputfile1_detect.c_str() << ": ";
  ifstream inp_detect;
  inp_detect.open(inputfile1_detect.c_str(), ios::in);
  if (! inp_detect.is_open()) {
    cout << "Error while opening input file " << inputfile1_detect.c_str() << endl;
    exit(2);
  }
  cout << "File opened."<< endl;

//reading FERMI data
while (!inp_detect.eof())
        {
        inp_detect >> time1[i] >> flux1[i] >> delflux1[i] >> deltime1[i] >> TS1[i] >> spec1[i] >>
             delspec1[i];
        i=i+1;
        getline (inp_detect,dummy);
        }

numlines1 = i - 1;      //Save number of lines read.
```

```
inp_detect.close();      //Close Fermi data file

if (numlines1 < 1)
        {
        cout << "No lines in Fermi file!" << endl;
        exit(3);
        }
else
        {
        cout << numlines1 << " lines read from file , from " << time1[0] << " to " << time1[numlines1-1]
             << " MJD." << endl << endl;
        }

i=0;     //Reset line counter.

//----------------------
//  XRT input section
//----------------------

  //Input section from Anthony
  cout << "Looking for file " << inputfile2_detect.c_str() << ": ";
  ifstream inp_detect;
  inp_detect.open(inputfile2_detect.c_str(), ios::in);
  if (! inp_detect.is_open()) {
    cout << "Error while opening input file " << inputfile2_detect.c_str() << endl;
    exit(2);
  }
  cout << "File opened."<< endl;

//reading XRT data
while (!inp_detect.eof())
        {
        inp_detect >> time2[i] >> binHW2[i] >> flux2[i] >>  delflux2[i] >> exp2[i] >> mode2[i];
        if (flux2[i] > 0 && delflux2[i] < flux2[i])      //Remove data below zero and data whose error
             is more than 100%
                {i=i+1;}
        getline (inp_detect,dummy);
        }

numlines2 = i - 1;       //Save number of lines read.

inp_detect.close();      //Close XRT data file.

if (numlines2 < 1)
        {
        cout << "No lines in XRT file!" << endl;
        exit(3);
        }
else
        {
        cout << numlines2 << " lines read from file , from " << time2[0] << " to " << time2[numlines2-1]
             << " MJD." << endl << endl;
        }

//-----------------------
//  Truncation of data
//-----------------------

if (time1[0] < time2[0])         //Minimum simultaneous time is the larger of the two start values.
        {
        MJDmin = time2[0];
        startIndex2 = 0;
        if (time2[0] - time1[0] > bufferSize)   //If 1 starts more than (bufferSize) days before 2,
             start using it at (bufferSize) days before, otherwise start 1 when it normally would.
                {
                for (j=0; floor(time1[j]) <= floor(time2[0])-bufferSize; j++)
                        {
                        startIndex1 = j;
                        }
                }
        else
                {
                startIndex1 = 0;
                }
```

```
        }
else
        {
        MJDmin = time1[0];
        startIndex1 = 0;
        if (time1[0] - time2[0] > bufferSize)
                {
                for (j=0; floor(time2[j]) <= floor(time1[0]-bufferSize); j++)
                        {
                        startIndex2 = j;
                        }
                }
        else
                {
                startIndex2 = 0;
                }
        }

if (time1[numlines1-1] < time2[numlines2-1])     //Maximum simultaneous time is the smaller of the two
    end values.
        {
        MJDmax = time1[numlines1-1];
        endIndex1 = numlines1-1;
        if (time2[numlines2-1] - time1[numlines1-1] > bufferSize)
                {
                for (j=numlines2-1; floor(time2[j]) >= floor(time1[numlines1-1])+bufferSize; j--)
                        {
                        endIndex2 = j;
                        }
                }
        else
                {
                endIndex2 = numlines2-1;
                }
        }
else
        {
        MJDmax = time2[numlines2-1];
        endIndex2 = numlines2-1;
        if (time1[numlines1-1] - time2[numlines2-1] > bufferSize)
                {
                for (j=numlines1-1; floor(time1[j]) >= floor(time2[numlines2-1])+bufferSize; j--)
                        {
                        endIndex1 = j;
                        }
                }
        else
                {
                endIndex1 = numlines1-1;
                }
        }

length1 = (endIndex1+1)-startIndex1;     //Extra '1' is for fencepost error.
length2 = (endIndex2+1)-startIndex2;

cout << "Simultaneous time region is from " << MJDmin << " to " << MJDmax << " MJD." << endl;
cout << "Useful Fermi data: " << time1[startIndex1] << " to " << time1[endIndex1] << " MJD, indices "
    << startIndex1 << " - " << endIndex1 << " (" << length1 << " points)." << endl;
cout << "Useful BAT data: " << time2[startIndex2] << " to " << time2[endIndex2] << " MJD, indices " <<
    startIndex2 << " - " << endIndex2 << " (" << length2 << " points)." << endl << endl;

//---------------------
//  UDCF calculation
//---------------------

for (j=startIndex1; j <= endIndex1; j++)        //Calculation of average for selected Fermi data.
        {
        sum1 = sum1 + flux1[j];
        }
avg1 = sum1/length1;

for (j=startIndex1; j <= endIndex1; j++)        //Calculation of standard deviation for selected Fermi
    data. Needs avg1.
        {
```

```
        SDsum1 = SDsum1 + pow( (flux1[j]-avg1), 2 );
        }
SD1 = sqrt( SDsum1/length1 );

for (j=startIndex2; j <= endIndex2; j++)        //Calculation of average for selected XRT data.
        {
        sum2 = sum2 + flux2[j];
        }
avg2 = sum2/length2;

for (j=startIndex2; j <= endIndex2; j++)        //Calculation of standard deviation for selected XRT
    data. Needs avg2.
        {
        SDsum2 = SDsum2 + pow( (flux2[j]-avg2), 2 );
        }
SD2 = sqrt( SDsum2/length2 );

cout << "Fermi avg: " << avg1 << ", SD: " << SD1 << endl;
cout << "XRT avg: " << avg2 << ", SD: " << SD2 << endl << endl;

const int UDCFlength = length1*length2; //Would be minus one, but for some reason it has a hissy fit.
double UDCF[UDCFlength], delT[UDCFlength];      //Define data arrays the right size to house the UDCFs.

maxDelT = 0;
minDelT = 0;

k = 0;  //Counter for UDCF array indices.

/*ofstream NaNlog;      //File output for logging those pesky NaNs.
NaNlog.open("NaNlog.txt", ios::out);*/

ofstream UDCF_out;
UDCF_out.open(UDCF_output.c_str(), ios::out);

for (i=startIndex1; i <= endIndex1; i++)        //Nested 'for' loops to calculate UDCFs. 'i' is index
    for set 1, 'j' for set 2.
        {
        for (j=startIndex2; j <= endIndex2; j++)
                {
                //UDCF[k] = ( (flux1[i]-avg1)*(flux2[j]-avg2) ) / sqrt( ( pow(SD1,2)-pow(delflux1[i],2)
                      ) * ( pow(SD2,2)-pow(delflux2[j],2) ) );        //WITH e_a, e_b.
                UDCF[k] = ( (flux1[i]-avg1)*(flux2[j]-avg2) ) / sqrt(pow(SD1,2)*pow(SD2,2));    //
                    WITHOUT e_a, e_b.
                delT[k] = time1[i] - time2[j];  //Defining time lag, deltaT_ij for each UDCF value.

                if (delT[k] > maxDelT)  //Max and min UDCF are needed for the binning.
                        maxDelT = delT[k];
                else if (delT[k] < minDelT)
                        minDelT = delT[k];

                if (UDCF[k] != UDCF[k]) //NaN != NaN, so this is a check.
                        {
                        //NaNlog << "((" << flux1[i] << "-" << avg1 << ")*(" << flux2[j] << "-" << avg2
                              << ")) / sqrt((" << SD1 << "^2-" << delflux1[i] << "^2) * (" << SD2 <<
                             "^2-" << delflux2[j] << "^2)) = " << UDCF[k] << endl;
                        }


                UDCF_out << delT[k] << " " << UDCF[k] << endl;

                k++;
                }
        }

UDCF_out.close();       //Close UDCF filestream.

cout << "Wrote " << UDCFlength << " lines to file \"" << UDCF_output << "\"." << endl << endl;

//NaNlog.close();

return 0;

}
```

DCF Binner

```
#include <iostream>
#include <fstream>
#include <math.h>

//Output codes: 0 = success, 1 = , 2 = file open failure, 3 = file format problem/empty file

int UDCF_DCF_XRT()
{

/*
//      User-set inputs:
//-------------------------------------------------------------------------------------------------------
        string inputfile = "1959_UDCF.txt";             //Input UDCF file
        string outputfile = "1959_DCF_50d.txt";         //Output DCF file
        double binSize = 50;                            //Bin size in days to use
//-------------------------------------------------------------------------------------------------------
*/

cout << endl;
cout << "  ----------------------" << endl;
cout << "    Fane's DCF Binner  " << endl;
cout << "  ----------------------" << endl << endl;

string inBefore = "UDCF_";      //Strings to use with common filenames.
string inAfter = "_XRT_fine.dat";
string outBefore = "DCF_";
string outMid = "d_";
string outAfter = "_XRT_fine.dat";


string id;
string inputfile;
string outputfile;
string binDays = "10";
double binSize;
double Tlim = 1000;

//----------------------
//  Getting user inputs
//----------------------

cout << "Source ID: ";
cin >> id;
/*cout << "UDCF filename: ";
cin >> inputfile;
cout << "Output filename: ";
cin >> outputfile;*/
cout << "Bin size (days): ";
cin >> binSize;
cout << "Repeat for string: ";
cin >> binDays;
cout << "Delta T limit (days): ";
cin >> Tlim;
cout << endl;

inputfile = inBefore + id + inAfter;
outputfile = outBefore + binDays + outMid + id + outAfter;

int i, j;
string dummy;

double maxDelT, minDelT;        //Extremes of delta T, error of delta T.
float numNegBins, numPosBins;
int binToUse;

double DCFtotalPrev, DCFbinFillPrev;    //For error checking.

ifstream inp_detect;    //Setting up input filestream.

ofstream DCF_file;      //Setting up output filestream.

ofstream error_file;
```

```
//-------------------------
//  Getting number of lines
//-------------------------

i = 0;
cout << "Looking for file " << inputfile.c_str() << ": ";
inp_detect.open(inputfile.c_str(), ios::in);     //Opening file.
if (! inp_detect.is_open())      //Checking file works.
        {
        cout << "Error while opening input file " << inputfile.c_str() << endl;
        exit(2);
        }
cout << "File opened."<< endl;
while (!inp_detect.eof())        //Getting number of lines.
        {
        i++;
        getline (inp_detect,dummy);
        }
cout << "File contains " << i << " lines."<< endl << endl;
inp_detect.close();

//-------------------
//  Reading in data
//-------------------

const int UDCFlength = i-1;      //Use the number of lines as the array size.
double UDCF[UDCFlength], delT[UDCFlength];       //Make arrays to house the UDCFs and delta Ts.

inp_detect.open(inputfile.c_str(), ios::in);     //Open file again to retrieve data.
i = 0;
while (!inp_detect.eof())
        {
        inp_detect >> delT[i] >> UDCF[i];
        i++;
        getline(inp_detect,dummy);
        }

//cout << UDCF[1000] << " " << UDCF[100000] << " " << delT[1000] << " " << delT[100000] << endl;
             //Sanity check for data input.

//-----------------------
//  Setting up Binning
//-----------------------

error_file.open("errors.txt", ios::out);

maxDelT = delT[0];
minDelT = delT[0];
for (i=0; i <= UDCFlength; i++)
        {
        if (delT[i] > maxDelT)  //Finding max and min delta T.
                maxDelT = delT[i];
        else if (delT[i] < minDelT)
                minDelT = delT[i];
        }

if (maxDelT > Tlim)      //Setting delta T limit of +/- 1000 days.
        {
        maxDelT = Tlim;
        cout << "Delta T maximum limited to " << Tlim << "." << endl;
        }
if (minDelT < -Tlim)
        {
        minDelT = -Tlim;
        cout << "Delta T minimum limited to -" << Tlim << "." << endl;
        }

numNegBins = ceil( (-1) * (minDelT/binSize) );  //Positive number.
numPosBins = ceil(maxDelT/binSize);

cout << "UDCF time range: " << minDelT << " to " << maxDelT << ", with a bin size of " << binSize << "
     days." << endl;
```

```
const int DCFlength = numNegBins + numPosBins;
double DCF[DCFlength], DCFtotal[DCFlength], DCFbinStart[DCFlength];      //Define data array the right
     size to house the DCF bins.
double DCFbinFill[DCFlength];   //Array to store the number of UDCF values assigned to a bin.
double DCFerr[DCFlength], DCFerrSum[DCFlength]; //Arrays for calculating DCF errors.
double DCFbinErr[DCFlength];

cout << "DCF bin indices are from 0 to " << DCFlength-1 << ", with " << numNegBins << " bins below and
     " << numPosBins << " above zero." << endl << endl;

//-----------------
//  Binning Code
//-----------------

for (i=0; i < DCFlength; i++)   //For each bin ...
        {
        DCFbinStart[i] = binSize*(i-numNegBins);        //Define the lower bin limits for the DCFs.
        DCFbinFill[i] = 0;
        DCFtotal[i] = 0;
        for (j=0; j < UDCFlength; j++)  //For each UDCF value ...
                {
                if (delT[j] >= DCFbinStart[i] && delT[j] < (DCFbinStart[i]+binSize) && sqrt(pow(delT[j
                     ],2)) <= Tlim)     //If the value falls in the right time range and is within +/-
                     1000 ...
                    {
                    DCFtotal[i] += UDCF[j];
                    DCFbinFill[i] = DCFbinFill[i] + 1;
                    }
                }
        }

//----------------------
//  Calculation of DCF
//----------------------

DCF_file.open(outputfile.c_str(), ios::out);

for (i=0; i < DCFlength; i++)
        {
        DCF[i] = DCFtotal[i]/DCFbinFill[i];      //Calculation of actual DCF.
        if (DCF[i] != DCF[i])
                error_file << "NaN in DCF: " << DCFtotal[i] << " / " << DCFbinFill[i] << " = " << DCF[i
                     ] << endl;
        }

//------------------------------
//  Calculation of DCF errors
//------------------------------

for (i=0; i < DCFlength; i++)   //For each bin ...
        {
        DCFerrSum[i] = 0;
        for (j=0; j < UDCFlength; j++)  //For each UDCF value ...
                {
                if (delT[j] >= DCFbinStart[i] && delT[j] < (DCFbinStart[i]+binSize))     //If the value
                     falls in the right time range ...
                    {
                    DCFerrSum[i] += (UDCF[j]-DCF[i])*(UDCF[j]-DCF[i]);       //Add the square of the
                         individual error.
                    }
                }
        }

for (i=0; i < DCFlength; i++)
        {
        DCFerr[i] = sqrt(DCFerrSum[i]) / DCFbinFill[i]; //Actual DCF errors.
        DCF_file << DCFbinStart[i]+(binSize/2) << " " << DCF[i] << " " << DCFerr[i] << endl;     //Write
             bins, DCFs and errors to file.
        DCFbinErr[i] = 0;       //Time error for DCFs.
        }

DCF_file.close();

//------------
```

```
//   Graphing
//-------------

cr3 = new TCanvas("cr3","DCF",1);
cr3->cd();
TGraph *gr1 = new TGraphErrors(DCFlength-1, DCFbinStart, DCF, DCFbinErr, DCFerr);
gr1->SetTitle("");
gr1->GetXaxis()->SetTitle("deltaT_ij_(days)");
gr1->GetYaxis()->SetTitle("DCF");
gr1->SetMarkerStyle(21);
gr1->Draw("AP");
//gr1->Fit("gaus");

error_file.close();

return 0;
}
```